

Development of Beam Position Monitors for Final Focus  
Systems at the International Linear Collider

Christina Jane Swinson  
Wolfson College, Oxford

Thesis submitted in fulfilment of the requirements for the degree of Doctor  
of Philosophy at the University of Oxford

Trinity Term 2010

## **Abstract**

The next major step forward for particle physics is a new generation of TeV energy linear colliders. Two systems of beam position monitor (BPM) have been developed for use in the beam delivery system of such a collider. Working prototypes of these two systems will be presented, the first being an interaction point (IP) beam position feedback system making use of stripline BPMs and the second a system of very high resolution cavity BPMs.

Testing of the feedback system installed in the extraction line of the Accelerator Test Facility (ATF) at the High Energy Research Laboratory (KEK) in Japan is presented. The performance of the stripline BPMs used in this system is investigated and shown to have a resolution of a few microns with a latency of less than 10ns.

Thirty two C-band cavity BPMs were installed throughout the extraction and final focus beamlines of ATF2. Commissioning of this system and an investigation into the properties and performance of the BPMs will be described. It will be shown that resolutions of  $< 100$  nm have been achieved and ascertained using Model Independent Analysis (MIA) techniques and the system fully commissioned for normal accelerator operation.



# Acknowledgments

Thanks must, first and foremost go to my supervisor, Professor Phil Burrows, for giving me many great opportunities and for his support from beginning to end. Thanks must also go to Stewart Boogert, sometimes friend and sometimes teacher but often both, for devoting so much of his valuable time to turning me into a physicist (at least you tried!).

Thank you to the FONT group, particularly Colin Perry, Glenn Christian, Ben Constance and Rob Apsimon for answering silly questions, tolerating sleep deprived moods and generally being very very patient (sorry for all the harassment guys!). Also to Christine Clarke, it was a pleasure to join you in the windowless room!

Thanks to everyone on the End Station A project at SLAC especially Mike Woods for giving me the opportunity to participate and Glenn White for putting up with my endless questions. The British contingent of the BABAR collaboration, especially Kim Alwyn, must also get a mention for helping me to make the most of the sun, sea and sand.

Many thanks to all the guys at ATF for all the practical help and support and to Alex Aryshev for keeping me sane under pressure and fully caffeinated at all times.

Thanks to all my friends at QMUL without whom I would probably not have made it through my undergraduate degree. Thanks also to my Father for putting up with me during thesis writing. And finally a big thank you must go to my good friend Iza for all the distractions and, quite simply, for not being a physicist.

# Contents

<b>1</b>	<b>Introduction</b>	<b>1</b>
1.1	The International Linear Collider . . . . .	1
1.1.1	Particle Physics at the ILC . . . . .	2
1.1.2	The Accelerator . . . . .	6
1.1.3	Beam Luminosity . . . . .	10
1.2	The Accelerator Test Facility - A Low Emittance Test Facility for Linear Colliders . . . . .	14
1.2.1	ATF2 - A Final Focus Upgrade to ATF . . . . .	16
1.3	Summary . . . . .	18
<b>2</b>	<b>Beam Position Monitors</b>	<b>20</b>
2.1	Transverse Measurement of Charged Particle Beams . . . . .	20
2.1.1	Button BPMs . . . . .	20
2.1.2	Cavity BPMs . . . . .	21
2.1.3	Stripline BPMs . . . . .	22
2.2	Signal Processing for Stripline BPMs . . . . .	26
2.3	Common Applications of Beam Position Monitors . . . . .	30
2.4	Summary . . . . .	32
<b>3</b>	<b>Stripline Beam Position Monitors for Fast Feedback Systems</b>	<b>34</b>
3.1	The FONT Project . . . . .	34
3.1.1	History . . . . .	35
3.1.2	Testing of the FONT4 Prototype System at ATF . . . . .	42

3.2	Beam Position Monitors and Signal Processing Electronics . . . . .	43
3.2.1	ATF Stripline BPMs . . . . .	43
3.2.2	Analogue BPM Processing Electronics . . . . .	43
3.3	BPM Calibration . . . . .	50
3.3.1	Calibration Results . . . . .	52
3.4	BPM Resolution . . . . .	55
3.4.1	Three BPM Method . . . . .	55
3.4.2	Multiple Processor Method . . . . .	58
3.5	Resolution Dependences . . . . .	66
3.5.1	Possible Causes of Low BPM Resolution . . . . .	69
3.5.2	The Effect of BPM Resolution on Overall Feedback System Performance	70
3.6	FONT System Upgrade for ATF2 . . . . .	71
3.7	Summary . . . . .	72
<b>4</b>	<b>Cavity Beam Position Monitors</b>	<b>73</b>
4.1	Cavities as Beam Position Monitors . . . . .	73
4.1.1	Quality Factor . . . . .	75
4.1.2	Output Signals . . . . .	78
4.1.3	Mode Selection . . . . .	80
4.2	Signal Processing . . . . .	80
4.2.1	Electronics . . . . .	81
4.2.2	Digital Down Conversion . . . . .	82
4.2.3	Calculation of In Phase and Quadrature Phase Components . . . . .	84
4.3	Summary . . . . .	85
<b>5</b>	<b>Cavity BPM Commissioning at ATF2</b>	<b>86</b>
5.1	Cavity BPM Hardware Setup at ATF2 . . . . .	86
5.1.1	Cavities . . . . .	86
5.1.2	Movers . . . . .	89
5.1.3	Mixing Electronics . . . . .	91

5.1.4	Digitization and Timing System . . . . .	91
5.1.5	Local Oscillator and Calibration Tone Systems . . . . .	93
5.2	Software . . . . .	94
5.3	Waveform Analysis . . . . .	96
5.3.1	Tuning . . . . .	96
5.4	Calibration . . . . .	98
5.4.1	Mover Calibration . . . . .	100
5.4.2	Non-Mover Calibration . . . . .	108
5.4.3	Scaling Factors . . . . .	109
5.5	Problems and Solutions . . . . .	110
5.6	Stability and Dynamic Range . . . . .	114
5.7	Summary . . . . .	115
<b>6</b>	<b>Cavity BPM System Performance</b>	<b>118</b>
6.1	BPM Resolution Determination Using Model Independent Analysis . . . . .	118
6.1.1	Singular Value Decomposition . . . . .	120
6.1.2	Results . . . . .	121
6.2	DDC Signal Processing . . . . .	121
6.2.1	Optimization of Filter Width . . . . .	125
6.2.2	Optimization of LO Frequency . . . . .	125
6.3	Applications of Cavity BPMs . . . . .	127
6.3.1	Dispersion Measurement . . . . .	128
6.4	Summary . . . . .	131
<b>7</b>	<b>Summary and Conclusions</b>	<b>133</b>
7.1	Feedback on Nanosecond Timescales . . . . .	133
7.1.1	Beam Position Monitor Studies . . . . .	134
7.1.2	Past Achievements . . . . .	134
7.1.3	Future Goals . . . . .	135
7.2	Cavity BPM . . . . .	135

7.2.1	Future Work for Cavity BPM . . . . .	137
<b>A</b>	<b>Hardware Methods and Schematics</b>	<b>138</b>
A.1	Layout of the FONT Cable Plant at ATF2 . . . . .	138
A.2	Layout of Cavity BPM Timing System . . . . .	138
A.3	Layout of Cavity BPM LO and Caltone Distribution Systems . . . . .	138
A.4	Cavity Frequency - Offline Measurements . . . . .	142
<b>B</b>	<b>Mathematical and Computing Functions</b>	<b>145</b>
B.1	Bessel Functions of the First Kind . . . . .	145
B.2	filter[b,a] . . . . .	146
	<b>Bibliography</b>	<b>148</b>

# List of Figures

1.1	Proposed layout of the ILC . . . . .	2
1.2	Feynman diagrams of dominant Higgs production mechanisms at the ILC . .	4
1.3	Feynman diagrams of possible SUSY production mechanisms at the ILC . .	5
1.4	Feynman diagram of top quark pair production at the ILC . . . . .	6
1.5	Layout of ILC polarized electron source . . . . .	8
1.6	Layout of ILC positron source . . . . .	9
1.7	Layout of RF unit for use in ILC main linac . . . . .	10
1.8	Diagram of the final doublet magnet setup in the ILC final focus system . .	12
1.9	Luminosity variation with vertical beam offset . . . . .	13
1.10	Diagram ATF2 machine layout . . . . .	15
2.1	Engineering drawing of a button BPM installed at ATF . . . . .	21
2.2	Transverse cross sectional representation of a typical stripline BPM . . . . .	22
2.3	Photograph of stripline BPM installed in the ATF2 extraction beamline . . .	23
2.4	Longitudinal cross sectional representation of a stripline BPM . . . . .	24
2.5	A typical stripline signal . . . . .	25
2.6	Amplitude and phase relationships in AM/PM BPM processing . . . . .	27
2.7	Diagram of log ratio BPM processing scheme . . . . .	28
3.1	Diagram outlining the proposed FONT setup at the ILC . . . . .	35
3.2	Diagram outlining the FONT1 setup at NLCTA . . . . .	36
3.3	Results of the FONT1 feedback system for data taken at NLCTA . . . . .	37
3.4	Results of the FONT2 feedback system for data taken at NLCTA . . . . .	38

3.5	Results of the FONT3 feedback system for data taken at ATF . . . . .	39
3.6	Diagram outlining the FONT 4 setup at ATF . . . . .	40
3.7	Results of the FONT4 feedback system for data taken at ATF . . . . .	41
3.8	Block diagram of BPM hardware setup at ATF . . . . .	42
3.9	Technical drawing of stripline BPM installed at ATF . . . . .	44
3.10	Technical drawing showing the longitudinal view of one the stripline BPMs installed at ATF . . . . .	45
3.11	Photo and diagram of FONT4 analogue BPM processor . . . . .	47
3.12	BPM processor sum and difference output signals . . . . .	48
3.13	BPM processor latency measurement . . . . .	50
3.14	BPM calibration results . . . . .	53
3.15	Diagram of method used to predict beam position in a given BPM . . . . .	56
3.16	BPM resolution results . . . . .	58
3.17	BPM resolution using simulated inputs . . . . .	59
3.18	BPM processor calibration results . . . . .	60
3.19	Distribution of BPM position measurements . . . . .	62
3.20	Beam position correlation plots . . . . .	63
3.21	Example of method of selection of data window considered for analysis . . . . .	65
3.22	BPM resolution and calibration constant vs data integration window . . . . .	67
3.23	BPM resolution VS Beam position . . . . .	68
3.24	Diagram of layout of FONT5 at ATF2 . . . . .	71
4.1	Figure depicting electric and magnetic field lines for the monopole and dipole transverse magnetic modes. . . . .	74
4.2	Variation of amplitude of the transverse magnetic field modes with frequency.	76
4.3	The arrangement of waveguides used to couple to cavity dipole modes . . . . .	79
4.4	BPM processing schemes (homodyne/heterodyne receivers) . . . . .	81
4.5	Dipole cavity BPM output waveform . . . . .	82
4.6	Plots of envelope and phase of cavity BPM signal . . . . .	84

5.1	Diagram of ATF2 cavity BPM installation . . . . .	87
5.2	Photo of ATF2 cavity BPM installation . . . . .	88
5.3	Photo of dipole cavity BPM in situ on the ATF2 beamline . . . . .	88
5.4	Photo of dipole cavity BPM (pre-installation) . . . . .	88
5.5	Engineering schematic of a C-band dipole cavity. . . . .	89
5.6	Photo of monopole/reference BPM . . . . .	90
5.7	Photo of cavity BPM with quadrupole mounted on a mechanical mover . . . . .	90
5.8	Block diagram of mixing electronics scheme . . . . .	92
5.9	Plot of calibration tone Signal . . . . .	93
5.10	Main panel of data acquisition software . . . . .	94
5.11	Waveform analysis panel of data acquisition software . . . . .	95
5.12	Screen shot of the data acquisition system waveform display . . . . .	95
5.13	Example of a waveform output from the cavity beam position monitor QD10AFF	97
5.14	Plot of Phase for an Untuned Cavity BPM . . . . .	98
5.15	Correlation plot of $I$ as calculated online and offline (using MATLAB) . . . . .	100
5.16	Plot showing how the BPM position varies during a mover calibration . . . . .	101
5.17	BPM signal amplitude vs pulse number for BPM QD10AFF during a mover calibration procedure. . . . .	102
5.18	Phase vs pulse number for BPM QD10AFF during a mover calibration pro- cedure. . . . .	103
5.19	$Q$ vs $I$ plot for cavity BPM QD10AFF . . . . .	105
5.20	$I'$ and $Q'$ vs beam position plot for cavity BPM QD10AFF . . . . .	106
5.21	Diagram illustrating the method for creating a local orbit bump . . . . .	109
5.22	Beam position vs pulse number for a non-mover calibration . . . . .	110
5.23	$Q$ vs $I$ plot for cavity BPM QF19X . . . . .	111
5.24	$I'$ and $Q'$ vs beam position plot for cavity BPM QF19X . . . . .	112
5.25	Cavity BPM phase issues . . . . .	113
5.26	Long range cavity BPM calibration . . . . .	116
5.27	Plot of beam orbit in the extraction line and final focus system of ATF2 . . . . .	117

6.1	Singular values for SVD . . . . .	119
6.2	Spatial and temporal eigenvectors of beam motion . . . . .	121
6.3	Beam position variation over 500 pulses (before and after MIA) . . . . .	122
6.4	Plot of cavity BPM resolution for all BPMs . . . . .	124
6.5	Variation of DDC parameters with filter width . . . . .	126
6.6	Variation of in-phase component of BPM signal with filter width . . . . .	127
6.7	I vs scale factor for variable filter width . . . . .	128
6.8	Variation of DDC parameters with DDC LO frequency . . . . .	129
6.9	Variation of in-phase component of BPM signal with DDC LO frequency . . . . .	130
6.10	I vs scale factor for variable DDC LO frequency . . . . .	130
6.11	Plot of calculated dispersion at each cavity BPM . . . . .	131
A.1	Layout of the FONT cable plant at ATF2 . . . . .	139
A.2	Diagram depicting the layout of the cavity BPM timing system . . . . .	140
A.3	Diagram of the cavity BPM LO and caltone distribution systems . . . . .	141
A.4	Plot of cavity BPM network analyzer measurements - s11 . . . . .	143
A.5	Plot of cavity BPM network analyzer measurements - s12 . . . . .	144
B.1	Plot of Bessel functions of the first kind . . . . .	146

# List of Tables

1.1	The Standard Model of Particle Physics . . . . .	3
1.2	ILC accelerator parameters . . . . .	7
1.3	ATF VS ILC beam parameters . . . . .	17
2.1	Table of comparison of BPM signal processing schemes . . . . .	31
3.1	FONT4 latency budget . . . . .	49
3.2	Measured beam charge and position for BPM calibration data . . . . .	54
3.3	Measured beam charge and position for BPM calibration data - Multiple processor method . . . . .	61
4.1	Cavity BPM output waveform parameters . . . . .	85
5.1	Table of frequency and quality factors of cavity BPMs as measured online and offline . . . . .	99
5.2	Calibration results for all 23 mover mounted ATF cavity BPMs . . . . .	107
5.3	Table of non-mover calibration results . . . . .	110
5.4	Results of calibration stability test of QM13FF . . . . .	115
5.5	Results of calibration stability test of QM14FF . . . . .	115
6.1	Table of cavity BPM resolution results . . . . .	123

# Chapter 1

## Introduction

The next major step forward for particle physics is a new generation of linear collider. The largest accelerator of this kind to date is the Stanford Linear Collider (SLC) which had a linear accelerator of length two miles with an achievement of 92GeV centre of mass energy [1]. The next step is to produce a linear collider capable of colliding leptons at much higher beam energies. This new generation of accelerators will achieve energies on the scale of TeV with lengths of the order tens of kilometers. These new higher energy machines will allow precision measurements of high mass particles and contribute towards greater understanding of the Standard Model. At such energies there are also many possibilities for discovery beyond the Standard Model.

### 1.1 The International Linear Collider

The International Linear Collider (ILC) is one of the major designs put forward for the next generation of linear accelerators. The ILC project is a collaboration of over three hundred scientific institutions and universities from over 20 countries [2]. Figure 1.1 [3] shows a representation of the proposed layout of the ILC.

The ILC is a linear electron positron collider with a centre of mass energy of 500 GeV with a view to upgrade to 1TeV at a later date [4]. The major advantage of the use of leptons in high energy physics experiments, as opposed to hadrons, is the cleanliness of the particle interactions. Hadron collisions produce a large number of different particle interactions due

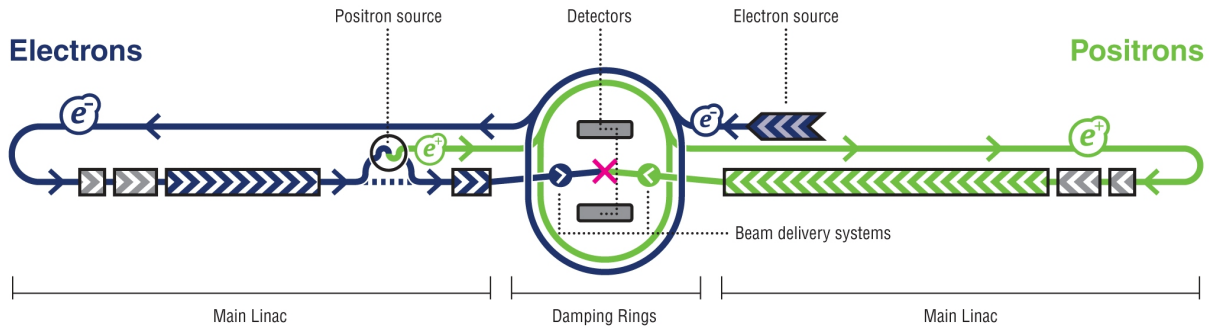


Figure 1.1: A basic representation of the proposed ILC layout [3].

to the internal structure of the hadrons (quarks and gluons) whereas leptons are fundamental particles with no internal features. Electron positron colliders therefore expect lower background radiation and event rates making it easier to identify and reconstruct specific events.

It is necessary for the next generation of lepton colliders to be linear in nature due to the effects of synchrotron radiation in circular machines. A charged particle accelerated along a curved trajectory will emit radiation thereby energy; this energy must be replaced by the accelerating structures. Since the energy lost due to this radiation is dependent upon  $E^4/r$  [5], where  $r$  is the radius of curvature of the path of the electron, the limiting factors in a circular accelerator are the size of the synchrotron and the strength of the accelerating cavities. For example, in order to double the 100GeV electron energy achieved at the Large Electron Positron collider (LEP) with the same accelerating cavities the machine would need to be sixteen times larger [6]. This same issue does not arise at the Large Hadron Collider (LHC) since the energy lost by a charged particle due to synchrotron radiation is also inversely proportional to  $m^4$  (where  $m$  is the mass of the particle) [7], making the use of a circular machine to accelerate protons to TeV energies possible.

### 1.1.1 Particle Physics at the ILC

It is hoped that the International Linear Collider will provide the means to push the boundaries of current knowledge of particle physics and help to explain the universe around us.

Fermions			Bosons	
Quarks	u	c	t	W
	d	s	b	
Leptons	$\nu_e$	$\nu_\mu$	$\nu_\tau$	$\gamma$
	e	$\mu$	$\tau$	g
				$H^*$

Table 1.1: The Standard Model of particle physics (\* as yet unobserved).

Alongside the potential for discovery the ILC will be a precision instrument capable of giving a more detailed view of any new physics processes discovered at the Large Hadron Collider currently operating at CERN, Geneva. There are many working theories on the impact of a machine such as the ILC on particle physics, most notably: precision measurement of the Higgs boson, explanations of the origin of dark matter and a deeper understanding of the Standard Model.

The Standard Model is currently the most complete and widely accepted theory of particle physics. This model is a convolution accounting for unified electroweak theory and quantum chromodynamics. Table 1.1 shows the fundamental particles described by the Standard Model, there are two major types; fermions and bosons. Fermions are spin 1/2 particles which can be split into two groups; quarks and leptons. Quarks come in six different flavours; up, down, charm, strange, top and bottom. They are subject to strong, weak and electromagnetic interactions and have a non integer value of elementary electric charge (either  $+\frac{2}{3}$  or  $-\frac{1}{3}$ ). Quarks have not been found to exist independently, instead they exist in pairs or threes combined in such a way as to give a one or zero value of electric charge. These groups of quarks are known as hadrons and may contain both quarks and anti-quarks. The leptons consist of electrons, muons, taus and their corresponding neutrinos, making six in total. Leptons are subject to weak and electromagnetic interactions but are not subject to the strong force. Electrons, muons and taus have a charge of  $1e$  (where  $e$  is the charge on the electron) and neutrinos are electrically neutral.

Bosons are force carrying particles with integer spin, there are five in total (four of which have been observed experimentally);  $W$  &  $Z$  particles, photons, gluons and the Higgs boson.

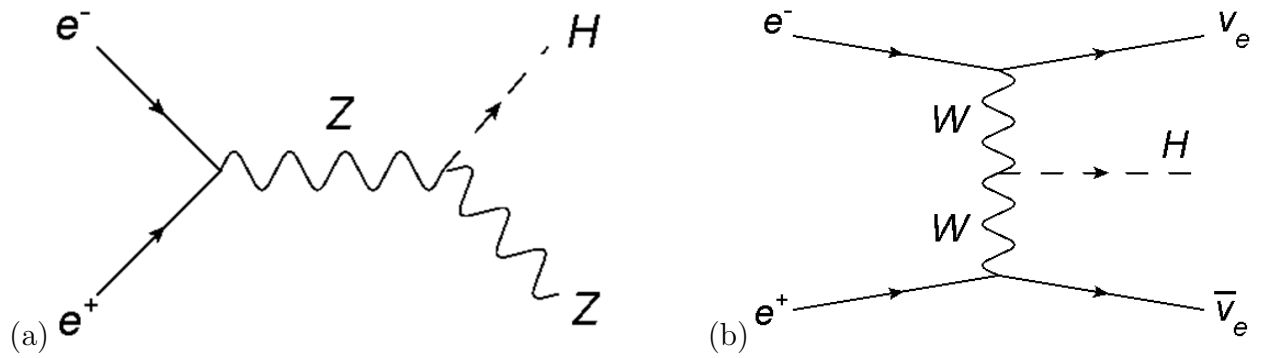


Figure 1.2: Feynman diagrams [11] of dominant Higgs production mechanisms at the ILC [4].

The weak force is mediated by the  $W$  and  $Z$  particles, the electromagnetic force by photons and the strong force by gluons. The Higgs boson is as yet unobserved and may be able to explain the origin of mass.

## Higgs Boson

Although the Standard Model has proved to be very successful in explaining the properties of fundamental particles which have been observed in high energy physics experiments, it is not capable of predicting their masses or explaining the reason why members of the same particle generation have differing masses. The underlying mechanism of mass generation may be explained with the discovery of the Higgs boson. The Higgs boson is an, as yet unobserved, fundamental particle (hypothesised by Peter Higgs in the 1960's) [8] which may help in the understanding of the properties of matter and in the explanation of electroweak symmetry breaking. The Higgs Boson is hypothesised to be a spin zero particle which is the quantum of a scalar field (i.e. invariant under Lorentz transformation). In order to account for mass we assume the presence of this uniform field, known as the Higgs field. This field is locally distorted whenever a particle moves through it and it is this distortion which causes the particles to gain mass [9]. This gathering of the field is known as the Higgs boson. Figure 1.2 shows the two main processes expected to produce a Higgs particle at a linear electron - positron collider [10].

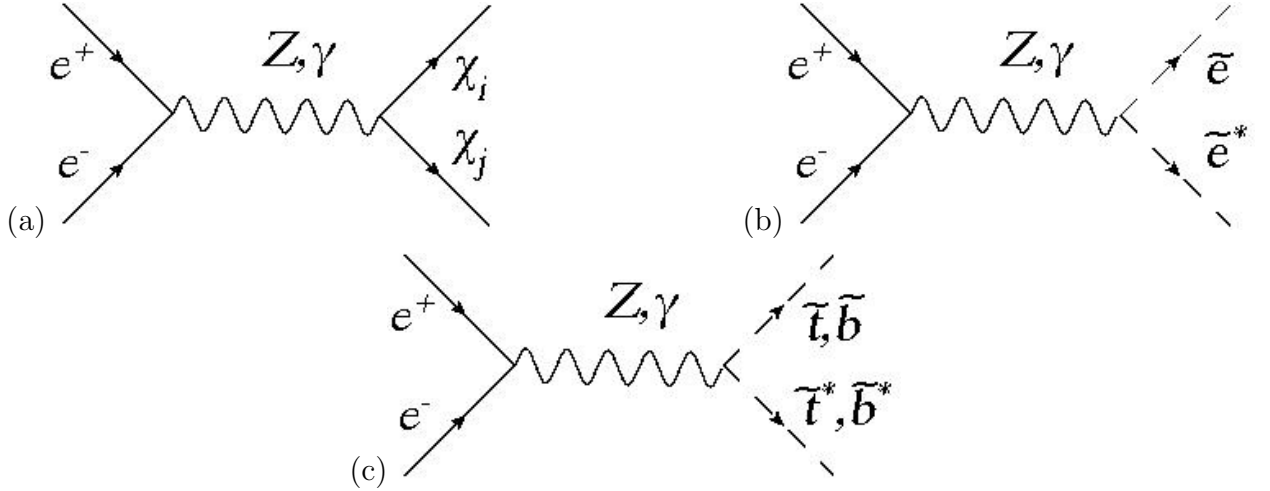


Figure 1.3: Feynman diagrams [11] of possible SUSY production mechanisms at the ILC [12].

## Supersymmetry

Supersymmetry is a theoretical model of particle physics postulated as a realistic extension of the Standard Model. As with the Higgs boson its hypothesis arises from the mass property of particles in the Standard Model. It is a proposed attempt to unify strong, weak and electromagnetic forces into a grand unified theory [13]. It is thought that each boson has a massive, so called, superpartner. Fermions have bosons as their partners and bosons have fermions (meaning each particle differs from its superpartner by spin 1/2) [14]. Some of these particles (known as the lightest supersymmetric particle (LSP) which are weakly interacting massive particles [15] (WIMP), and being the lightest of the supersymmetric particles, unable to decay) may also be good candidates for the dark matter [16] predicted by observations of gravitational behavior of rotating galaxies. These superpartners have not yet been detected but are expected to be visible at higher, but achievable, energies of  $\tilde{m} \leq 1\text{TeV}$  [17]. Figure 1.3 shows Feynman diagrams of mechanisms by which supersymmetric particles may be produced at the ILC.

## Top Quark Physics

The top quark is the most massive of the quark family of fundamental particles and it is for this reason that very high collision energies are required to observe and measure this

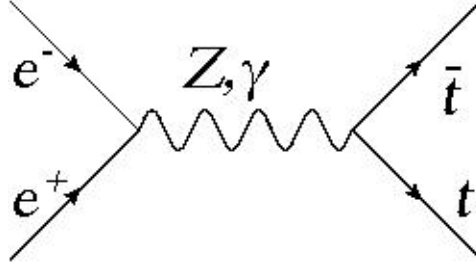


Figure 1.4: Feynman diagram [11] of top quark pair production at the ILC.

particle. First discovered at the Tevatron accelerator, Fermilab in 1995, the top quark has been measured to have a mass of  $171.3 \pm 1.2$  GeV [18]. The ILC will provide precision measurements of the particle's properties and interactions including a mass measurement of greatly reduced error than previously achieved [19], and a measurement of the total decay width. Figure 1.4 shows a Feynman diagram of one possible top quark pair production mechanism at the ILC. Top quark production may also lead to evidence of physics beyond the Standard Model [20].

### 1.1.2 The Accelerator

As represented in figure 1.1, the ILC consists of two similar linear accelerators (linacs) placed head to head, one for the acceleration of electrons and one for positrons. Each of these linacs aims to accelerate the electrons/positrons in bunches of  $2 \times 10^{10}$  particles to energies of 250 GeV (with possible upgrade to 500 GeV); a summary of accelerator and beam parameters is shown in table 1.2.

#### Particle Sources

The ILC is designed for electron - positron collisions to make use of polarized sources and minimize the amount of background radiation produced per desirable event. Figure 1.5 [4] shows a schematic of the electron source. The electron beam will be produced using a photocathode DC (direct current) electron gun; a titanium-sapphire laser with 2 ns pulse [21] knocks electrons from a GaAs photocathode target. These electron bunches are then focused

<b>Parameter</b>	<b>Value</b>
Total site length (km)	31
Length of Beam Delivery section (km)	4.5
<b>Main Linacs</b>	
Average accelerating gradient in cavities (MV/m)	31.5
Length of each Main Linac (km)	11
Beam pulse length (ms)	1
Average beam current (mA)	9.0
<b>Damping Rings</b>	
Beam energy (GeV)	5
Circumference (km)	6.7
<b>IP Beam Parameters</b>	
Center-of-mass energy (GeV)	500
Peak Luminosity ( $\text{cm}^{-2}\text{s}^{-1}$ )	$2 \times 10^{34}$
Repetition rate $f$ (Hz)	5
Number of particles per bunch $N$	$2 \times 10^{10}$
Number of bunches per pulse $n_b$	2625
Bunch interval in the Main Linac $t_b$ (ns)	369.2
in units of RF buckets	480
Normalized emittance at IP $\gamma\epsilon_x^*$ (mm.mrad)	10
Normalized emittance at IP $\gamma\epsilon_y^*$ (mm.mrad)	0.04
Beta function at IP $\beta_x^*$ (mm)	20
Beta function at IP $\beta_y^*$ (mm)	0.4
R.m.s. beam size at IP $\sigma_x^*$ (nm)	639
R.m.s. beam size at IP $\sigma_y^*$ (nm)	5.7
R.m.s. bunch length $\sigma_z$ ( $\mu\text{m}$ )	300
Disruption parameter $D_x$	0.17
Disruption parameter $D_y$	19.4
Beamstrahlung parameter $\Upsilon_{ave}$	0.048
Energy loss by beamstrahlung $\delta_{BS}$	0.024
Number of beamstrahlung photons $n_\gamma$	1.32
Luminosity enhancement factor $H_D$	1.71

Table 1.2: Nominal design parameters for the ILC [4].

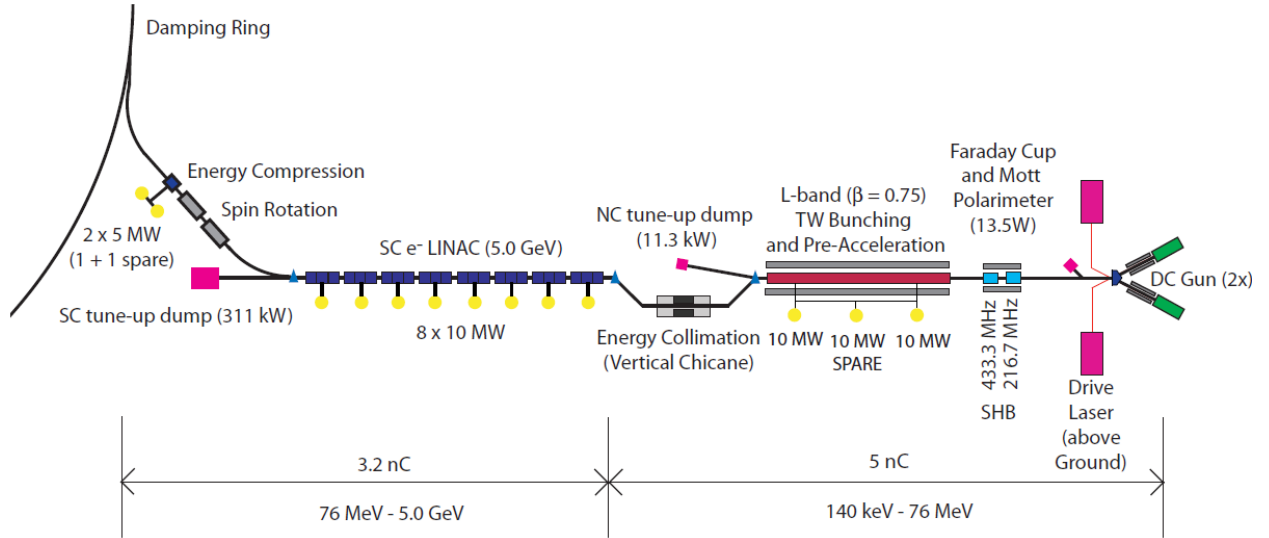


Figure 1.5: Layout of ILC polarized electron source [4].

in an electric field and accelerated to 5 GeV in a 250 m linac and then injected into the damping ring. Positrons are made using photons, produced by the passage of a relativistic electron beam through an undulator, incident on a metal target [22]. The positron beam is also accelerated to 5 GeV before being injected into its damping ring. Figure 1.6 [4] shows a schematic of the positron source.

## Damping Rings

Two 6.7 km damping rings (one for electrons and one for positrons), situated in the middle of the accelerator (figure 1.1), will serve to reduce emittance and to stabilize the beam by removal of jitter [23].

The beam is injected into the damping ring where its trajectory is dictated through the use of bending magnets. As the beam travels through the magnet its path is bent in order to keep it inside the damping ring beampipe. This bending causes emission of photons from the electrons (or positrons) causing a reduction in momentum. This is known as synchrotron radiation and its effect is to reduce the beam emittance to give a stable tightly packed beam [24]. Synchrotron radiation causes the electrons to lose energy so this is replaced, during each turn of the damping ring, by use of an accelerating RF cavity to ensure the beam is extracted from the damping ring at the same energy with which it was injected (5

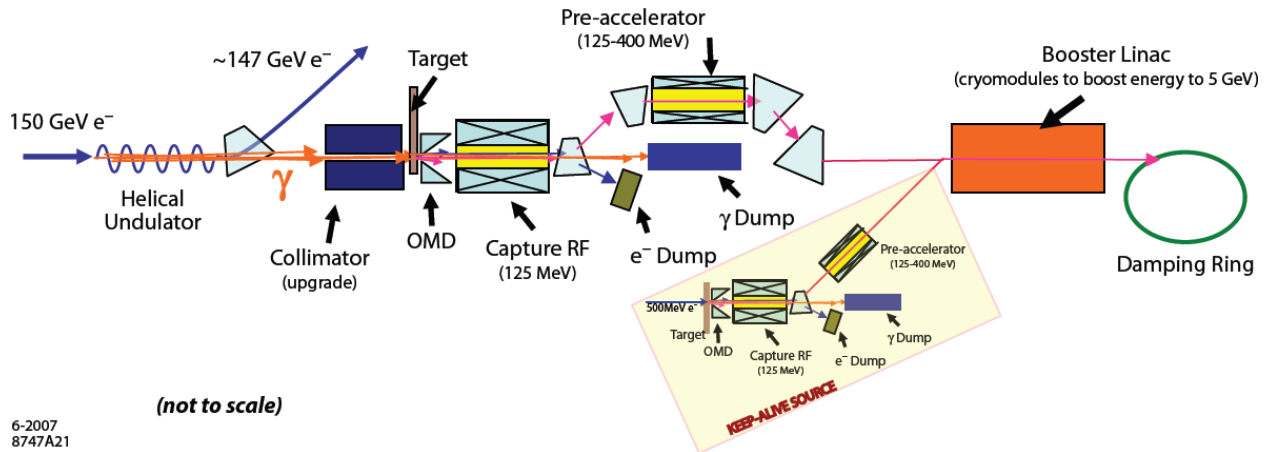


Figure 1.6: Layout of ILC positron source [4].

GeV).

### Ring to Main Linac

The ring to main linac (RTML) is designed to take the beam extracted from the damping ring and prepare it for injection into the main linac. The main functions of this beamline are as follows [25]:

- Acceleration from 5 - 15GeV
- Removal of jitter and dispersion (introduced by damping ring extraction kicker etc.)
- Collimation of beam halo created in damping ring (caused by space charge effects)
- Correct particle polarization from vertical (in damping ring) to that required at the interaction point
- Bunch compression (beam is elongated in the damping ring and must be shortened to ILC interaction point parameters before injection into the main linac)

### Main Linac

The ILC main linacs, one each for electrons and positrons, having a length of 11.3 km [4] each, will accelerate the beams from 15 GeV to 250 GeV [26]. The beams will be accelerated

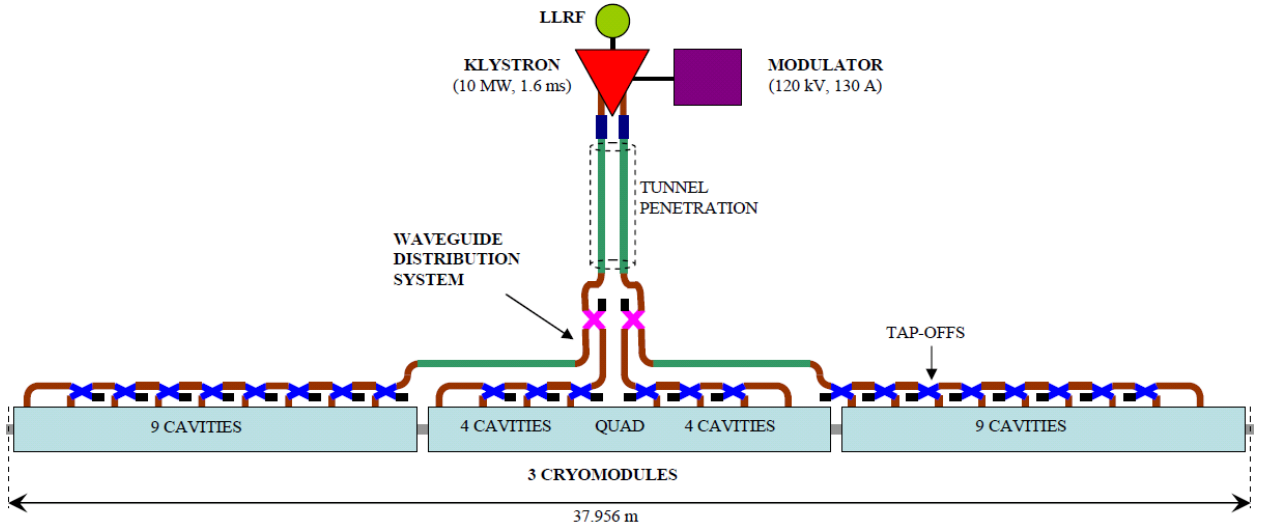


Figure 1.7: Layout of RF unit for use in ILC main linac [4].

using helium cooled, superconducting, L-band (1.3 GHz), niobium cavities with an accelerating gradient exceeding  $30 \text{ MVm}^{-1}$ . The linacs are made up of a number of RF units (278 for the positron and 282 for the electron linac), each of which consists of three cryomodules containing 26 superconducting cavities. Figure 1.7 [4] shows a diagram of the layout of one unit.

## Beam Delivery System

The goal of the beam delivery system (BDS), situated in the last 4.5 km of the accelerator, is to ensure that nanometre-sized particle beams reach the interaction region and collide with high luminosity. The BDS will focus the beam to 639nm in the  $x$  plane and 5.7 nm in  $y$ , it will also maintain this beamsize and ensure collision of the two beams. The BDS will also be home to many different types of beam diagnostics instrumentation, such as beam position monitors and wire scanners, for measurement and control of beam parameters [27].

### 1.1.3 Beam Luminosity

Alongside high energies, one of the most important properties of the incoming beams at the point of collision is luminosity. It is desirable that the maximum number of events be

achieved per collision, this value is determined by the product of the luminosity and the interaction cross section. The event rate is given by equation 1.1, where  $R$  is the event rate,  $L$  the luminosity and  $\sigma_{int}$  the interaction cross section, and the luminosity by equation 1.2

$$R = L\sigma_{int} \quad (1.1)$$

$$L = f \frac{Nn_1n_2}{4\pi\sigma_x\sigma_y} H_D \quad (1.2)$$

Where  $n_{1,2}$  is the number of particles in each colliding bunch,  $N$  is the number of bunches per train,  $\sigma_{x,y}$  is the transverse rms beamsizes at the interaction point (IP),  $f$  is the frequency with which the bunches collide and  $H_D$  is the luminosity enhancement factor. The luminosity enhancement factor arises from the Coulomb interaction between the incoming beams.

The beamsizes,  $\sigma_{x,y}$ , may be written as in equation 1.3 giving an expression for luminosity in terms of beam emittance (equation 1.4).

$$\sigma_{x,y} \approx \sqrt{\sigma_{\beta_{x,y}}^2 + \sigma_{\delta_{x,y}}^2} = \sqrt{\epsilon_{x,y}\beta_{x,y} + D_{x,y}^2 \left(\frac{\Delta P}{P}\right)^2} \quad (1.3)$$

where  $\sigma_{x,y}$  can be deconvolved into an emittance ( $\sigma_{\beta_{x,y}}^2$ ) and a dispersion ( $\sigma_{\delta_{x,y}}^2$ ) contribution. It is also the case that  $\epsilon_{x,y}\beta_{x,y} \gg D_{x,y}^2 \left(\frac{\Delta P}{P}\right)^2$  in the dispersion free region of the beam delivery system, where  $\Delta P/P$  is the momentum spread of the beam and  $D_{x,y}$  is the dispersion function (The dispersion function relates the real trajectory of a particle to that of the ideal orbit and will be discussed further in section 2.3). The quantities  $\epsilon_{x,y}$  and  $\beta_{x,y}$  are the emittance and betatron amplitude function respectively. The emittance is the area of the phase space ellipse occupied by the beam and the beta function is the amplitude of the betatron oscillation. It can be seen from equation 1.4 that in order to achieve a high luminosity each bunch must be small, highly populated and of low emittance.

$$L = f \frac{Nn_1n_2}{4\sqrt{\epsilon_x\beta_x\epsilon_y\beta_y}} H_D \quad (1.4)$$

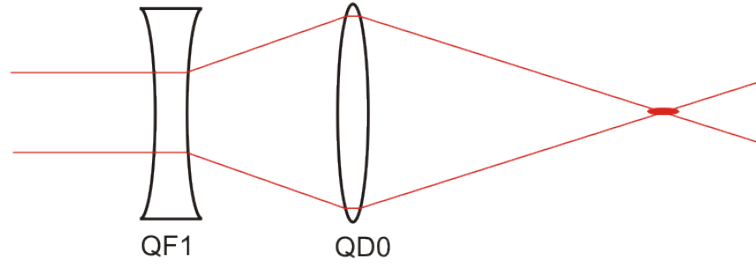


Figure 1.8: Diagram of the final doublet magnet setup in the ILC final focus system. Using standard notation QF1 indicates a quadrupole magnet which focuses the beam in  $x$  and defocuses in  $y$ , and QD0 focuses in  $y$  and defocuses in  $x$ .

### Nanometre-sized Beams

To achieve high luminosity the ILC will use flat nanometre-sized particle beams; 5.7nm in the vertical dimension and 639nm in the horizontal [4]. Flat beams are used instead of round beams in order to minimize  $e^+e^-$  pair production caused when particles pass through the electromagnetic field of the opposing beam. Figure 1.8 shows the method by which such small beams are achieved. The section of the BDS situated next to the interaction point is known as the final focus system, the aim of which is to demagnify the beams down to nanometre level [28]. The final focus system acts as a telescope [29] using strong ( $140\text{Tm}^{-1}$  [30]) quadrupole magnets to focus the beams (figure 1.8). The beam is first made large using a defocussing magnet (QF1) and then squeezed down to 5.7nm, in the  $y$  dimension, using a very strong focussing magnet (QD0). The use of such high strength magnets introduces chromaticity in the beam which is corrected by the use of sextupole magnets which accompany each quadrupole. Working with such small beams presents many challenges in beam instrumentation with respect to measurement of beam properties. This has prompted, among other things, the development of cavity beam position monitors capable of nanometre precision measurements of beam position (see chapter 4).

### Feedback Systems for Luminosity Optimization at the ILC

Achievement of the maximum number of events is also dependent on precision alignment of the beams to ensure a head on collision. Where head on collision does not occur  $\sigma_x\sigma_y$  in the

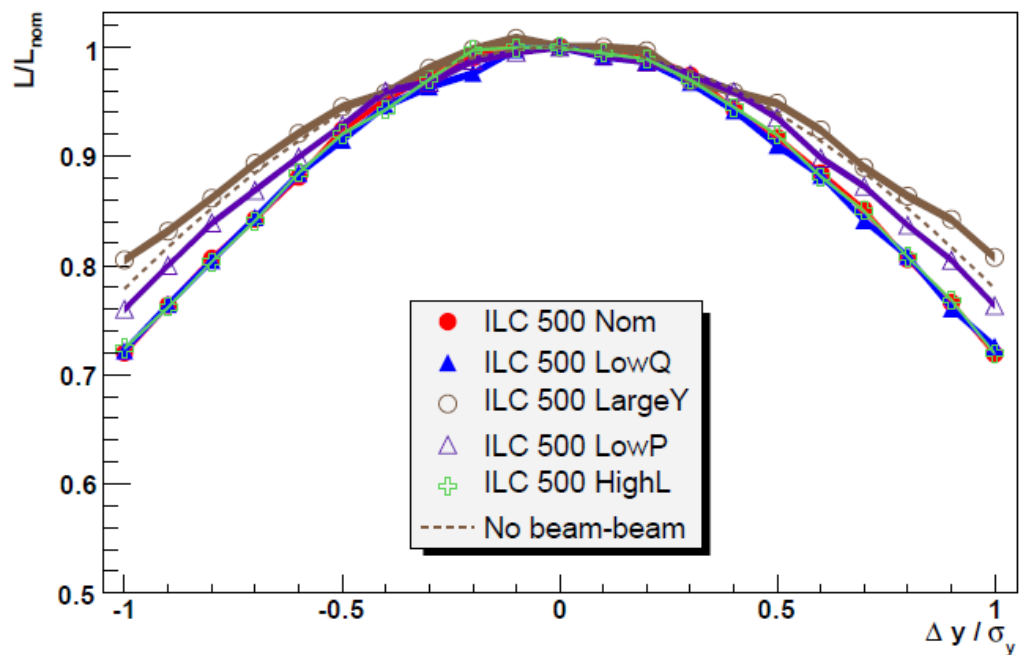
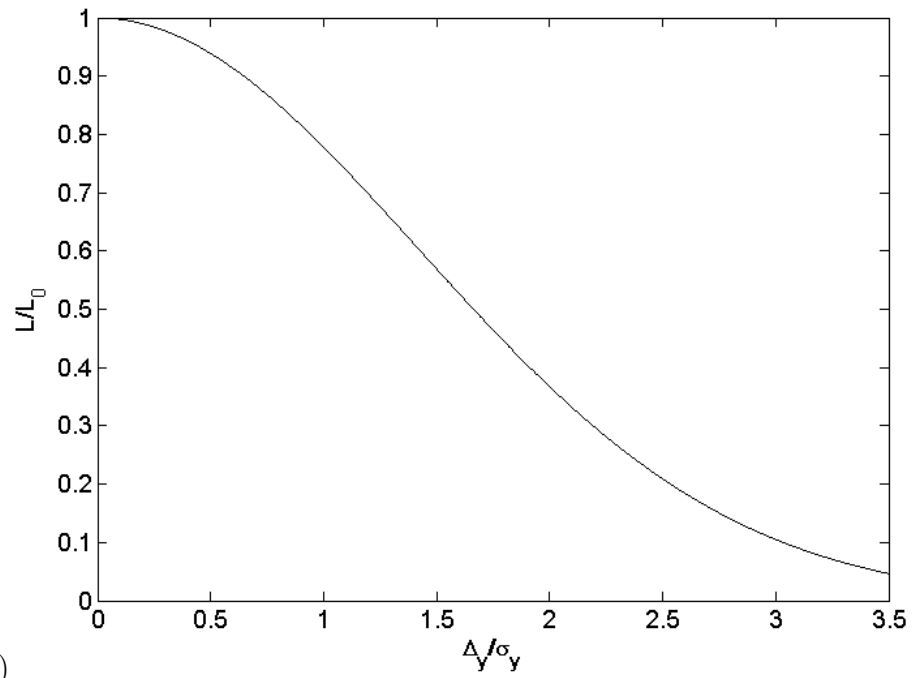


Figure 1.9: The effect of vertical beam offset on luminosity for  $e^+ e^-$  collisions. (a) is for a the simplified case of no interaction between the two incoming beams ( $H_D = 1$ ) and (b) [31] is for the various different ILC beam parameters [4].

## 1.2 The Accelerator Test Facility - A Low Emittance Test Facility for Linear Colliders<sup>14</sup>

luminosity calculation (equation 1.2) now represents the area of the portion of the beams which collide [32]. Figure 1.9a shows the variation of normalized luminosity with normalized vertical position offset of the beams for two Gaussian distributed same-sized beams. The relationship is as follows [33]

$$L/L_0 = e^{-\frac{1}{4} \frac{\Delta y^2}{\sigma_y^2}} \quad (1.5)$$

Where  $L/L_0$  is the normalized luminosity,  $\sigma_y$  the vertical beamsize and  $\Delta y$  is the offset in vertical position of the beams. This is for the simplified case of no interaction between the two incoming beams ( $H_D = 1$ ). Figure 1.9b shows simulated results of the variation of luminosity as a result of vertical offset between two colliding ILC beams [31]. An offset in transverse position between the two incoming beams may occur due to cultural noise and ground motion. Several position feedback systems will be used throughout the ILC to maintain beam orbit with high frequency ground motion requiring the most complex correction system. This motion causes movement of the final doublet quadrupoles which in turn causes transverse beam motion and a total loss of luminosity through beam misalignment and emittance growth [34]. It is the intent that, at the ILC, there will be a fast feedback system designed to correct beam misalignment at the individual bunch level through the use of beam position monitors and fast kickers (see chapter 3).

## 1.2 The Accelerator Test Facility - A Low Emittance Test Facility for Linear Colliders

The Accelerator Test Facility (ATF) at KEK, Japan is a small test accelerator designed for use in the development of subsystems to be used in the next generation of linear colliders. Initially designed as a test facility for JLC (Japan Linear Collider) [35], the ATF is an ideal test facility for ILC beam diagnostics and orbit correction systems. Figure 1.10 [36] shows the layout of ATF, after a recent upgrade, divided into 5 major sections; injection (photocathode RF gun), linac, damping ring, extraction line and final focus system.

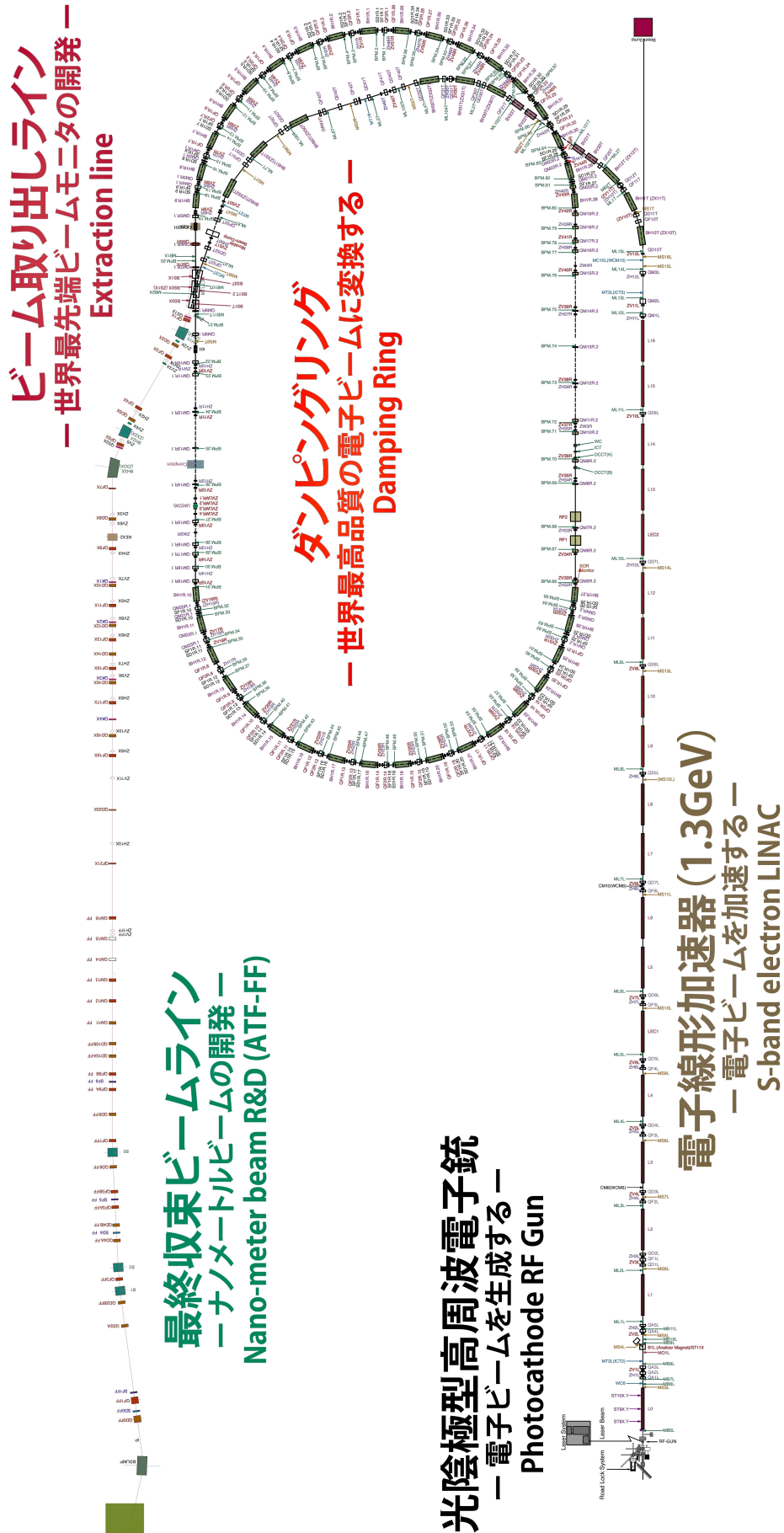


Figure 1.10: Diagram of ATF2 machine layout [36].

### Injection and Linac

Electrons are produced using a photocathode RF gun. Electrons are released by a laser incident on a cesium-telluride photocathode [37]. These electron bunches, containing typically  $1 \times 10^{10}$  particles, are then accelerated through a 90m long S-band linac to reach a beam energy of 1.28 GeV, with an achieved average accelerating gradient of  $26 \text{ MVm}^{-1}$  for the nominal case [38].

### Damping Ring

When the beam has exited the linac it is then injected into a 138 m circumference damping ring, consisting of two arcs and two straight sections, where it is stored for a few hundred milliseconds [39] to produce a beam with emittances of  $\epsilon_x \approx 1 \text{ nm.rad}$  and  $\epsilon_y \approx 6 \text{ pm.rad}$  [40]. The beam is then extracted from the damping ring into the extraction line.

### Extraction Line

The ATF extraction line is used primarily for testing and development of prototype beam diagnostics and orbit correction systems. The low emittance of the ATF beam makes it ideal for testing ILC beam instrumentation, specifically those to be used in the final sections of the accelerator before collision. Among other things ATF has seen extensive testing and development of laser wire scanners, precision beam position monitors and orbit feedback systems. A recent upgrade to this facility has made way for many new projects and is providing a much improved beam quality.

#### 1.2.1 ATF2 - A Final Focus Upgrade to ATF

The commissioning of the upgrade to ATF2 is ongoing with the aim of achieving the following goals [41]:

- Achievement of 37nm beam size

## 1.2 The Accelerator Test Facility - A Low Emittance Test Facility for Linear Colliders17

Parameter	ATF2	ILC
Beam energy (GeV)	1.3	250
Relative luminosity: $L/L_0$ (m)	1	3.5-4.5
Emittance: $\gamma\epsilon_x/\gamma\epsilon_y$ ( <i>mrad</i> )	$5 \times 10^{-6}/3 \times 10^{-8}$	$1 \times 10^{-5}/4 \times 10^{-8}$
$\beta$ at IP: $\beta_x^*/\beta_y^*$ ( <i>mm</i> )	4.0/0.1	21/0.4
$\eta'$ at IP: $\eta'_x$	0.14	0.094
Energy spread: $\sigma_E$ (%)	$\sim 0.1$	$\sim 0.1$
Chromaticity: $W_y$	$\sim 10^4$	$\sim 10^4$
Beam size at IP: $\sigma_x^*/\sigma_y^*$ ( $\mu\text{m}/\text{nm}$ )	2.8/34	0.66/5.7
Aspect ratio: $\sigma_x^*/\sigma_y^*$	82	115

Table 1.3: ATF VS ILC beam parameters [42].

- Demonstration of a compact final focus system based on local chromaticity correction
- Maintenance of the small beam size
- Control of beam position down to 2nm level at IP
- Demonstration of beam orbit stabilization with nanometre precision at the IP
- Establishment of beam jitter control techniques at the nanometre level with an ILC-like beam

In order to develop suitable systems to ensure beam delivery at the ILC it is ideal to have a beam comparable to that of the ILC. Table 1.3 [42] shows a comparison of ATF2 and proposed ILC beam parameters. Whilst the ATF2 beam is not comparable in energy to that of the ILC it is an ultra low emittance beam with a very small beamsize. These two properties together with common values for energy spread and chromaticity produce a beam whose behaviour is representative of the ILC beam, allowing the ATF2 final focus system as a scale model of the proposed ILC final focus system [42] to be meaningfully tested.

## Nanometre Scale Beam Position Measurements

The nanometre sized beam at ATF will require a very high resolution beam position monitoring system in order to accurately determine its position. It is to this end that an extensive array of cavity beam position monitors have been installed throughout the extraction and final focus beamlines.

## Feedback Systems

Position and angle feedback systems are an essential component of the ILC beam delivery system to ensure maximum collision luminosity. A prototype ILC feedback system is currently being tested by the FONT (Feedback on Nanosecond Timescales) [43] research group at ATF. This project may also prove to be of use in the day to day running of ATF, providing position stability and therefore reducing beam jitter.

## 1.3 Summary

The future of particle physics is dependent on the development of accelerator technology to allow very high energy particle collisions to take place. The Large Hadron Collider (LHC) is currently fulfilling this role via TeV hadron collisions. The next step is to build an accelerator to provide not only high energy collisions but high energy collisions of leptons, specifically electrons and positrons, to allow more precise particle measurements to be made. A linear collider is the best way of achieving this important goal.

One of the major requirements of any particle accelerator is that of high luminosity. The aim is to cause as many particle interactions as possible each time two bunches of particles collide; this is achieved by an exceptionally small, dense beam and by ensuring the beams coincide with maximum overlap of the bunches. This luminosity requirement is what makes the beam delivery system (BDS) such an important part of the accelerator. The remainder of this thesis is dedicated to the development of two of the major parts of the

BDS: position feedback systems and nanometre resolution cavity beam position monitors, including research and development of prototype systems at ATF.

# Chapter 2

## Beam Position Monitors

Beam position monitors (BPMs) are an integral part of any beam diagnostics system and are found in most accelerators. In addition to their research use in understanding the properties and behaviour of particle beams BPMs are also essential for the day to day running of an accelerator. This chapter will give a short introduction to beam position monitors and their most common applications.

### 2.1 Transverse Measurement of Charged Particle Beams

There are many methods and devices for determining the transverse beam position. This section will concentrate on button, stripline and cavity beam position monitors, the three most common types of BPM in use.

#### 2.1.1 Button BPMs

Button BPMs usually consist of two or more pairs of button shaped electrodes placed into opposing sides of the wall of the beampipe. The position of the beam is determined using the coupling of the electrodes with the electric field of the beam. This is often the simplest method by which the beam position can be measured.

It is convenient to consider the image charge of the beam since for relativistic beams the image charge has the same distribution as the beam charge [45], simplifying the interpretation of beam position monitor signals. In the relativistic case the longitudinal component of the

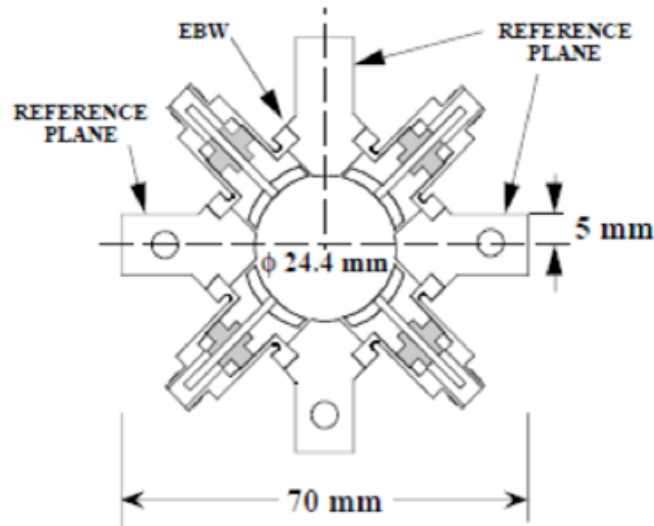


Figure 2.1: Diagram, showing a cross sectional view, of a typical button BPM used at ATF. This BPM has two pairs of circular shaped electrodes (or pickups) [44].

electromagnetic field is Lorentz contracted leaving the field with an almost purely radial component. The beam position is calculated from the difference between the current induced in each pair of buttons, and can be normalized by the beam charge using the sum of these two signals. Figure 2.1 [44] shows a schematic of a typical button BPM used at ATF.

### 2.1.2 Cavity BPMs

The use of resonant cavities as BPMs is a more recently developed method of transverse beam position measurement. A cavity BPM consists essentially of a cavity constructed in such a way as to resonate strongly at some specified frequency. As the beam passes through the cavity its electric field produces a high frequency wave which causes the cavity to resonate. Of the many possible excitation modes the mode chosen is one where the electric field component in the direction of motion of the beam is equal to zero so when the beam is at the centre of the BPM no oscillation is induced and therefore no output signal is seen. For beam position monitors it is usual to use the dipole mode, although this is not necessarily the most prominent mode, since the amplitude of the output of this mode varies linearly with the beam's distance from the cavity wall. Cavity BPMs will be discussed in more detail in chapter 4.

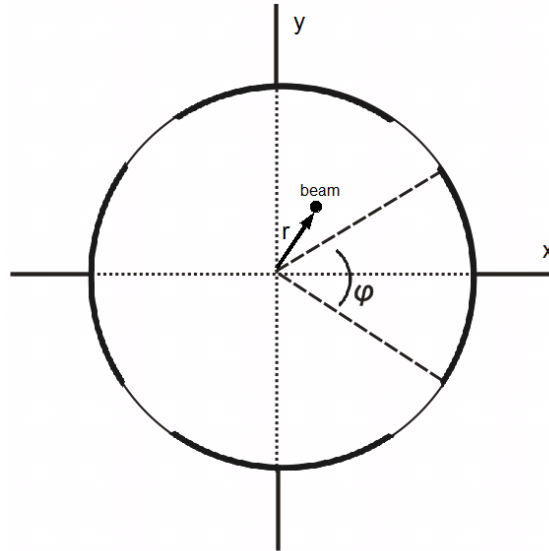


Figure 2.2: A diagram representing a transverse cross sectional view of a typical stripline BPM. The sketch shows four stripline electrodes, each one with a pickup at one end of the metal strip.

### 2.1.3 Stripline BPMs

A transverse cross sectional representation of a typical stripline BPM is shown in figure 2.2, and figure 2.3 shows a photograph of a longitudinal view of a stripline installed at ATF2. Stripline BPMs work in a similar way to button BPMs with the one major difference being that the electrodes are elongated strips as opposed to being button shaped (figure 2.4). This has the effect that the bipolar signal seen is much slower (figure 2.5) than that seen by a button, with the difference between the two peaks being equal to twice the length of the striplines.

As the beam travels through the beampipe it is accompanied by an image charge, of equal magnitude but opposite sign to that of the beam, induced in the wall of the beampipe. The BPM is a discontinuity in the beampipe and as the image charge crosses this gap a voltage is induced in the metal strip. This results in two pulses, one traveling forward and one backward with respect to the direction of motion of the beam, one of which goes to the electronics (figure 2.4(a)) whilst the other travels down the strip. As the beam reaches the downstream end of the BPM (figure 2.4(b)) it encounters a second discontinuity at the end of the strip, this again produces two identical pulses though opposite in polarity to those

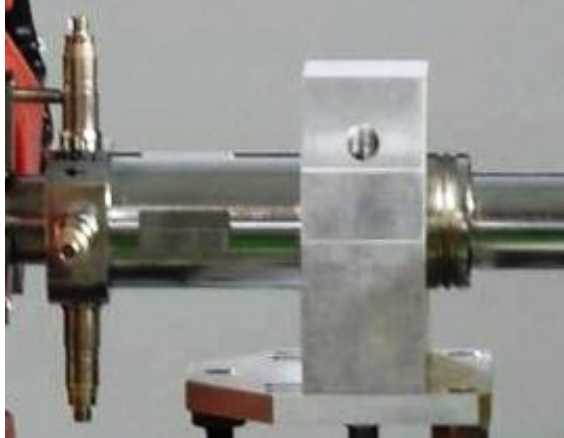


Figure 2.3: Photograph of stripline BPM installed in ATF2 extraction beamline. The signals are read from the four pickups located at the left hand end of the BPM.

created upstream. Since, in the relativistic case, the pulse produced at the upstream end of the strip arrives at the downstream end at the same time as the beam it coincides in time with the pulses produced at the downstream discontinuity. This means that since the pulses are of equal magnitude but opposite in sign they will cancel leaving only one pulse which was created at the downstream end of the strip. This pulse then travels along the strip against the direction of motion of the beam and to the electronics. The result is that the input to the BPM processing electronics is a bipolar (figure 2.5) pulse with a separation in time as shown by equation 2.1, where  $l$  is the length of the stripline. This is the time taken for the beam to travel the length of the BPM plus the time taken for the second pulse to travel back along the strip.

$$t = \frac{2l}{c} \quad (2.1)$$

The sum of the image charge over the beampipe is constant, and equal to the charge of the beam, and the Lorentz contraction of the electric and magnetic fields ensures the transverse image charge distribution is the same as that of the particle bunch. This means that the percentage of the total image charge induced in each strip will be equal to the ratio of the strip width to the beampipe circumference for a beam whose position is equidistant from all strips. This can be described as in equation 2.2 where  $I_{strip}$  is the current induced

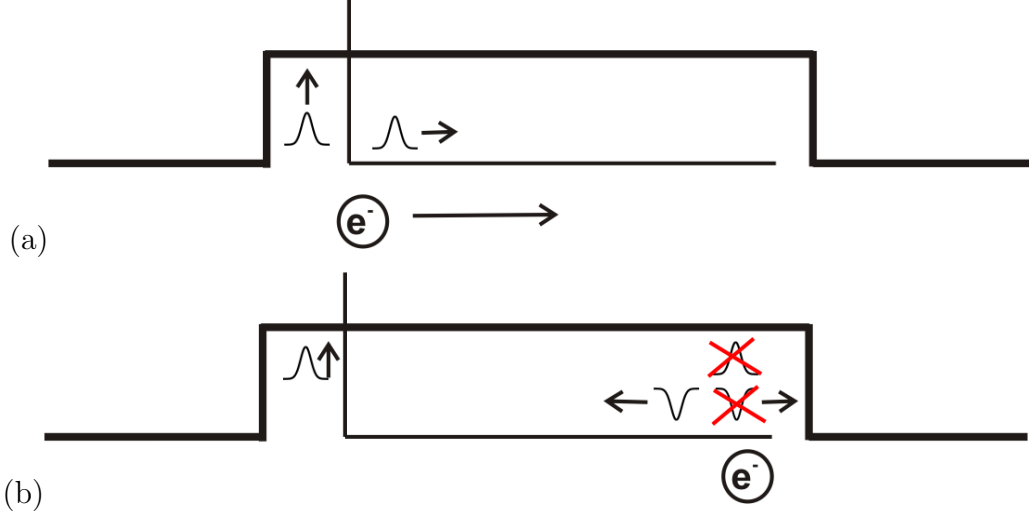


Figure 2.4: Two diagrams each representing a longitudinal cross section of a stripline BPM, showing the beampipe wall with one of the four metal strips. (a) shows the induced voltage as the beam crosses from the beampipe to the upstream end of the stripline and (b) illustrates the state as the beam exits via the downstream end of the BPM.

in the BPM electrode and  $\varphi$  is the azimuthal angle subtended by the strip [46] (figure 2.2).

$$I_{strip} = I_{beam} \frac{\varphi}{2\pi} \quad (2.2)$$

The voltage output, using Ohm's law, can then be calculated in the time domain to be [47]

$$V(t) = \frac{\varphi Z}{4\pi} \left[ I_{beam}(t) - I_{beam} \left( t - \frac{2l}{c} \right) \right] \quad (2.3)$$

where  $Z$  is the characteristic impedance of the strip. This is a calculation for the simplest case (for the beam traveling through the centre of the BPM). For a case where the beam is off centre we should consider a more general approach. Consider an electron bunch of Gaussian distribution whose current in the time domain may be described as

$$I_{beam}(t) = \frac{eN}{\sqrt{2\pi}\sigma_t} \exp\left(\frac{-t^2}{2\sigma_t^2}\right) \quad (2.4)$$

where  $e$  is the charge on the electron,  $N$  the number of particles in the bunch and  $\sigma_t$  the rms bunch length (in units of time). For short bunches (i.e. in the limit where the bunch

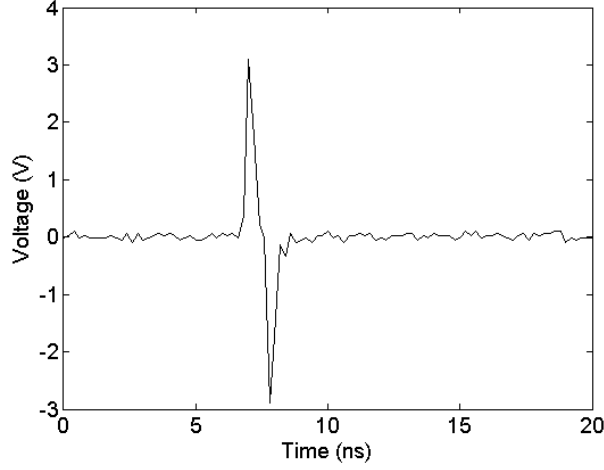


Figure 2.5: An example of a signal as measured directly from the BPM stripline. It can be seen that the two peaks are separated by approximately 800ps which is consistent with the length of the strip (12cm).

length ( $\sigma_t$ ) tends to zero) the beam current may be approximated to [48].

$$I_{beam} = qc\delta(z) \quad (2.5)$$

where  $q$  is the beam charge and  $\delta$  is the Dirac delta function. The image current coupled to the stripline for a beam which is not central to the beampipe can then be written as

$$I_{strip} = -\frac{I_{beam}}{2\pi}(b^2 - r^2) \int_{-\varphi}^{\varphi} \frac{d\varphi}{b^2 + r^2 - 2br \cos(\phi - \varphi)} \quad (2.6)$$

Where  $b$  is the bore radius of the BPM,  $r$  is the displacement of the beam and  $\phi$  is the tilt angle of the beam. Again using Ohm's law ( $V = I_{strip}Z$ ) and substituting in 2.6 we can predict the peak voltage of the signal received from the strip to be

$$V \propto \tan\left(\frac{b\varphi}{2(b-r)}\right) \quad (2.7)$$

Using Taylor expansion

$$V \propto \frac{b\varphi}{2(b-r)} - \frac{(b\varphi)^3}{24(b-r)^3} + \frac{(b\varphi)^5}{160(b-r)^5} - \dots \quad (2.8)$$

and in the limit where  $r \ll b$  we can approximate to

$$V \propto \frac{(b\varphi)}{2(b-r)} \quad (2.9)$$

By considering equations 2.5, 2.6 and 2.9 a generalized expression may be formed

$$V = f(t)qZ \frac{b\varphi}{2(b-r)} \quad (2.10)$$

where  $f(t)$  defines the shape of the output pulse [49].

## 2.2 Signal Processing for Stripline BPMs

There are three major methods used to analyze stripline signals to derive the position of a beam traveling through the BPM. These are: log ratio, amplitude to phase modulation (AM/PM) and, most commonly, the difference over sum method.

### Difference over Sum

The difference over sum method may be used in both hardware and software environments to simply and accurately determine the beam position. As the signal on each strip is dependent only on the beam position and charge along with the BPM geometry and impedance (equation 2.10), considering the impedance to be fixed and the beam displacement to be much smaller than the bore radius of the BPM we can say that for two opposing striplines the sum of the signals is linearly dependent on the charge of the beam (in the limit where  $r \ll b$ ).

$$V_1 + V_2 = f(t)qZ \frac{b\varphi}{(b^2 - r^2)} b \quad (2.11)$$

$$V_1 - V_2 = f(t)qZ \frac{b\varphi}{(b^2 - r^2)} r \quad (2.12)$$

From equation 2.12 it can be seen that the difference between these two signals depends on both the beam charge and the position of the beam. We can normalize this calculated differ-

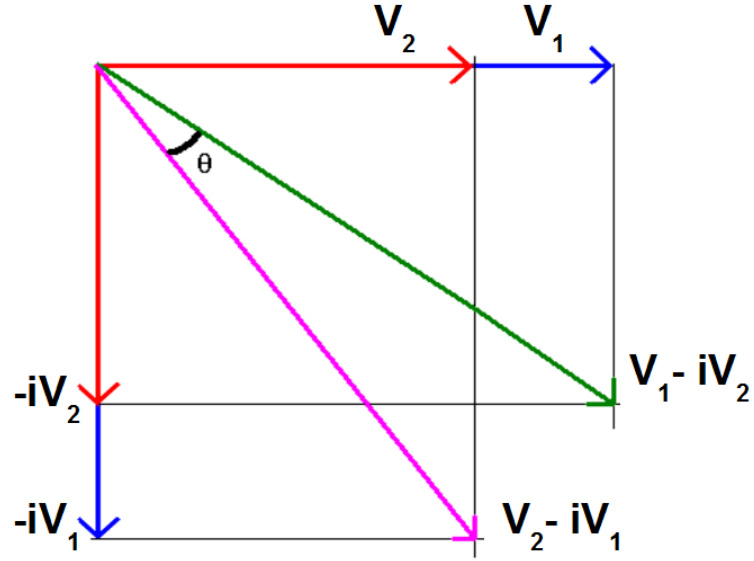


Figure 2.6: Amplitude and phase relationships of the output signals from two opposing striplines in the amplitude to phase modulation signal processing scheme.  $\theta$  represents the relative phase and the vector length the amplitude of the signals [49].

ence  $(V_1 - V_2)$  using the sum  $(V_1 + V_2)$  to give a charge independent position measurement.

$$\frac{V_1 - V_2}{V_1 + V_2} = \frac{r}{b} \quad (2.13)$$

### Amplitude to Phase Modulation

An alternative method, to that of difference over sum, used to interpret stripline BPM signals is the AM/PM method or amplitude to phase modulation and is a charge independent hardware based solution. Considering two striplines placed opposite each other, this method splits the output signal from each stripline into two and rotates one half by  $90^\circ$  and adds this rotated signal to the unrotated signal of the opposing strip. The two resulting signals are equal in amplitude but with a phase difference which is proportional to the position of the beam. The relationship can be characterized as follows [50].

$$y \equiv \Delta\theta = 2 \tan^{-1} \left( \frac{V_1}{V_2} \right) - 2\pi \quad (2.14)$$

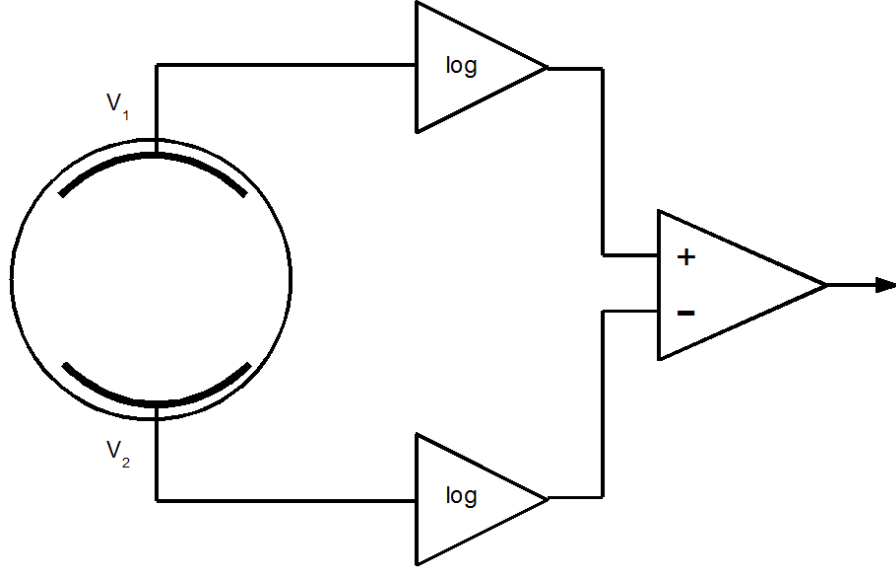


Figure 2.7: Basic representation of the electronics scheme for log ratio BPM processing. Each signal passes through a logarithmic amplifier followed by a difference amplifier to give an output which is beam position dependent but charge independent.

Where  $\Delta\theta$  is the phase difference between the two signals,  $V_1$  and  $V_2$  represent the output signals of each of the two opposing strips and  $y$  is the position of the beam from the half way point between the two strips. Figure 2.6 [49] is a representation of the amplitude and phase relationships of the two output signals,  $\theta$  represents the relative phase and the vector length the amplitude of the signals. The stripline signals undergo a rotation such that the amplitude is dependent only on charge and the phase difference only on position [51].

### Log ratio

A third signal processing method is known as the log ratio method. Again this can be done using hardware or software methods. Equations 2.15 and 2.17 [52] show how this method determines the beam position independent of charge. For a pair of striplines (1 and 2) placed diametrically opposite to each other within a cylindrical beampipe their relative output signals, when a beam bunch passes through, may be described as

$$\frac{I_1}{I_2} = \frac{1 + \frac{4}{\phi_0} \sum_{n=1}^{\text{inf}} \frac{1}{n} \left(\frac{r_0^n}{R_n}\right) \cos(n\theta_0) \sin\left(\frac{n\phi_0}{2}\right)}{1 + \frac{4}{\phi_0} \sum_{n=1}^{\text{inf}} \frac{1}{n} \left(\frac{r_0^n}{R_n}\right) \cos(n\theta_0) \sin\left(n\left(\pi + \frac{\phi_0}{2}\right)\right)} \quad (2.15)$$

where  $R$  is the bore radius of the BPM,  $\phi_0$  is the angle subtended by the striplines and  $r_0, \theta_0$  are the beam coordinates. Using  $y = r_0 \cos \theta_0$  equation 2.15 may be simplified to give

$$y \approx \frac{Ln10}{160} \left( \frac{R_n \theta_0}{\sin\left(\frac{\phi}{2}\right)} \right) 20 \log \left( \frac{I_1}{I_2} \right) \quad (2.16)$$

So the beam position ( $y$ ) from the centre of the beampipe is dependent on the logarithmic ratio of the two stripline outputs.

$$y = \log \left( \frac{V_1}{V_2} \right) \quad (2.17)$$

Figure 2.7 shows a schematic of the electronics scheme for log ratio BPM processing [53]. Each signal passes through a logarithmic amplifier followed by a difference amplifier to give an output which is beam position dependent but charge independent.

### Comparison of Signal Processing Techniques

Table 2.1 is a comparison of the three BPM signal processing techniques. The log ratio method provides the best linearity, allowing more reliable beam position measurements when the beam is extremely off axis than is achievable with the AM/PM or difference-over-sum schemes. Although the AM/PM method has the poorest linearity it tends to have lower amplifier noise and higher bandwidth. Both the log ratio and AM/PM methods have the capacity for real time charge normalisation.

In spite of the fact that online charge normalisation (within the BPM electronics) is not possible in using the difference-over-sum technique, the stripline BPMs in the ILC feedback system (FONT) will implement this scheme. There are multiple advantages to using this signal processing method:

- Circuit may be passive (no amplifier is required to drive electrical components, and signal levels output by the striplines are, in general sufficiently large.)
  - Lower latency (Amplification is often a major cause of increased latency. Absence of these components, combined with the fact that the electronics used are the most

simple of all the three processing schemes serves to minimize the time taken to process the BPM signals.)

- Lower noise, higher resolution (Active, as opposed to passive, components tend to have lower signal-to-noise ratios. It is desirable to maximize the signal-to-noise ratio of the BPM electronics to increase the resolution of the processor, and thus the position measurement.)
- Higher bandwidth (other processing schemes may experience more limitation of bandwidth due to the use of diodes, such as is the case with the log ratio method.)
- Good linearity (The linearity of the major components (to be discussed in more detail in section 3.2.2), such as mixers, is the limiting factor of the processor linearity. As the beam moves further away from the centre of the beampipe and the stripline signal output increases the response of the electronic components no longer exhibit a linear response. Elimination of amplifiers together with high quality components can maximize this linearity.)
- Charge normalization may be achieved using other methods (FONT will use digital methods to perform charge normalization using sum and difference signal outputs from the BPM electronics).

## 2.3 Common Applications of Beam Position Monitors

Beam position monitors such as those described above provide an accurate and non-invasive method of beam orbit measurement. This orbit information may be used in various ways to measure different beam parameters, allowing correction of these values to give the preferred beam state. Two of the most common applications for beam position monitors in a charged particle accelerator are in orbit and dispersion correction.

Feature	Difference-over-sum	AM-PM	Log ratio
Time-domain processing	yes	no	no
Frequency-domain processing	yes	yes	yes
Carrier frequency range	> 1 GHz	< 100 MHz	< 500 MHz
Acquisition bandwidth	> 100 MHz	< 10 MHz	< 100 MHz
Amplitude dynamic range	low	high	high
Displacement response linearity	intermediate	poorest	best
Normalized real-time response	no	yes	yes
Cable phase-matching required	depends	yes	no
Amplifier noise figure	can be very low	> 20 dB typ	15 dB achieved
Cost	lowest	highest	intermediate
Circuit complexity	lowest	highest	intermediate

Table 2.1: Comparison of difference-over-sum, AM/PM and log ratio BPM signal processing schemes [54].

### Orbit Correction and Feedback Systems

When working with colliders one of the most important aims is achievement and maintenance of as high luminosity as possible to give a high number of particle interactions for each bunch collision. As was mentioned in chapter 1 the ILC will aim for peak luminosity to be of the order  $10^{34}m^{-2}s^{-1}$ . Maintenance of a stable beam orbit is essential to achieve delivery of the beam to the interaction point and alongside the use of BPMs combined with manual orbit correction techniques some of the most useful tools for achieving this are position feedback systems. The feedback on nanosecond timescales (FONT) group [55] is developing a fast feedback system for use in the final focus system of the international linear collider. An integral part of this system will be stripline beam position monitors.

### Dispersion Measurement

One source of orbit degradation is known as dispersion. An off momentum particle (i.e.  $\Delta p/p \neq 0$ , where  $p$  is the nominal momentum for a particle at the design energy) is said to follow a dispersive trajectory which is not the same length as the ideal orbit. The horizontal

dispersion function ( $D_x$ ) describes how the displacement of a particle (or beam) varies as a function of its momentum deviation from that of the nominal beam momentum,  $\delta$  [56].

$$\Delta x(s) = D_x(s)\delta \quad (2.18)$$

Where  $\Delta x$  is the horizontal displacement of the beam and  $s$  is the position along the beam-line. One common method used to measure this dispersion function using beam position monitors is by measurement of the beam orbit variation as induced by a change in the RF frequency of the accelerating cavities [57]. It is possible to calculate the dispersion function in this way since the frequency shift causes a change in the relative momentum deviation of the beam,  $\delta$ .

$$\delta = -\frac{1}{\alpha - \gamma^{-2}} \frac{\Delta f}{f} \quad (2.19)$$

Which gives

$$D(s) = (\gamma^{-2} - \alpha) \frac{\Delta x(s)f}{\Delta f} \quad (2.20)$$

Where  $f$  is the RF frequency,  $\alpha$  is the momentum compaction factor and  $\gamma$  the Lorentz factor. Dispersion measurements will be discussed in more detail in chapter 6.

## 2.4 Summary

The importance of the role of beam position monitors in accelerators, especially beam delivery systems, has been demonstrated many times. With technology capable of producing smaller and smaller beams there is increasing demand on BPMs to be of extremely high resolution. Despite vast improvements in cavity BPM technology, stripline BPMs are still very useful to provide fast beam position measurements using relatively simple technology and are capable of achieving micron level resolutions (chapter 3). All three types of BPM

discussed here (button, stripline and cavity) may be found at the ILC, with high resolution cavity BPMs for the final focus system and striplines for the fast feedback system (FONT). BPMs are integral to many accelerator systems and are used for, among other things: orbit measurement, beam based alignment, feedback systems and dispersion measurement.

# Chapter 3

## Stripline Beam Position Monitors for Fast Feedback Systems

The FONT (feedback on nanosecond timescales) group is working on research and development of a fast feedback system for use in future linear colliders such as the ILC. Such a system is designed to provide beam position and angle correction in final focus systems to ensure maximum possible luminosity at the point of collision. This chapter provides an account of measurements performed to assess the properties and performance of the stripline BPMs to be used in a fast position feedback system. Results and conclusions of calibration and resolution measurements performed at the Accelerator Test Facility will be presented.

### 3.1 The FONT Project

It is the aim of the FONT project to provide intra-train position and angle feedback at the interaction region of the ILC; figure 3.1 shows a representation of the proposed layout. This feedback system will be instrumental in compensating for the effects of environmental vibrational noise, both natural (e.g. ground motion) and man made (e.g. machine noise), on beam position. The system will work to align the two incoming beams. For collision of two beams, the position of one of the beams will be measured in the extraction line as it exits the interaction region and a correction applied to the opposing incoming beam [58]. The FONT system can be separated into three sub systems: BPMs with signal processing

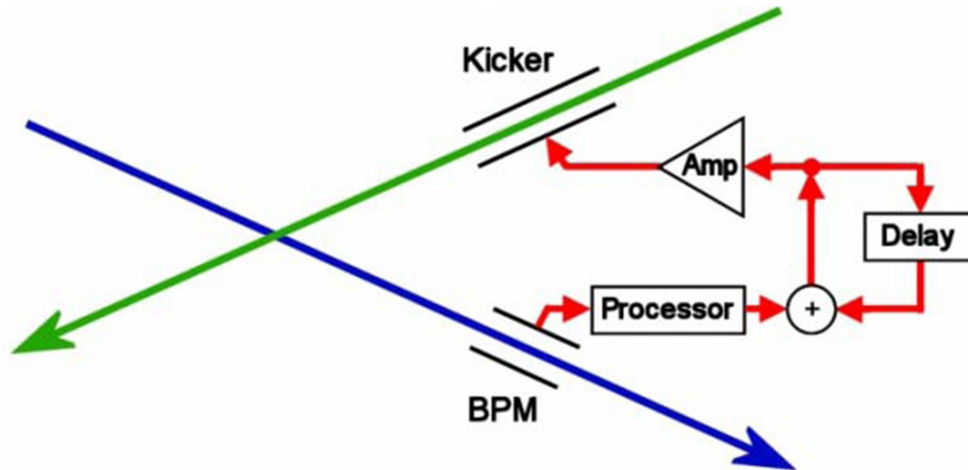


Figure 3.1: Diagram outlining the proposed setup of the FONT system at the international linear collider [59].

electronics, kicker magnets with driving amplifiers and feedback circuits.

### 3.1.1 History

The FONT feedback system has been redesigned several times to allow for improvements and changes in system requirements. It is currently in its 5th incarnation.

#### FONT1

The FONT project was initially created with the Next Linear Collider (NLC) [60] in mind with the first working prototype tested at NLCTA (Next Linear Collider Test Accelerator), SLAC. The most difficult problem to overcome for FONT1 was that of latency. NLCTA had a beam train of length only 177ns and bunch spacing of 88ps [61], requiring a very fast feedback system even to measure the position of the first bunch and correct the position of the last in the train. Figure 3.2 shows a diagram of the setup of FONT1 at NLCTA. The system comprised a fast button BPM (see example in chapter 2), a feedback loop and a kicker, with a measured latency of 66ns for the whole system and 5ns for the BPM processor [62].

Figure 3.3 [49] shows the feedback results of the FONT1 project. The beam was deliberately offset from zero using a dipole corrector magnet placed upstream of the feedback

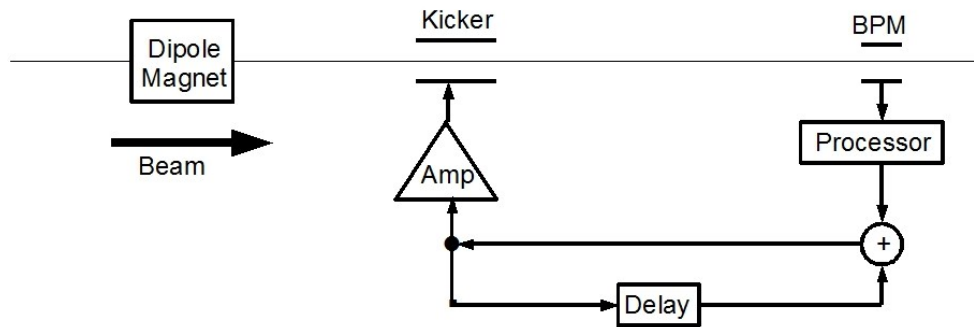


Figure 3.2: Diagram outlining the FONT1 setup at NLCTA.

system (figure 3.2). The main feedback loop was then turned on followed by the delay loop. Figure 3.3b shows the effect of the main feedback loop. It can be seen to begin to move the offset beams to the same position when the kicker is switched on, with feedback achieved at 180ns. The beams then return to their original position since the BPM is now measuring an already corrected position and thus applying too little correction. This issue is resolved by switching on the delay loop (figure 3.3c), the delay loop keeps the original calculated correction until the end of the bunch train [63].

## FONT2

FONT2 [64] was also tested at NLCTA and included several improvements. Two additional BPMs were introduced to allow for independent position monitoring, the distance between the kicker and the feedback BPM was reduced in order to reduce overall system latency, the BPM processor was redesigned to allow online charge normalization using logarithmic amplifiers and a beam flattener (removes static structure) was added [65].

Figure 3.4 shows the feedback results from the FONT2 setup; again the beam was offset from zero using a dipole corrector magnet and the feedback effect observed. FONT2 achieved a total system latency of 55ns and an estimated 18ns for the BPM. The two additional BPMs introduced for FONT2 allowed a measurement of the resolution of the feedback BPM to be made. A resolution of  $15 \mu\text{m}$  was achieved [66].

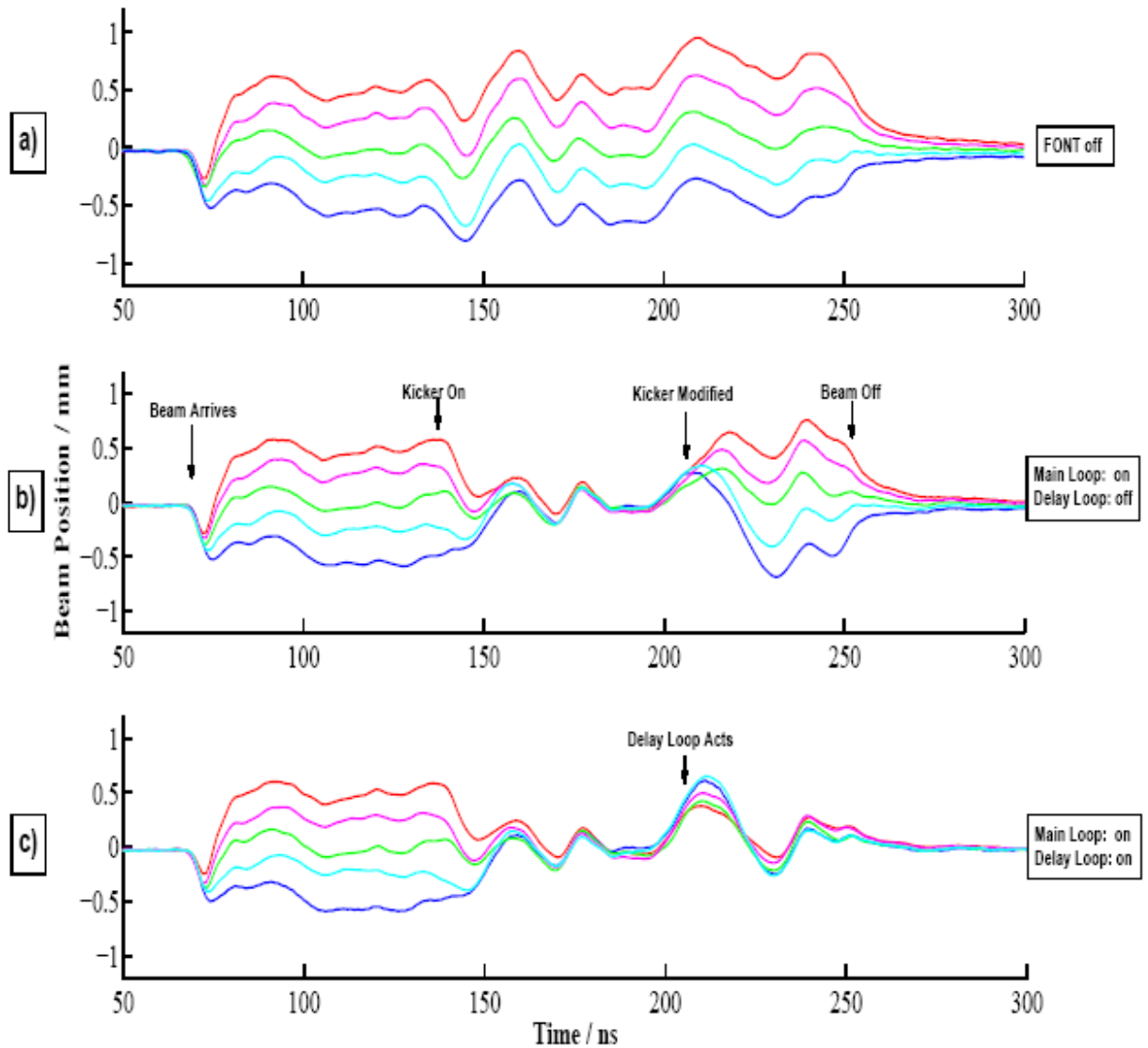


Figure 3.3: Results of the FONT1 feedback system for data taken at NLCTA [49], September 2002. The beam was deliberately offset from zero using a dipole magnet upstream of the feedback system [46]. (a) shows the initial conditions of the beam, (b) the beam position with the feedback switched on and (c) shows the beam position with both the feedback and delay loop on. These plots do not show individual bunch positions since the 88ps bunch spacing is much too short to allow the BPM to resolve individual bunches [63].

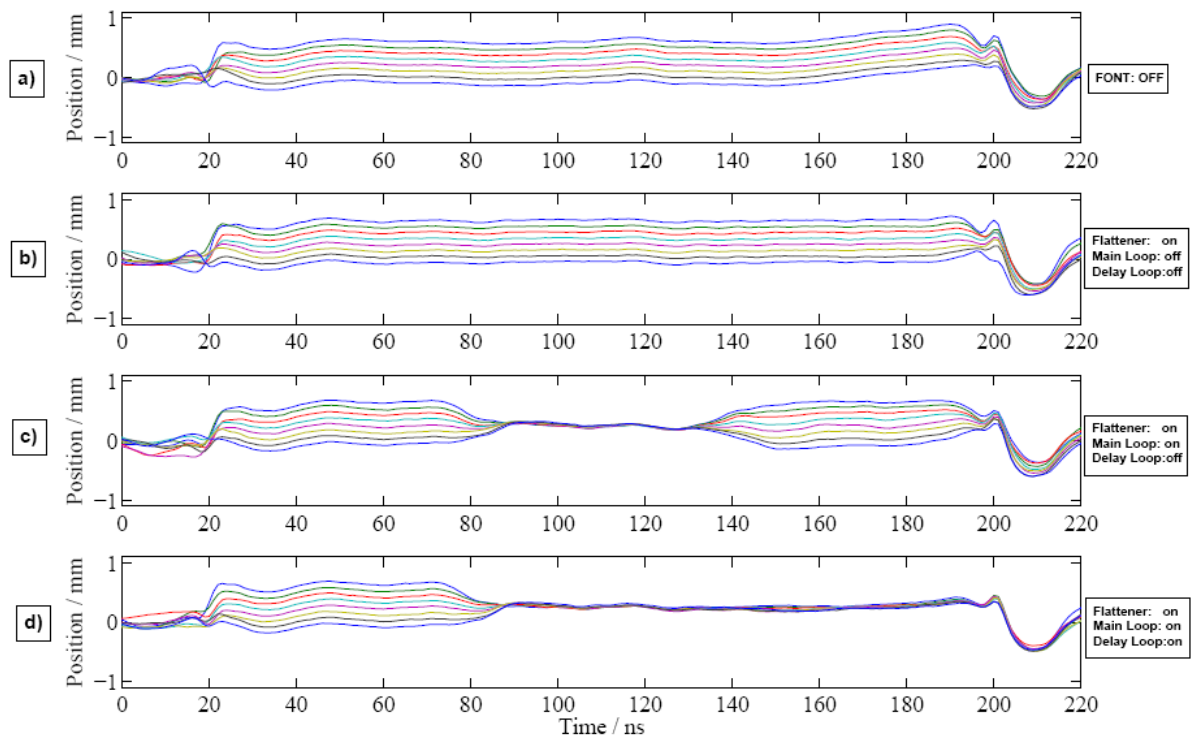


Figure 3.4: Results of the FONT2 feedback system for data taken at NLCTA [49]. (a) shows the initial beam conditions, (b) the beam with the flattener on, (c) the main feedback loop on and (d) shows the effect of the flattener, the feedback loop and the delay loop all in operation.

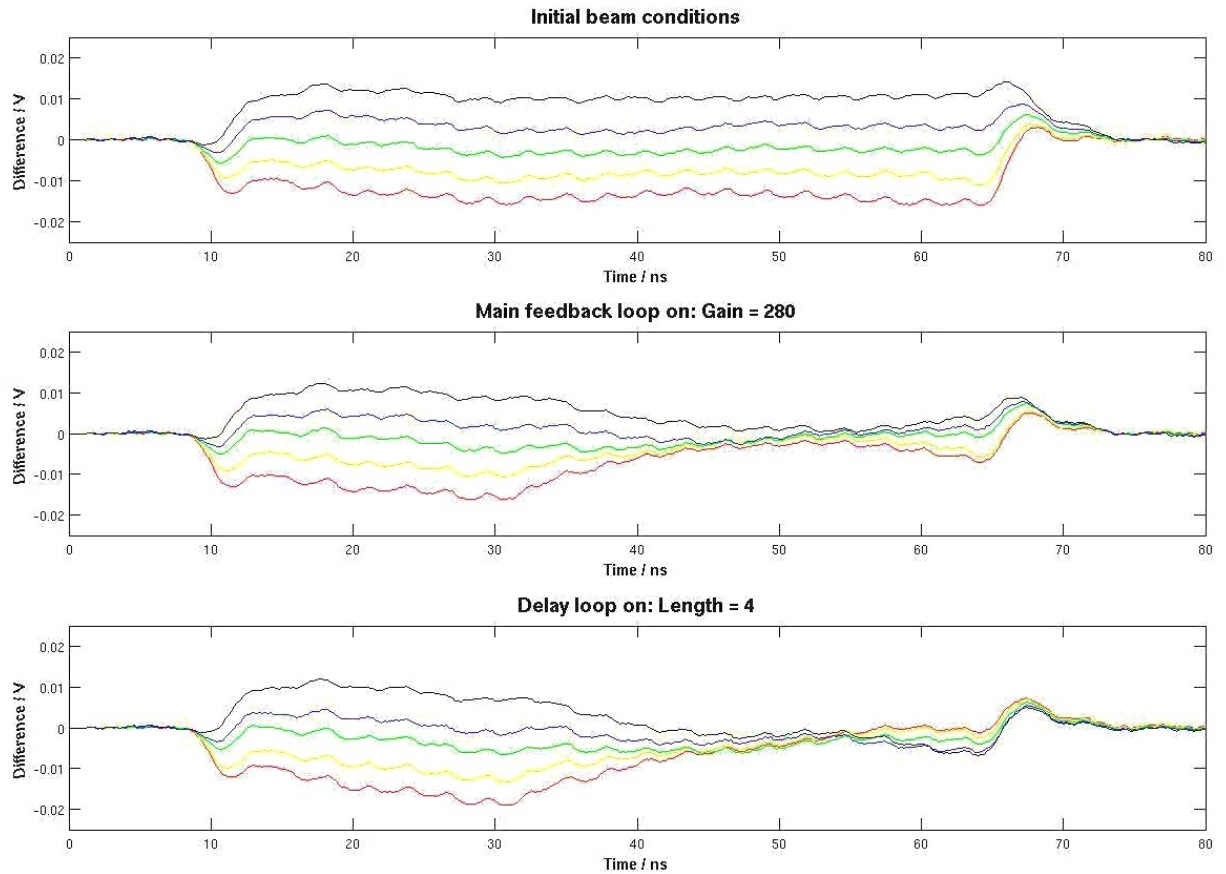


Figure 3.5: Results of the FONT3 feedback system for data taken at ATF [63]. Going from top to bottom data are plot for the following conditions: The initial conditions of the beam, the beam position with the feedback switched on and the beam position with both the feedback and delay loop on.

### FONT3

The third generation of FONT, FONT3 [67], saw a move to ATF where the electron beam is much closer to the beam conditions expected at a future linear collider (smaller and more stable) [66]. The ATF installation again consisted of three BPMs (one for feedback), one kicker and one set of feedback electronics. The BPMs for FONT3 were stripline BPMs (see chapter 2) with difference-over-sum processing electronics and no charge normalization (as opposed to the slower logarithmic amplifier method used to obtain a charge normalized position signal in FONT2). Use of stripline BPMs allows fast, high resolution beam position measurements (see chapter 2) and the use of the sum-over-difference method without charge normalization serves to reduce the latency of the system. Figure 3.5 shows the feedback results. FONT3 achieved a BPM resolution of  $15 \mu\text{m}$  [63] and a latency of 23ns [58],

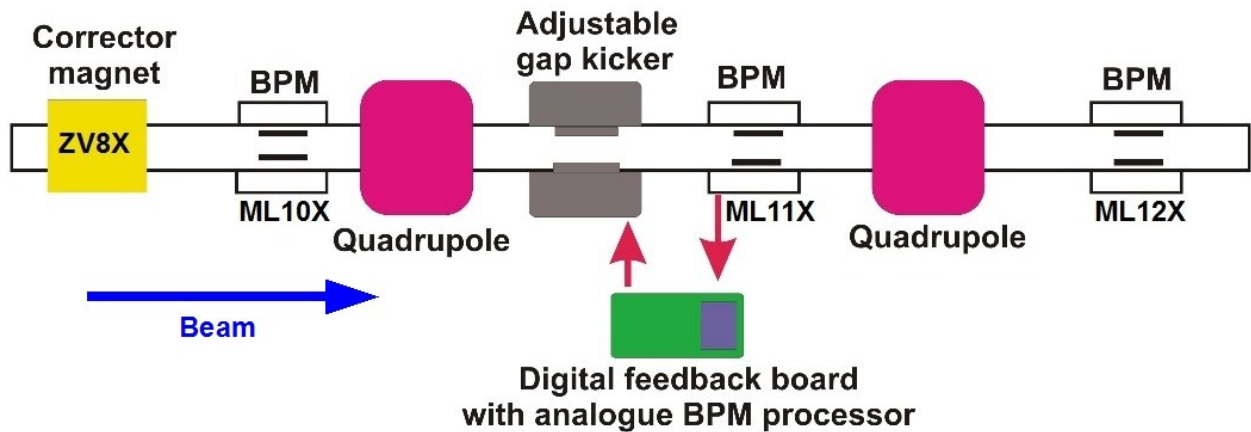


Figure 3.6: Diagram outlining the FONT 4 setup at ATF, detailing the major components of the system and the surrounding beamline. The quadrupoles shown were switched off during calibration to simplify beam optics calculations.

approximately 6ns of which was attributed to the BPM processor [63].

## FONT4

With a view to concentrate on FONT as an ILC prototype, FONT4 [68] saw a move to digital feedback electronics. Cold machines like the ILC have larger bunch spacing (370 ns [4]) than proposed warm machines (eg. NLC, 1.4 ns [69]) allowing the use of slower, but more accurate, digital electronics. The FONT4 system was set up as shown in figure 3.6 with a three bunch beam having a bunch spacing of 154 ns. The feedback results are shown in figure 3.7. FONT4, with particular attention paid to the BPM setup, will be discussed in more detail in sections 3.1.2 and 3.2.

## FONT5

FONT5 [70] is currently under development at ATF2 and will provide both vertical position and angle correction of the beam. It will incorporate the electronics for the two BPMs and two kickers (one for  $y$  and one for  $y'$  orbit correction) required for these two types of feedback in to one central digital system. This recent upgrade will be discussed briefly at the end of this chapter.

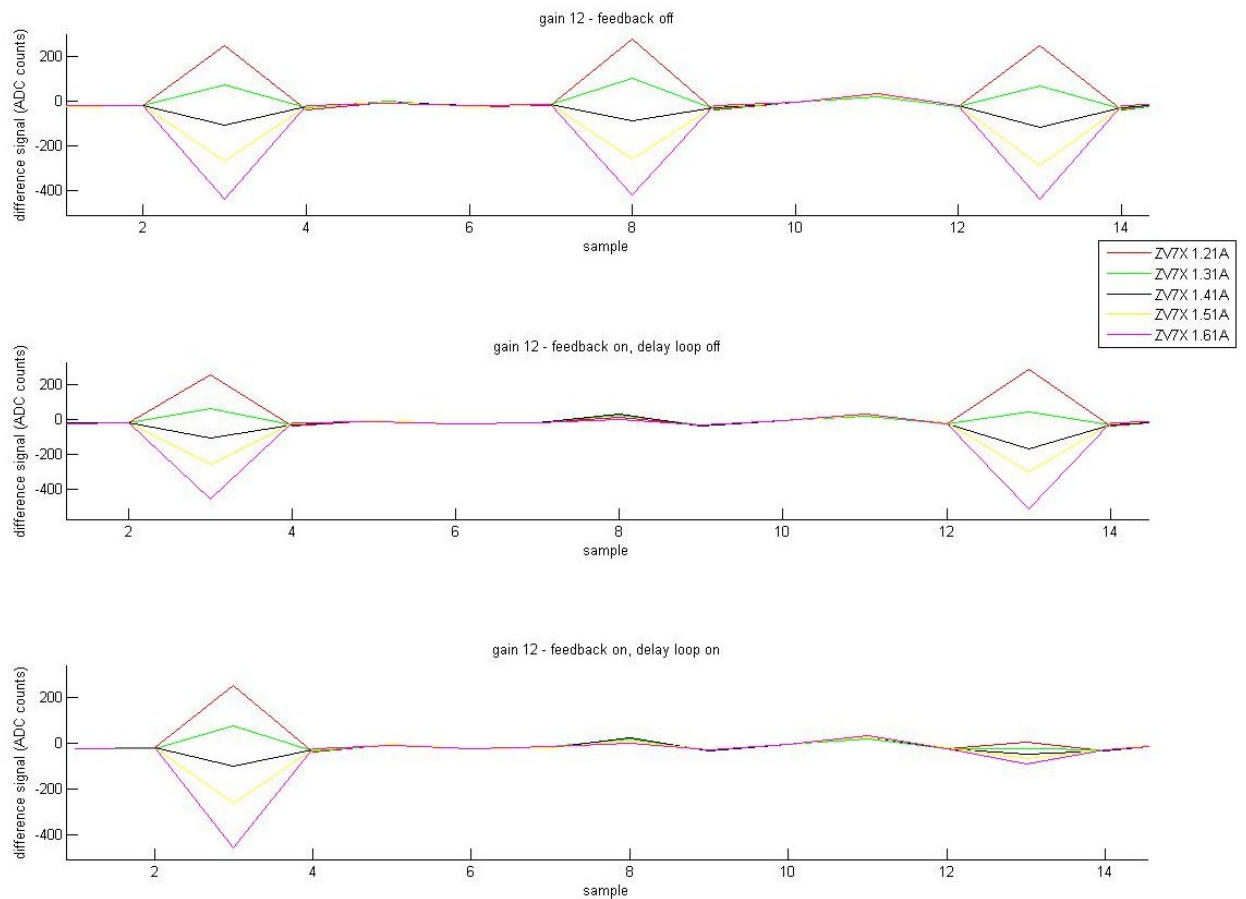


Figure 3.7: Results of the FONT4 feedback system for data taken at ATF [71]. Going from top to bottom data are plotted for the following conditions: feedback and delay loop off (i.e initial beam conditions); feedback on, delay loop off; both feedback and delay loop on. Each plot shows the individual positions of each of three bunches separated by 154ns giving a sample time of approximately 31ns (x-axis). This data is not normalized with respect to charge and so, whilst showing the effectiveness of the feedback system, gives only relative position in ADC counts.

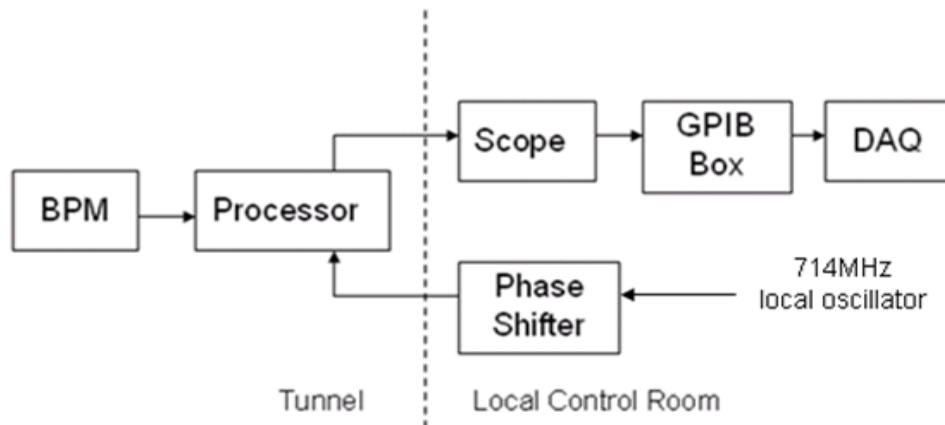


Figure 3.8: Block diagram of BPM hardware setup at ATF.

### 3.1.2 Testing of the FONT4 Prototype System at ATF

The FONT4 system was set up on the extraction line of ATF, as shown in figure 3.6. The test setup consisted of a dipole corrector magnet (denoted ZV8X), three stripline BPMs (denoted ML10X, ML11X and ML12X) with processing electronics, an adjustable gap kicker and the digital feedback board. Of the three BPMs ML11X was used as an input to the feedback board with the other two acting as witness BPMs for monitoring the effect of feedback on the beam. This experiment involved the use of only one beam as opposed to the ILC setup using two beams. For the purposes of feedback a three bunch train was used with bunch separation of 154ns.

As the beam passes through ML11X the vertical position of the first bunch in the train is measured and the information passed to the digital feedback board where it is sampled, digitized and processed and subsequently outputs an analogue correction signal [72]. This signal is then passed to an amplifier which is used to drive the kicker. The magnet then applies a kick in an attempt to move the second bunch to the nominal position. The process is then repeated measuring the second bunch and using the position information from both bunches one and two to correct the orbit of the third bunch.

## 3.2 Beam Position Monitors and Signal Processing Electronics

The advantage of having three BPMs is that it allows a more detailed investigation into their properties than would be possible with less than three BPMs, for example it allows their resolution to be measured.

The investigation into the performance of the beam position monitors was done using all three BPMs and independent of the feedback function of the FONT system. Figure 3.8 shows a block diagram of the experimental setup with the processing electronics situated next to the beamline and the DAQ system situated in the local control room. The data were acquired using an oscilloscope and recorded using a MATLAB <sup>®</sup> [73] based GUI (graphical user interface) [74], where it could be analyzed offline.

### 3.2.1 ATF Stripline BPMs

The BPMs used for this experiment had an aperture of radius 1.35 cm with 12 cm long copper striplines of width 1.65 cm. A photograph of one of the striplines, which is currently installed at ATF2, can be seen in figure 2.3 and an engineering drawing can be seen in figure 3.9. The stripline signal was picked off at the upstream end of the BPM and input to the FONT analogue electronics. An example of a raw BPM signal which will be input to the BPM processor was seen in figure 2.5.

### 3.2.2 Analogue BPM Processing Electronics

Figure 3.11a is a photograph of one of the BPM processors used for FONT4 at ATF, and 3.11b shows a block diagram representation of the analogue processor design. The signals from each of the two striplines (figure 2.5) are input to the processor where they are first split and then filtered using low pass filters to remove high frequency components. One half of each filtered stripline signal is passed to a 180° power combiner the output of which

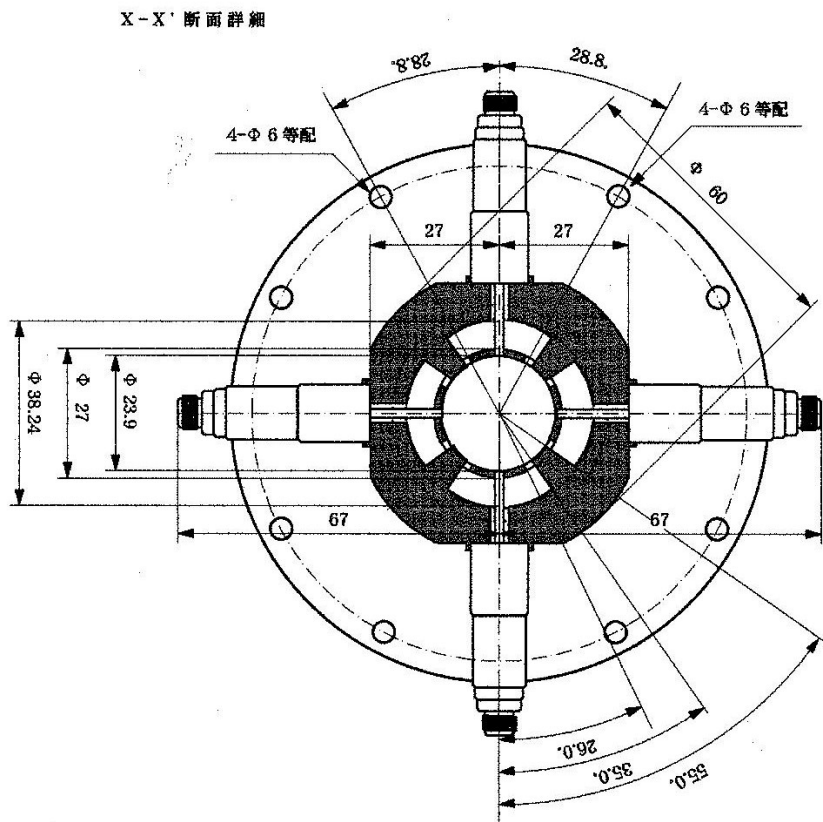


Figure 3.9: Cross sectional technical drawing of stripline BPM installed at ATF [75].

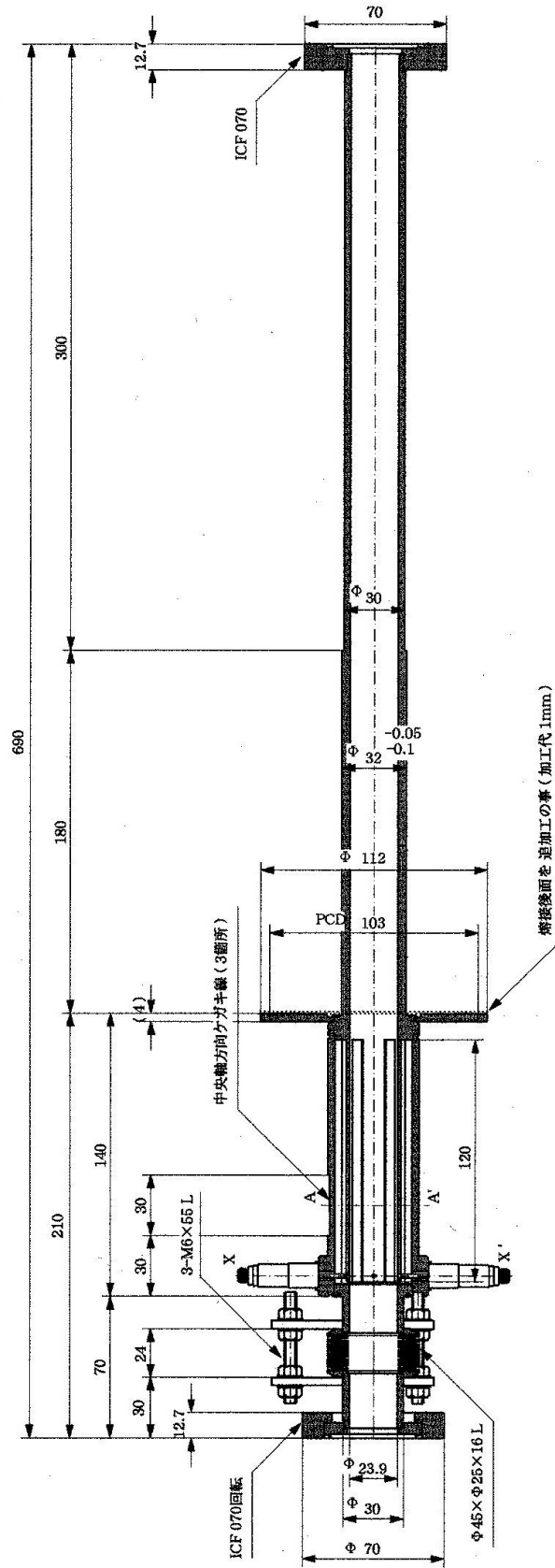


Figure 3.10: Technical drawing showing the longitudinal view of one of the stripline BPMs installed at ATF [75].

is then filtered using a band pass filter (BPF). The band pass filter serves to reduce the bandwidth of the signal and broaden the output of the processor to allow accurate sampling of the peak by the digital feedback electronics [76]. The signal output from the BPF is then down mixed with a 714 MHz local oscillator (LO) signal (which is locked to the beam) to give a difference signal output, this essentially gives  $V_1 - V_2$  as described in equation 2.12. Meanwhile the other half of the signals are summed, and the output filtered and mixed as done for the difference signal, giving  $V_1 + V_2$  as in equation 2.11.

### Processor Output Signals

An example of the output of the processor can be seen in figure 3.12. The signals in black are the raw (a) sum ( $V_1 + V_2$ ) and (b) difference ( $V_1 - V_2$ ) measured directly at the processor output using an oscilloscope. The form of this signal is of two peaks, the smaller of which is attributed to the quadrature phase ( $Q$ ) component of the BPM output and the more prominent peak is a measure of the in-phase ( $I$ ) component [76] where

$$I = A(t) \cos(\phi(t)) \quad (3.1)$$

$$Q = A(t) \sin(\phi(t)) \quad (3.2)$$

where  $A$  and  $\phi$  are the amplitude and phase of the signal. One structure apparent in these signals is that of the baseline noise which is caused in the most part by leakage of the 714MHz LO signal into the sum and difference output channels (the LO input is very close to the sum and difference outputs, see figure 3.11a) and thermal noise from both the BPM and the processor (this contribution is in general less significant than the LO leakage). It is possible to remove some of this noise from the signal after the fact by subtracting a running average over the pulse from the signal, as follows

$$y(n) = \frac{1}{M} \sum_{k=0}^{M-1} x(n-k) \quad (3.3)$$

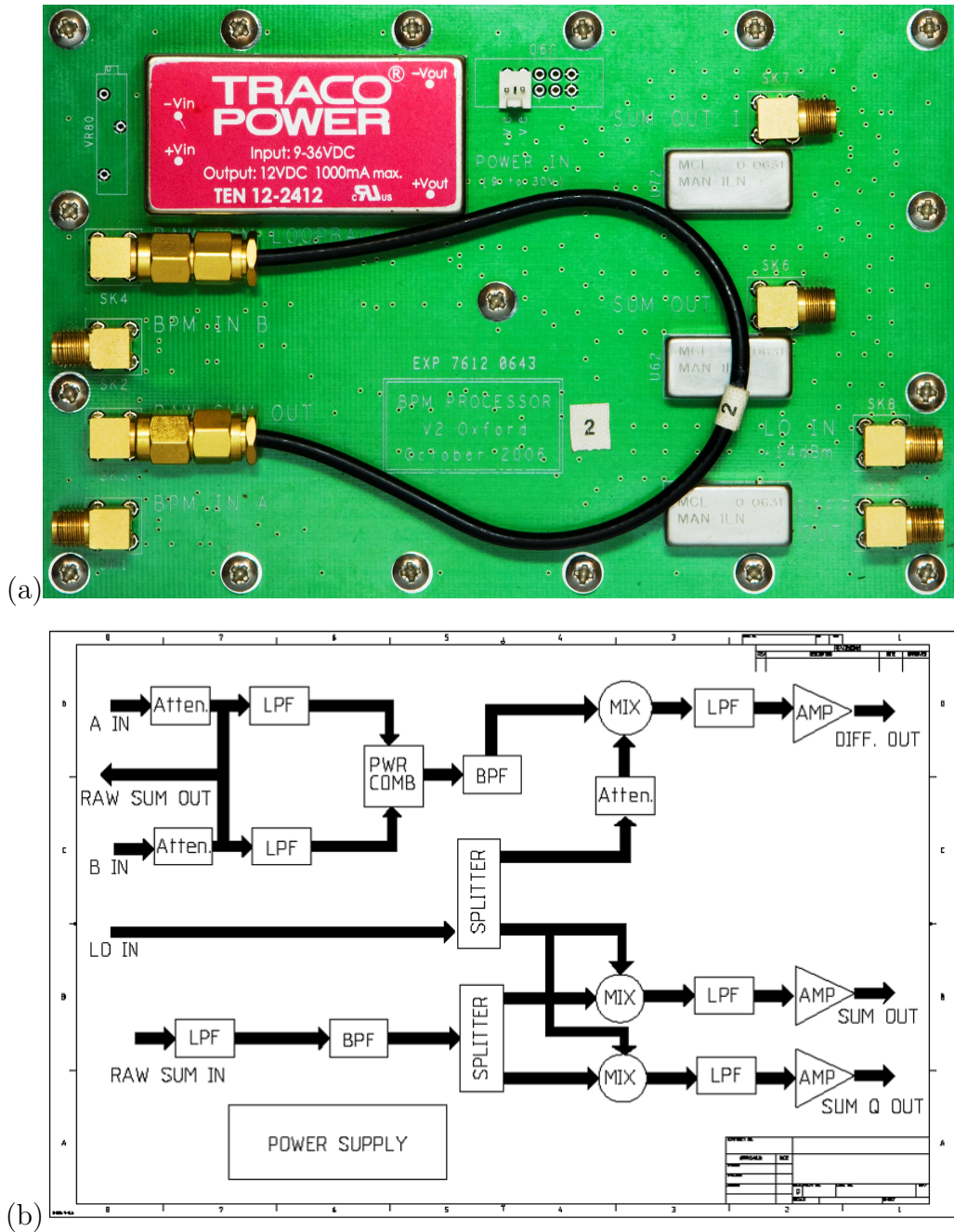


Figure 3.11: (a) Photo of one of the analogue BPM processors used in the FONT feedback system. (b) Block diagram representation of FONT analogue BPM [77].

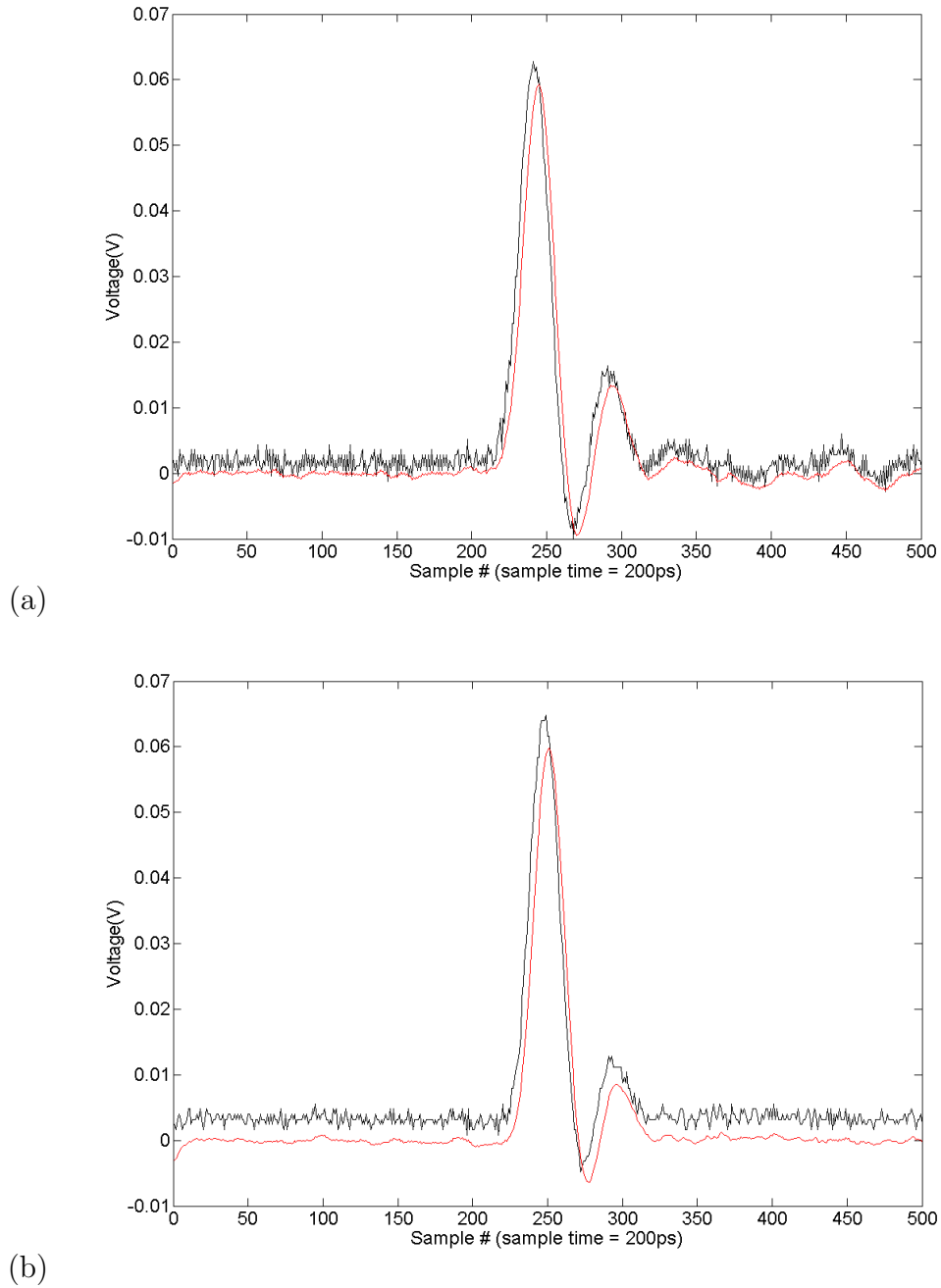


Figure 3.12: An example of the (a) sum ( $V_1 + V_2$ ) and (b) difference ( $V_1 - V_2$ ) outputs from one of the FONT analogue processors. The black traces are the raw processor output and the red traces are these signals after some of the noise has been filtered out (equation 3.3).

Latency Type	Source	Time(ns)
Irreducible	Time of flight from kicker to BPM	7
	Signal propagation delay (cables)	15
Reducible	BPM processor	10
	Digital processor	68
	amplifier	40
Total		140

Table 3.1: FONT4 latency budget [58].

where  $M$  is the number of points to average (in this case 7 to remove any 714MHz component in the sum and difference signals). In other words every point in  $y(n)$ , will be the average of the last  $M$  points in  $x(n)$  [78]. The signals shown in red in figure 3.12 are the signals after the running average has been performed and any baseline offset removed.

The beam position is then taken to be the difference output signal from the processor divided by the sum signal output. This charge normalization (divide by sum signal) is not performed using the BPM electronics (see chapter 2). In the case of the BPM used for feedback it is done using the digital feedback electronics and for the purposes of this study is performed using software analysis written in MATLAB [73].

## Latency

The most important goal of the processor development is to have as low latency as possible whilst maintaining high resolution. For ATF the maximum bunch spacing available is 154 ns meaning that the overall latency of the feedback system should be no higher than 140 ns in order to perform feedback at the individual bunch level. Table 3.1 [58] shows the latency budget for the FONT4 system at ATF. The budget allows for no more than 10ns latency for the BPM processor.

Figure 3.13 shows the results of processor latency measurements performed in the lab. The green oscilloscope trace is the signal that was input to the processor, this was created using a pulse generator, and the blue trace is the processor difference signal output. The latency was taken to be the difference between the two peaks and was measured to be 10.6

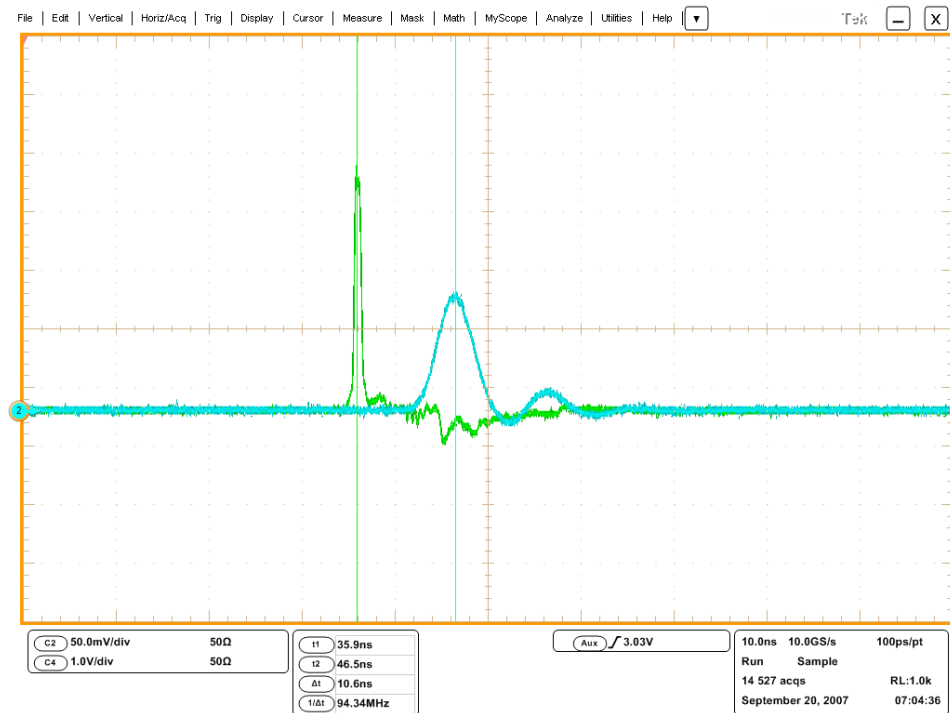


Figure 3.13: Oscilloscope trace showing the measured latency value of the processor to be 10.6 ns. The green line represents the signal input to the processor and the blue line the output.

ns. This is over 4 ns slower than the BPM processors used for FONT3 due to the extra filtering used to broaden the processor output pulse [76].

### 3.3 BPM Calibration

Calibration of the beam position monitors was done using a corrector magnet positioned 5.78 m [79] upstream of the first BPM (ML10X) with each BPM separated by 2.2m. The beam was moved across the beampipe in the  $y$ -direction (vertical) by varying the current in the corrector magnet. Data were collected at intervals of 0.1 A over a range of 1.6 A, (from -1.5 A to 0.1 A), which corresponds to movement in the  $y$ -direction of 1.8 mm (see equations 3.4 and 3.7) in ML10X; data were taken for 50 pulses at each magnet current setting; the data taken when the corrector current is set to -0.4A is not used here due to corruption of the data file. These data give a measure of BPM signal as a function of magnet current. The change in magnet current can then be related to the change in beam position by calibration

of the magnet with respect to a known BPM or by measurement of the magnetic field. For example

$$\theta_{kick} = kI \quad (3.4)$$

where  $\theta_{kick}$  is the angle by which the beam is deflected,  $I$  is the current in the magnet and  $k$  depends on the magnet properties and the beam momentum. This information can then be used in conjunction with optics calculations to predict the position of the beam at the BPM in question. A change in position of the beam at the corrector magnet (i.e. when the magnet current is varied) may be used to predict the change in position of the beam at the BPM location. For this the accelerator lattice, described by the Twiss matrix [80], must be considered.

$$\begin{pmatrix} y_2 \\ y'_2 \end{pmatrix} = \widehat{M} \begin{pmatrix} y_1 \\ y'_1 \end{pmatrix} \quad (3.5)$$

For the purposes of this investigation all quadrupoles (and any other focusing magnets) in the region of the BPMs (figure 3.6) were switched off to simplify these optics calculations with a twiss matrix for a drift length (field free region) as follows [81]

$$\widehat{M}_{drift} = \begin{pmatrix} 1 & \Delta s \\ 0 & 1 \end{pmatrix} \quad (3.6)$$

This simplification means that the beam position may then be calculated as

$$y_{bpm} = \Delta s_{dip-bpm} \tan(\theta) \quad (3.7)$$

where  $y_{bpm}$  is the vertical position of the beam at the BPM in question,  $\Delta s_{dip-bpm}$  is the distance between the BPM and dipole corrector magnet and  $\theta$  is the angle of the beam's trajectory.

The calibration constant,  $C$ , is the value by which the difference-over-sum output must be divided in order to convert the position in Volts to the position in metres. It is possible to calculate the theoretical calibration constant through measurement of the gain over each set

of processing electronics. This gives a reasonable estimate of the experimental calibration constant [82].

$$C = \left( \frac{g_{diff}}{g_{sum}} \right) \frac{2}{r} \quad (3.8)$$

where  $g_{diff}$  and  $g_{sum}$  are the electronics voltage gain in the difference and sum processor channels respectively. The voltage gain in dB is given by

$$g = 20 \log_{10} \left( \frac{V_{out}}{V_{in}} \right) \quad (3.9)$$

where  $V_{in}$  and  $V_{out}$  are the voltage of the processor input and output signals respectively. The design specifications of the electronics give the gain ratio to be approximately 20 [83], and so with a BPM aperture of radius  $r = 14$  mm [75] the estimated calibration constant,  $C \approx 2.9 \text{ mm}^{-1}$  (equation 3.8).

### 3.3.1 Calibration Results

The first step of data analysis is to remove the noise, as was outlined in section 3.2.2. The next step is to perform the difference-over-sum calculation (equation 2.13) where the sum and difference are taken to be

$$\Sigma = \sum_{j=1}^n \sigma_j(t) - \bar{\sigma}_j(t) \quad (3.10)$$

and

$$\Delta = \sum_{j=1}^n \delta_j(t) - \bar{\delta}_j(t) \quad (3.11)$$

where  $\sigma_j$  and  $\delta_j$  are the elements of the moving average of the processor output signals (equation 3.3) and where  $j = 1, 2, 3, \dots, n$  and  $n$  is the number of oscilloscope samples in the waveform. After determining the sum and difference values a line is fit to the difference-over-sum ( $\Delta/\Sigma$ ) vs beam position (as calculated from the magnet current, equations 3.4 and 3.7), and the gradient taken to be the calibration constant,  $C$  (equation 3.8), or scaling factor to be used to relate signal output to beam position.

Figure 3.14 shows the calibration results yielding calibration constants,  $C$ , of  $-2.84 \pm$

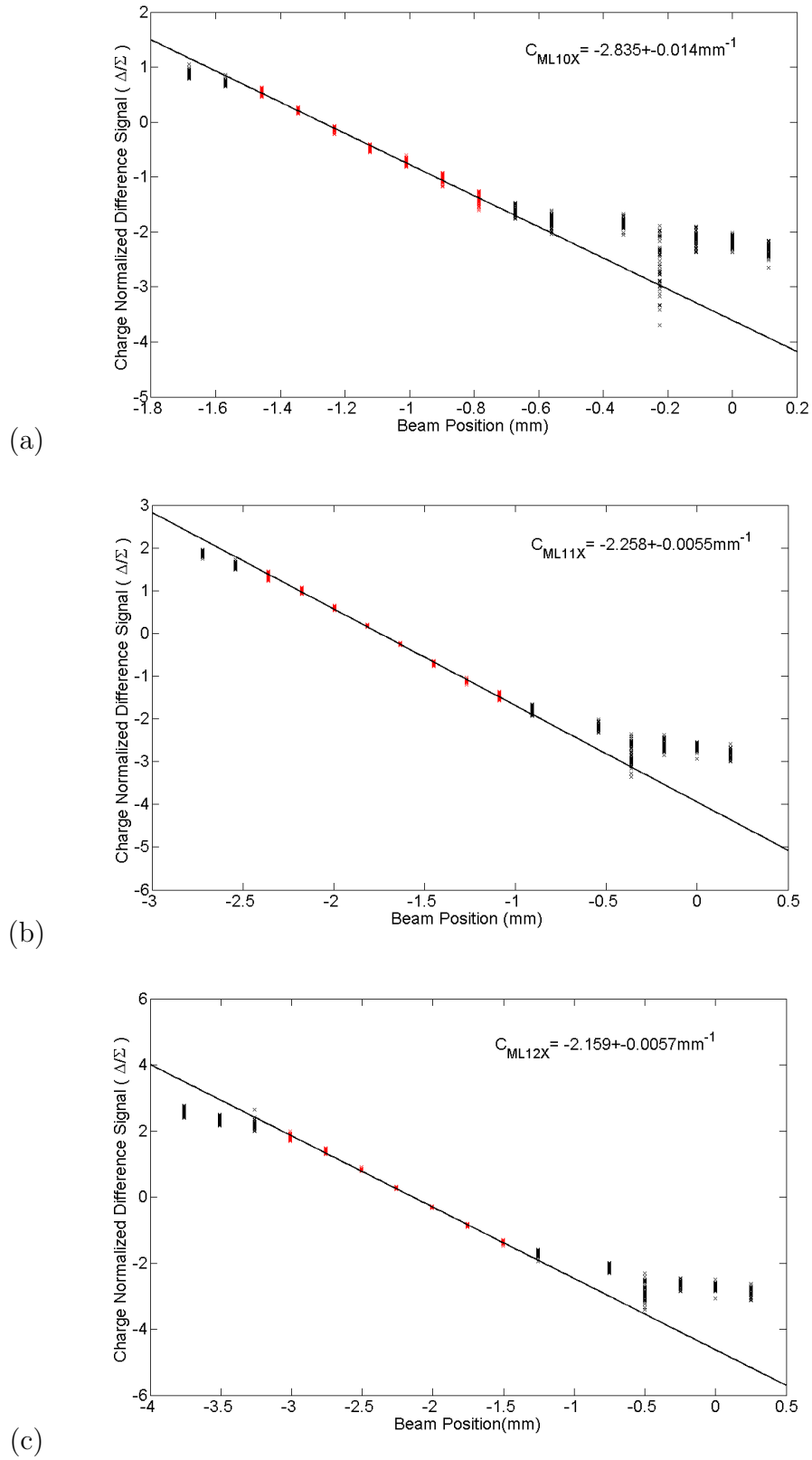


Figure 3.14: Difference-over-sum vs beam position calculated from corrector magnet current (equation 3.7) for each of the three BPMs, 50 pulses are plotted for each beam position. The region shown in red is the range over which the line has been fit.

I (A)	BPM											
	ML10X				ML11X				ML12X			
	$\Sigma$ (mV)	$\delta\Sigma^*$	$\bar{y}$	$\delta y^*$	$\Sigma$ (mV)	$\delta\Sigma^*$	$\bar{y}$	$\delta y^*$	$\Sigma$ (mV)	$\delta\Sigma^*$	$\bar{y}$	$\delta y^*$
-1.5	15	5	0.9	17	63.5	5	1.86	6	65.5	5	2.57	7
-1.4	15.6	6	0.72	20	66.6	6	1.58	7	68.3	7	2.33	8
-1.3	13.7	18	0.54	17	59.5	16	1.34	8	60.6	16	2.19	15
-1.2	14	17	0.21	28	60.7	16	0.98	13	61.1	15	1.81	9
-1.1	14	25	-0.14	18	61.3	20	0.59	9	62.1	21	1.37	8
-1	14	5	-0.48	16	67	5	0.18	16	67.7	5	0.82	9
-0.9	15	7	-0.72	15	65.7	7	-0.25	13	66.2	8	0.27	11
-0.8	13.1	12	-1.03	14	56.7	10	-0.71	9	57	10	-0.32	10
-0.7	12.9	9	-1.41	13	55.5	8	-1.11	8	55.6	8	-0.87	7
-0.6	14	9	-1.63	10	60.1	9	-1.47	7	60.4	9	-1.37	8
-0.5	13.3	14	-1.8	11	57.7	13	-1.79	8	58.3	13	-1.74	10
-0.3	15.7	8	-1.83	10	65.7	10	-2.16	7	66.1	9	-2.12	7
-0.2	9.8	52	-2.61	32	44.1	40	-2.8	18	44.7	36	-2.87	20
-0.1	14.3	11	-2.12	11	59.6	11	-2.6	9	60.3	10	-2.62	8
0	15.2	11	-2.7	8	63.7	10	-2.67	7	64.3	10	-2.71	11
0.1	14.4	9	-2.88	11	61.2	9	-2.83	7	62.3	8	-2.88	9

Table 3.2: Mean and variation (\*as percentage of mean) of beam charge ( $\bar{\Sigma}$ ,  $\delta\Sigma$ ) and vertical position ( $\bar{y}$ ,  $\delta y$ ) as measured by the three BPMs during the calibration procedure (figure 3.14), where  $y = \Delta/\Sigma$ . Twenty consecutive electron bunches, for each magnet current setting, were used for this measurement.

0.014 mm<sup>-1</sup>,  $-2.26 \pm 0.0055$  mm<sup>-1</sup> and  $-2.16 \pm 0.0057$  mm<sup>-1</sup> for BPMs ML10X, ML11X and ML12X respectively. The region shown in red is the range over which the line has been fit. The data begins to deviate from the fitted line when the stripline signal becomes too large and the processor output response becomes non-linear. The calibration constants measured here vary between each BPM. Since this constant should be a property of the processing electronics only [83] (equation 3.9), the variation suggests the three processors are not identical. Table 3.2 shows, for each BPM at each corrector magnet current setting, the mean and variation of sum signal ( $\bar{\Sigma}$ ,  $\delta\Sigma$ ) and the mean and variation of vertical position ( $\bar{y}$ ,  $\delta y$ ), where  $y = \Delta/\Sigma$ . It can be seen that (table 3.2) the sum signals for ML10X is significantly smaller in amplitude than those seen from ML11X and ML12X suggesting a possible malfunction of ML10X. These differences in the processor output will be considered in section 3.4.2.

## 3.4 BPM Resolution

As described in chapter 1, in order to bring two beams into collision at the ILC it is necessary to have nanometre beam position accuracy. This accuracy of position feedback at the interaction point requires the feedback BPM to have micron resolution [84]. This section will outline two methods for determining BPM resolution and their experimental results. As an integral part of the position feedback system it is desirable that the BPM be capable of measuring the beam position as accurately as possible. The BPM is a contributing factor to the overall noise of the feedback system and bad resolution in turn causes a higher noise figure of the feedback system which reduces the accuracy to which the beam position can be corrected.

### 3.4.1 Three BPM Method

In this method two BPMs are used to predict the position of the third; the resolution is taken to be the standard deviation of the residual between this predicted position and the

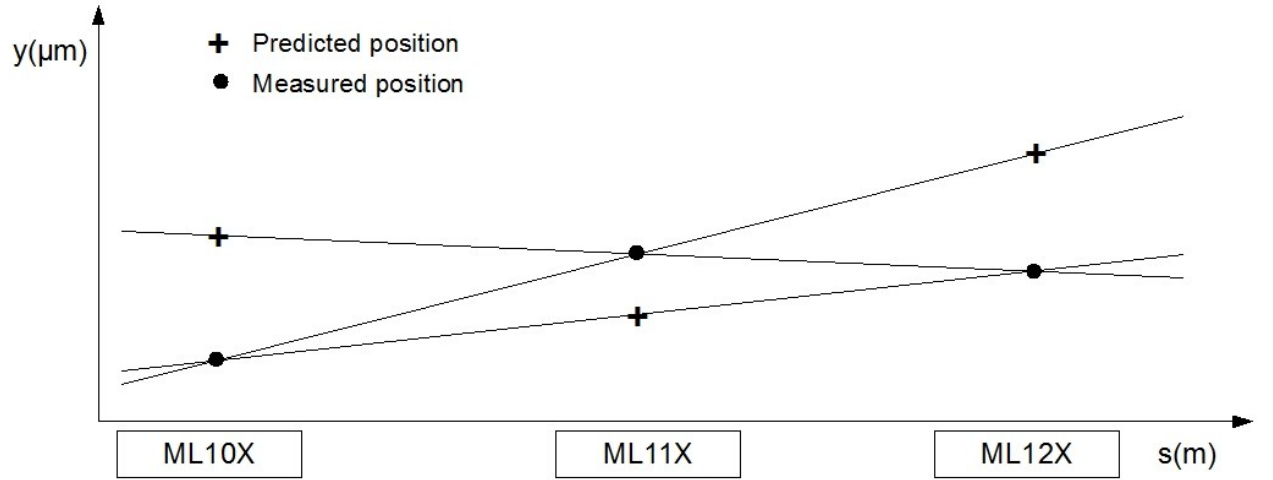


Figure 3.15: Diagram to show how the predicted position of a third BPM is given by fitting the positions measured by the other two.

position as measured by the third BPM. This method is represented in figure 3.15 where the predicted position may be calculated geometrically as follows [85];

$$y_j = y_i + \frac{s_{ij}}{s_{ik}}(y_k - y_i) \quad (3.12)$$

Where  $y_i$  represents the true position of the beam in the  $i$ th BPM and  $s_{ij}$  is the distance between the BPMs  $i$  and  $j$ . Considering the case in which the three BPMs are evenly spaced (as is true in this particular case) we get the following simplified expression, where  $y_2$  represents the position of the beam in the middle BPM.

$$y_2 = \frac{1}{2}(y_1 + y_3) \quad (3.13)$$

We can then define the position in this BPM, as predicted by the two outer, to be

$$y_2^P = \frac{1}{2}(y_1^m + y_3^m) \quad (3.14)$$

Where  $y^P$  represents the predicted position and  $y^m$  the measured position which may be represented as

$$y_2^m = y_2 + r_2 + \text{const} \quad (3.15)$$

where  $y_2$  is the true position of the beam and  $r_2$  is a variable that is a member of the distribution whose standard deviation is equal to that of the resolution of the BPM. The residual between the measured and predicted position for the middle BPM is given by

$$\delta y_2 = y_2^m - y_2^P \quad (3.16)$$

substituting for  $y_2^m$  gives

$$\delta y_2 = \left( y_2 - \frac{1}{2}(y_1 + y_3) \right) + \left( r_2 - \frac{1}{2}(r_1 + r_3) \right) + const \quad (3.17)$$

$$\sigma_2 = std(\delta y_2) = \sqrt{std(r_2)^2 + \frac{1}{4}std(r_1)^2 + \frac{1}{4}std(r_3)^2} = R_2 \sqrt{1 + \frac{R_1^2}{4R_2^2} + \frac{R_3^2}{4R_2^2}} \quad (3.18)$$

where  $R$  is the resolution of the BPM. Applying the assumption that each of the three BPMs is identical to the others, and so have the same resolution, a simplified expression exclusive to the central BPM of the three BPM system may be written:

$$R_2 = \frac{\sigma_2}{\sqrt{\frac{3}{2}}} \quad (3.19)$$

This process may be repeated for the outer two BPMs and written more generally as [85]

$$R_i = \frac{\sigma_i}{\sqrt{1 + \frac{s_{ij}R_j^2}{s_{jk}R_i^2} + \frac{s_{ik}R_k^2}{s_{jk}R_i^2}}} \quad (3.20)$$

## Results

Data were taken for 300 pulses with the beam held at a constant position near to the centre of the BPMs. The data were then processed as stated above to give the results presented in figure 3.16. Figure 3.16 shows the distribution of residuals for which the standard deviation of the distribution is the resolution of the three BPM system. Application of equations 3.12

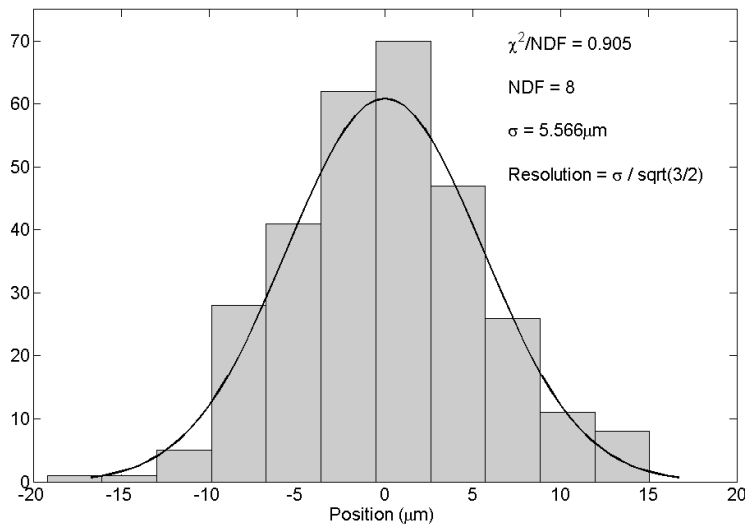


Figure 3.16: Measured distribution of residuals. Since this method assumes the BPM resolution to be the same for all three BPMs the distribution of residuals (difference between measured and predicted positions) is also the same.

- 3.20 gives the resolution of the system to be  $4.46 \pm 0.04 \mu\text{m}$ . The fit is a Gaussian fit to illustrate how normally distributed the beam position data are. The error arises from the fit error in figure 3.16.

Figure 3.17 shows a simulation of the effect of using this method to determine resolution on non-identical BPMs. The input resolution arising from simulated beam positions was taken to be the standard deviation of generated Gaussian position distributions and the output calculated as outlined at the beginning of this section. The input for BPMs 1 and 2 were varied between 1 and 10 (i.e. the standard deviation of gaussian distributions of beam position, in arbitrary units) whilst the input for BPM3 remained constant (with a distribution of standard deviation equal to one). It can be seen that use of non-identical processors yields varying resolutions dependent on the difference in input and the arrangement of the BPMs.

### 3.4.2 Multiple Processor Method

Another method used to obtain resolution information is to input identical signals to each set of BPM processing electronics. The output signals from ML12X were split and then

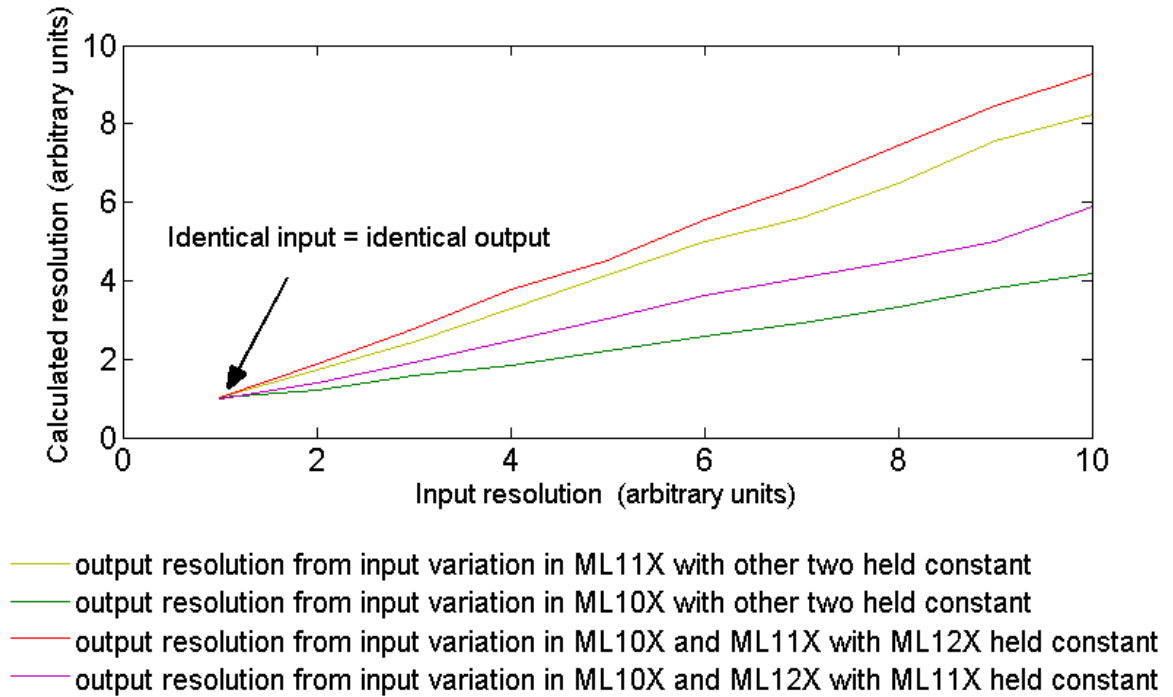


Figure 3.17: Output vs input resolution as calculated using the three BPM method for simulated beam position distributions. The input distributions were varied to simulate the results of using the three BPM method with non-identical BPMs.

input to four (one for each of the three BPMs and one spare) BPM processors (denoted P1, P2, P3 and P4) and the calibration procedure previously described was performed. Figure 3.18 shows the calibration curves for each of the four processors, yielding constants of  $-2.774 \pm 0.007 \text{ mm}^{-1}$ ,  $-7.329 \pm 0.078 \text{ mm}^{-1}$ ,  $-2.709 \pm 0.0074 \text{ mm}^{-1}$  and  $-2.711 \pm 0.0062 \text{ mm}^{-1}$  for processors P1, P2, P3 and P4 respectively. These calibration data have larger linear regions than those for the three BPM case since the outputs from ML12X were split four ways, to be input to the four processors, reducing the voltage of the input signals and therefore increasing the linearity of the processor output with respect to beam position. The calibration constants for P1, P3 and P4 are much more consistent than those measured in the three BPM method (figure 3.14) suggesting a contribution from the BPMs (if the striplines were not identical) or possibly a change in the beam properties (for example beam coupling or dispersion arising from dipole magnets present between the BPMs) between each BPM. This splitting method removes any differences between the BPMs giving a better idea of the differences between the processors. Although every effort has been made to use

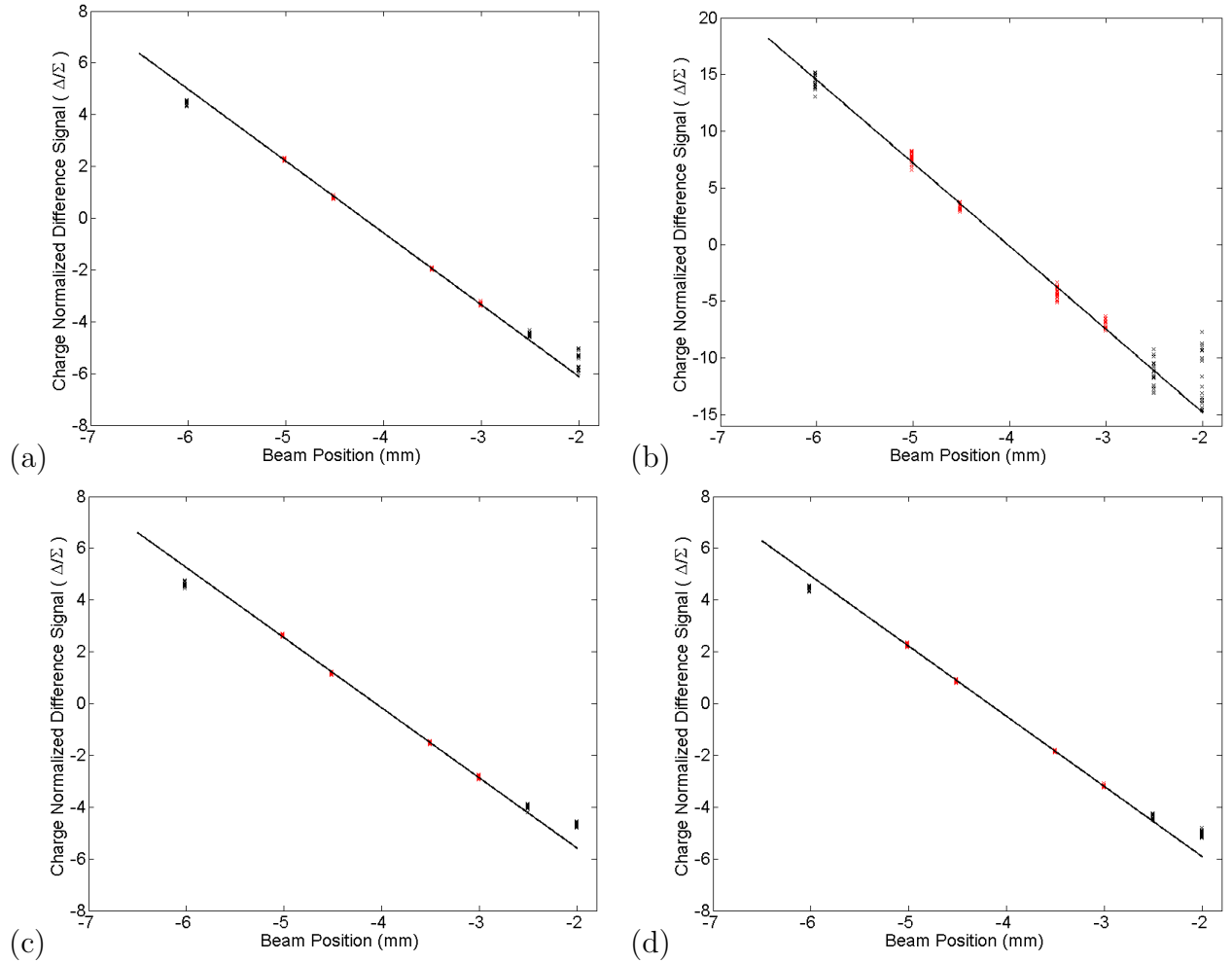


Figure 3.18: Difference-over-sum vs beam position, as calculated from corrector magnet current (equation 3.7), for each of the four BPM processors (all with signals input from ML12X), P1(a), P2(b), P3(c) and P4(d) respectively. The region shown in red is the range over which the line has been fitted (missing data points are as a result of corrupt data files).

identical cables, connectors and other components these too may have an impact on the calibration constant. Processor P2 has a vastly different calibration constant (and therefore sum and difference signals, table 3.3) and of measured beam position for an unperturbed beam (figure 3.19) suggesting processor malfunction or possibly a loose cable connection. For this reason  $P_2$  will be excluded from the following resolution calculations.

## Results

The resolution of a BPM is determined by the amount of random noise present. The resolution of a BPM should be the rms of the distribution of position measurements for some

I (A)	BPM															
	P1			P2			P3			P4						
	$\Sigma(\text{mV})$	$\delta\Sigma^*$	$\bar{y}$	$\delta y^*$	$\Sigma(\text{mV})$	$\delta\Sigma^*$	$\bar{y}$	$\delta y^*$	$\Sigma(\text{mV})$	$\delta\Sigma^*$	$\bar{y}$	$\delta y^*$	$\Sigma(\text{mV})$	$\delta\Sigma^*$	$\bar{y}$	$\delta y^*$
-2.4	22.5	7	4.45	3	11.1	8.5	14.29	8	22.3	7.5	4.62	3.5	22.6	7	4.28	5
-2	21.6	7	2.27	3.5	11	9	7.63	11	21.4	6.5	2.62	3	21.8	6	2.27	4.5
-1.8	20.2	8.5	0.8	10.5	10.8	6.5	3.26	14	20	8.5	1.17	6	20.3	7.5	0.87	10
-1.4	21.3	14.5	-1.94	2.5	11.2	8	-4.22	19	21.1	14	-1.51	4.5	21.3	13.5	-1.83	3.5
-1.2	19.4	7	-3.32	3	11	7	-7.01	9	19.3	7	-2.84	3.5	19.6	6.5	-3.18	2.5
-1	21.5	13	-4.48	3	10.7	9	-11.35	18	21.2	15	-4	4.5	21.4	15.5	-4.36	3
-0.8	18	7	-5.53	8.5	11.1	8	-11.59	30	22.8	7	-4.66	3	23.1	6	-5.01	4

Table 3.3: Mean and variation (\*as percentage of mean) of beam charge ( $\bar{\Sigma}$ ,  $\delta\Sigma$ ) and vertical position ( $\bar{y}$ ,  $\delta y$ ) as measured by the four processors, connected in parallel to ML12X, during a calibration procedure (figure 3.18), where  $y = \Delta/\Sigma$ .

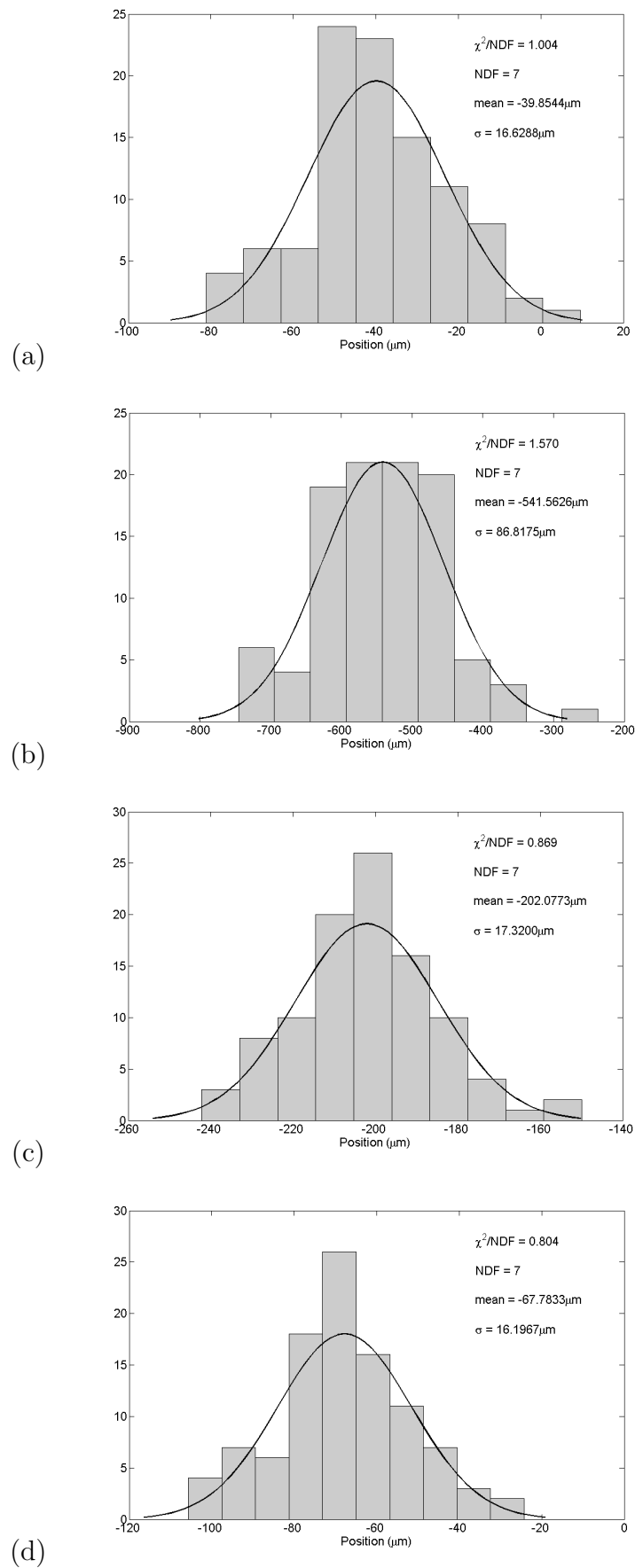


Figure 3.19: Distribution of measured position for 100 pulses in (a) P1 (b) P2, (c) P3 and (d) P4. P2 shows a much wider distribution, inconsistent with the other three, and so will be omitted from the resolution calculations.

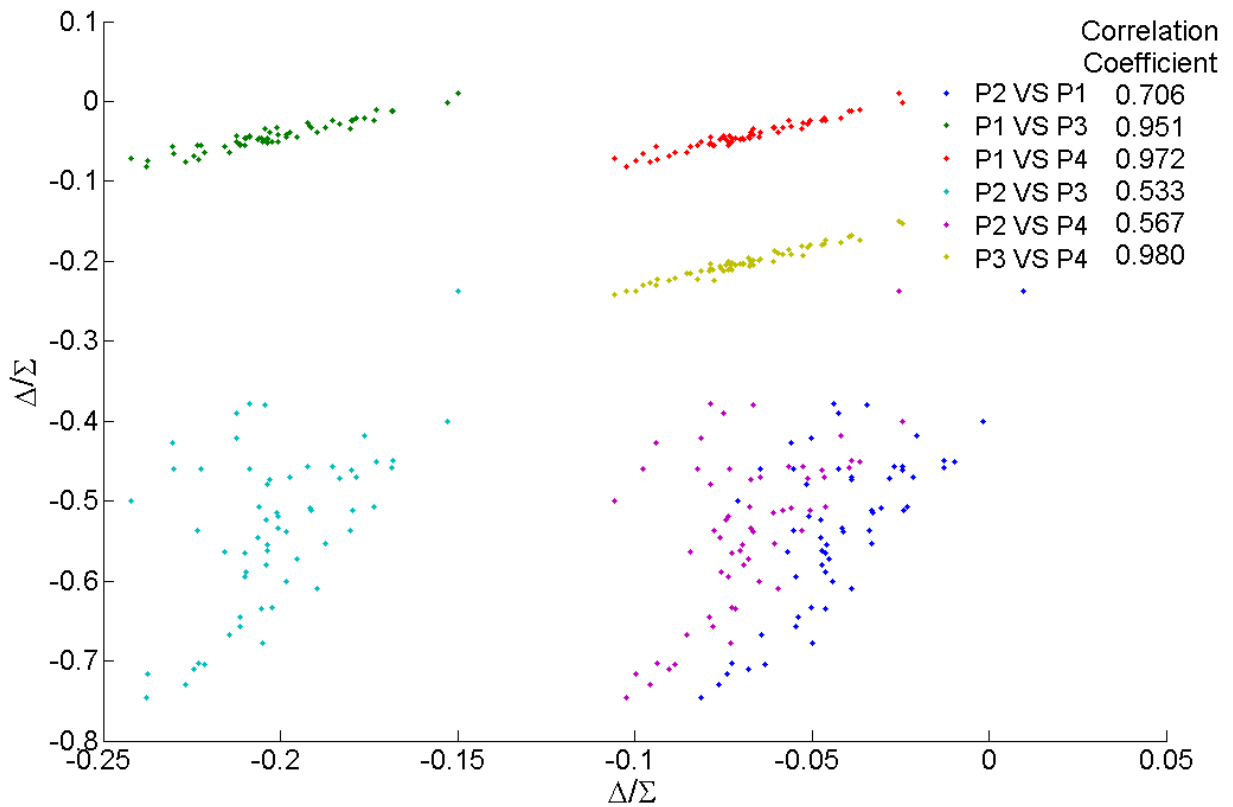


Figure 3.20: Correlation plots of beam positions as measured by each processor versus positions as measured by the other three.

number of pulses of a beam with fixed position. Experimentally, this is not the case since there are bunch to bunch variations in the properties of the beam (position, size etc.). A better estimate of the noise (resolution) in a BPM processor can be achieved in case of identical signals being input to multiple processors. This may be done by the consideration of the beam position as measured in one processor in relation to that measured by the second. Variation in the beam will see the signal vary in the same way in both processors, removal of this correlation will leave only the processor noise. The resolution may be determined by use of the correlation coefficient between the two sets of data. Considering, in the first instance, processors  $P_1$  and  $P_3$

$$\rho_{p_1,p_3} = \frac{cov(p_1, p_3)}{\sigma_{p_1}\sigma_{p_3}} = \frac{\langle(p_1 - \mu_{p_1})(p_3 - \mu_{p_3})\rangle}{\sigma_{p_1}\sigma_{p_3}} \quad (3.21)$$

Where  $\rho_{p_1,p_3}$  is the correlation coefficient and  $\mu_{p_1}, \mu_{p_3}$  are the expected values of  $p_1$  (the beam position as measured in processor,  $P_1$ ) and  $p_3$  (the beam position as measured in processor  $P_3$ ). It is also true that  $\mu_{p_1} = \langle(P_1)\rangle$  and  $\sigma_{p_1}^2 = \langle(p_1 - \langle p_1 \rangle)\rangle^2$  defining the correlation coefficient to be [86]

$$\rho_{p_1,p_3} = \frac{\langle p_1 p_3 \rangle - \langle p_1 \rangle \langle p_3 \rangle}{\sqrt{\langle p_1^2 \rangle - \langle p_1 \rangle^2} \sqrt{\langle p_3^2 \rangle - \langle p_3 \rangle^2}} \quad (3.22)$$

Figure 3.20 shows correlation plots of the beam position as measured by the four processors with correlation coefficients also shown. From these results the resolution,  $R$ , may be calculated as follows

$$R_{p_1,p_3} = \sigma_{p_1} \sqrt{(1 - \rho_{p_1,p_3})} \quad (3.23)$$

If the assumption that all three BPM processors are identical were correct then the resolution calculation would yield the same result in all three of the above cases. Since this is not the case it can be inferred that each individual processor's resolution must be different than that of the other two. Where data from three BPM processors with identical inputs exists it is possible to determine these individual resolutions.

$$\mathfrak{R}_{P_1} = \frac{\sqrt{R_{p_1,p_3}^2 + R_{p_1,p_4}^2 - R_{p_3,p_4}^2}}{\sqrt{2}} \quad (3.24)$$

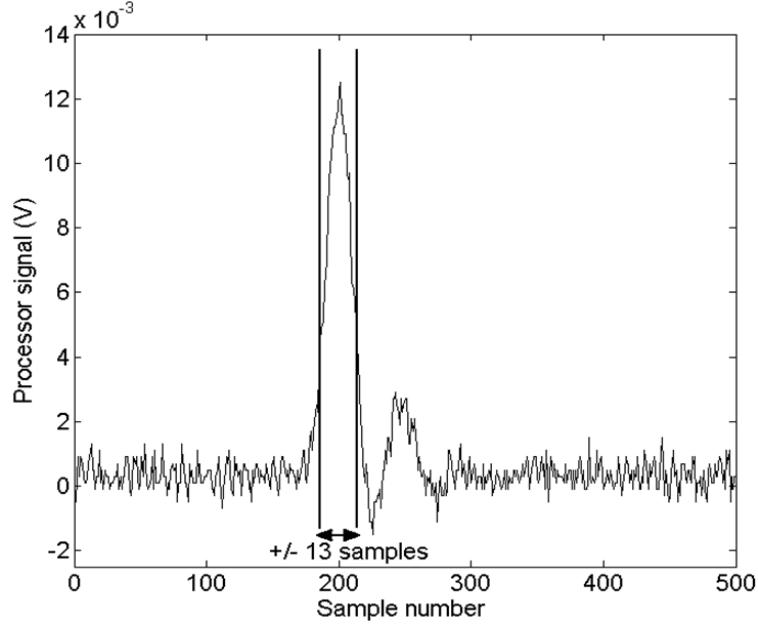


Figure 3.21: Example of method of selection of data window considered for analysis.

$$\mathfrak{R}_{P3} = \frac{\sqrt{R_{p1,p3}^2 + R_{p3,p4}^2 - R_{p1,p4}^2}}{\sqrt{2}} \quad (3.25)$$

$$\mathfrak{R}_{P4} = \frac{\sqrt{R_{p1,p4}^2 + R_{p3,p4}^2 - R_{p1,p3}^2}}{\sqrt{2}} \quad (3.26)$$

where  $\mathfrak{R}$  is the individual resolution of each BPM processor and  $R$  gives an upper limit of resolution which is dependent on a pair of processors.

The resolutions of the FONT analogue BPM processors are  $4.3 \pm 0.05 \mu\text{m}$ ,  $4.0 \pm 0.02 \mu\text{m}$  and  $1.0 \pm 0.02 \mu\text{m}$  for P1, P3 and P4 respectively where the error arises from the error on the rms position. These resolution values are the processor contribution to the overall BPM system resolution only, there will also be contributions from the BPM and other components such as data acquisition hardware though it is expected that the processors will have the most significant effect on resolution [87]. This multiple processor method illustrates that the resolution of the BPM system is significantly worse than the expected  $1\text{-}2\mu\text{m}$  [88], although the case of processor P4 shows that resolution close to  $1 \mu\text{m}$  is possible.

## 3.5 Resolution Dependences

The resolution of a BPM system may be dependent not only on the quality of the hardware but also on the input signal tolerance, data acquisition and analysis.

### Integration Window

The BPM data are taken using an oscilloscope producing signals such as that shown in figure 3.21. As was mentioned previously the beam position is determined by division of the difference by the sum signal,  $\Delta/\Sigma$  (equations 3.11, 3.10 and 2.13). The question is whether to consider the whole of these two signals or just the peaks. It is not practical to use just the peak value due to the oscilloscope noise and sample timing jitter producing uncertainty in the position in time of the peak output from the processor. So what proportion of the waveform should be used?

The proportion of the sum and difference signals used is referred to as the integration window, the width of which is described as the number of time samples either side of the peak (for example see figure 3.21. In the first instance it seems reasonable to choose an integration window to be some number of samples either side of the peak value but not so wide as to include anything outside of the main peak. This is in fact not the case since although  $Q$  should be equal to zero where  $I$  is maximum (equation 3.1) some part of the quadrature component may be hidden inside the main peak in the case where the LO is not exactly in phase with the stripline signal during mixing in the BPM processor (section 3.2.2). The calibration constant varies significantly with integration window but seems to level off when the whole of the waveform has been taken into consideration (figure 3.22a), the only issue being that as more of the signal is taken into account more noise is also included. This may be compensated for, to some extent, through the method of noise removal outlined in the calibration section 3.2.2.

Figure 3.22b shows the variation of resolution with integration window as calculated using the fixed calibration constants (determined using the entire waveforms) shown in sec-

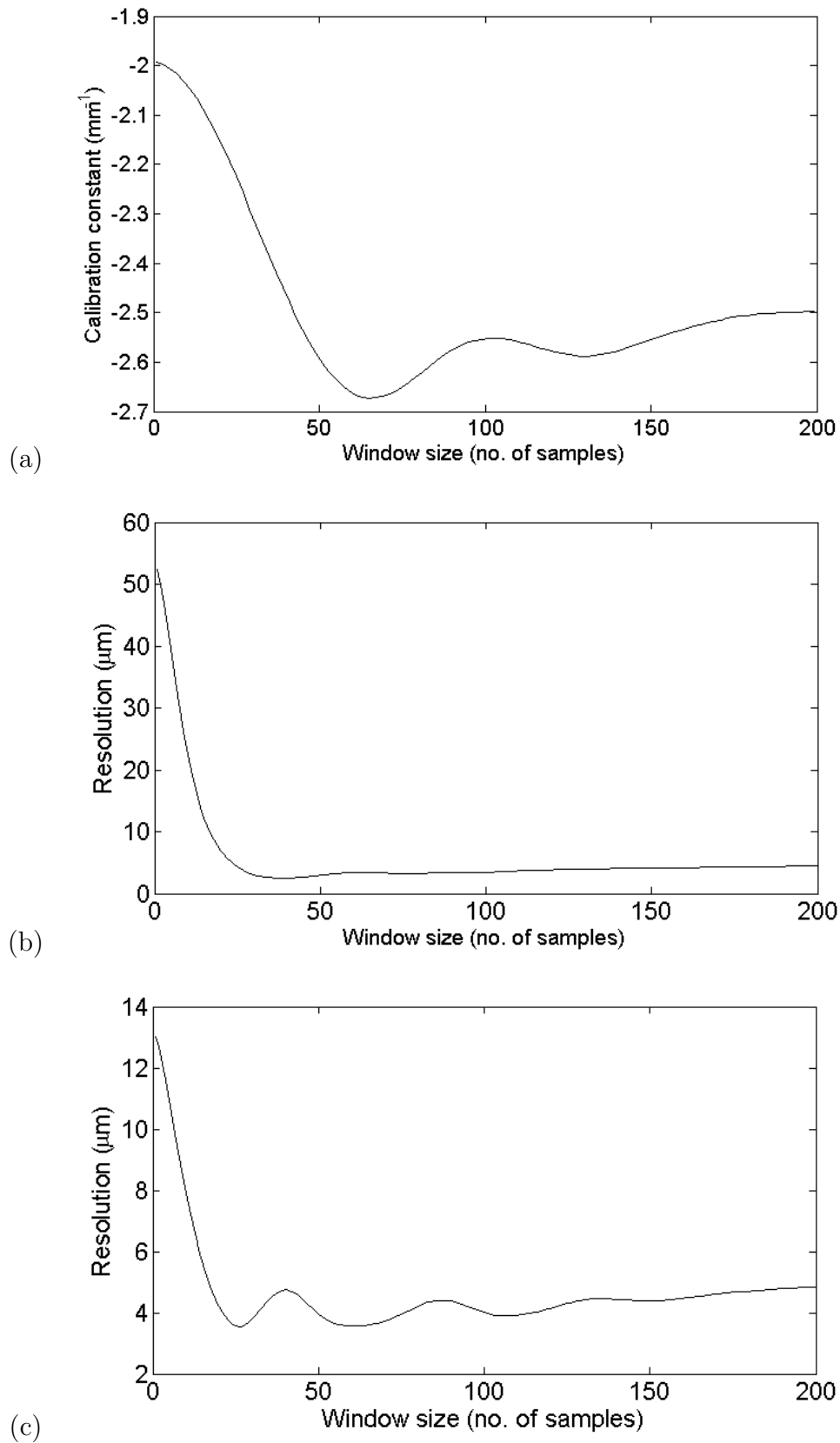


Figure 3.22: Variation of BPM calibration constant (a) and resolution (b) and (c) with width of integration window ( $sample = 200$  ps). (b) shows the variation in resolution when the integration window for the resolution data is varied and the calibration constant used to calculate position fixed. (c) shows the variation in resolution when the width of the integration window is varied for both the calibration and resolution data; at each point on this plot a different calibration constant (those in figure (a)) is used.

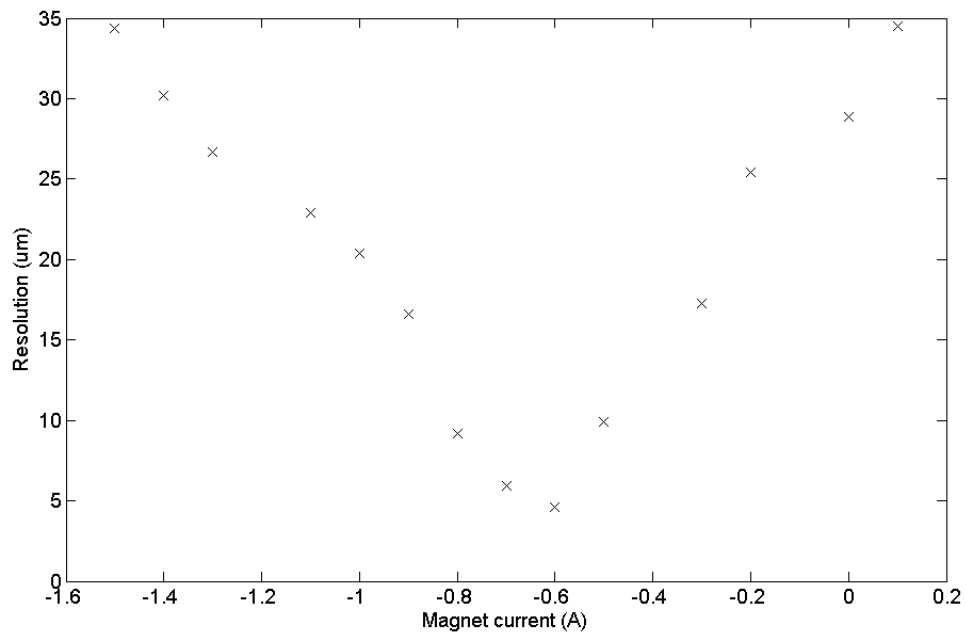


Figure 3.23: BPM resolution vs Beam position (where the data was processed over the full integration window).

tion 3.3.1. Figure 3.22c also shows the variation of resolution with integration window but calculated using calibration constants which also vary with integration window (those in figure 3.22a). It can be seen that a realistic resolution estimate may not be determined by consideration only of the peaks of the processor output signals and that as the window size is increased beyond that which is just wide enough to include the main pulse the resolution worsens (most likely due to the decreasing signal-to-noise ratio). The most favourable resolution result is  $2.5 \mu\text{m}$  (figure 3.22b) but, for consistency, all calibration and resolution calculations outlined earlier in the chapter were performed using integration over the whole waveform to determine the values for sum and difference (see equations 3.10 and 3.11).

### Beam Position

It has been seen that the processor output is affected by the magnitude of the input signals (section 3.3). This can be seen by observation of the variation of the calculated resolution with respect to beam position (figure 3.23). The best resolution is where the beam is closest to the electrical centre of the BPM; it worsens as the beam moves outwards from this point;

here the resolution was calculated using the three BPM method.

### 3.5.1 Possible Causes of Low BPM Resolution

Low BPM resolution may arise from:

- System properties
  - BPM processing electronics
  - BPM striplines
  - Ancillary components (cables, connectors, attenuators, amplifiers etc). FONT was not a permanent installation at ATF meaning that equipment was frequently dismantled and removed from the beamline, increasing the likelihood of possible problems with ancillary components.
  - Data acquisition techniques (for example, resolution of oscilloscopes).
  - LO being miss-phased with incoming BPM signal to mixing electronics (phasing done by hand using electronic phase shifters with variable power supplies).
- Measurement methods
  - Use of ballistic beam (where focusing magnets between corrector and BPM are switched off). It is often impractical to have a completely ballistic beam due to the potential for beam loss. Dipole corrector magnets may be used without complicating optics calculations which may cause a change in the state of the beam between the corrector (being used for calibration purposes) and the BPM and between each of the BPMs. For example  $x$ - $y$  coupling may be introduced meaning that movement of the beam in  $y$  will also cause movement of the beam in  $x$  leading to an incorrect prediction of beam position using the corrector magnet current.
- Calculation methods

- Assumption that BPMs and processors are identical.

It is clear that the BPMs are not identical and so methods of determining resolution, other than those described earlier, are desirable (some alternative methods will be discussed, with reference to cavity BPMs, in chapter 6) including the consideration of both the  $x$  and  $y$  directions in order to make it possible to take account of any effect one may have on the other. Many of these problems are currently being addressed at ATF2.

### 3.5.2 The Effect of BPM Resolution on Overall Feedback System Performance

There are several noise contributions to the overall feedback system. The most significant components being the feedback board (ADCs and DACs), the kicker amplifier and the BPM.

- The kicker amplifier - contributes noise of approximately  $10\mu\text{V}$  which is negligible when compared to the output from the digital feedback board which is of the order of hundreds of millivolts [76].
- The DAC - contributes noise of  $< 0.2$  LSB (least significant bit) [76] which is under the quantization noise<sup>2</sup> and so not significant.
- The ADC - has a noise figure of  $\pm 1$  LSB (according to the manufacturer).
- The BPM - has a noise figure in Volts of  $\approx 25\mu\text{V}$  for a resolution of  $5\mu\text{m}$ .

The overall noise of the feedback board (since the ADC is not perfect) is  $\approx 1.5$  LSB rms [76]. So an input of  $\approx 100$  mV to the digital board this gives a noise level in Volts to be  $46\mu\text{V}$ , adding in quadrature gives a total noise of  $\approx 52.4\mu\text{V}$ . The BPM resolution has a significant effect on the noise of the feedback system making it essential to improve the BPMs measured here (the required value for operation at the ILC has been estimated to be  $\approx 1\mu\text{m}$ ). For

---

<sup>2</sup>Quantization noise is a rounding error arising from the difference between the analogue signal to be measured and the digital output of the ADC. It is distributed uniformly over  $\pm 0.5$  LSB



Figure 3.24: Diagram of layout of FONT5 at ATF2. ZV6X is a corrector magnet and QD10X, QD12X and QD14X are quadrupole magnets. P1, P2 and P3 are BPMs and K1 and K2 are kickers (one each for correction in  $y$  and  $y'$ ).

the ATF feedback layout, a feedback BPM (ML10X) resolution of  $4 \mu\text{m}$  will yield an error of  $\approx 75 \text{ nm}$  on a position correction centred on ML11X (which is 3 m downstream of the kicker).

## 3.6 FONT System Upgrade for ATF2

The ATF upgrade gives the ideal opportunity for the FONT system to progress from a strictly research project to a working system for use in the day to day running of ATF2. Three dedicated stripline BPMs and two stripline kicker magnets have been installed in the extraction line of the ATF2 machine; figure 3.24 shows a diagram of the new hardware setup for the FONT5 system and figure A.1 (appendix A) shows a detailed cable plant schematic. It is the aim of the FONT project, regarding ATF2, to provide bunch by bunch correction in both  $y$  and  $y'$  to a resolution at or better than one micron. In order to achieve this it is necessary to improve the resolution of the BPMs and to update the feedback hardware to accommodate the use of both kicker magnets. Improvement of the BPM resolution is currently on going with approach from several directions. One major change will be with the data acquisition system. Until recently data from the BPMs were recorded using an oscilloscope, which will be upgraded to higher resolution digital ADCs. The actual BPM hardware will, in the first instance, retain the current processing scheme but with better optimization of mixers and filters. There will follow another iteration of beam position monitor electronics involving a new scheme which is independent of any local oscillator (LO), thereby eliminating problems caused by badly phased or unstable LO signals.

## 3.7 Summary

The FONT feedback system is a fast intra train feedback system designed to provide beam position control at the interaction point of future linear colliders. Passing through multiple stages FONT has progressed to FONT5, an ILC prototype currently being tested at ATF2.

One of the major components of this feedback system is a stripline beam position monitor requiring micron level resolution in order to perform adequately at the ILC. Investigation into the properties of the BPMs and calculation of their resolution found that the BPM processing electronics were not identical and that their resolution, in some cases, was much too low. The resolution of processors P1, P3 and P4 (P2 was not reliable) were calculated to be  $4.3 \pm 0.05 \mu\text{m}$ ,  $4.0 \pm 0.02 \mu\text{m}$  and  $1.0 \pm 0.02 \mu\text{m}$  respectively, showing that with this processing scheme it is possible for the resolution to approach  $1 \mu\text{m}$ .

# Chapter 4

## Cavity Beam Position Monitors

The most recently developed area in beam position monitor engineering is that of cavity BPMs. Cavity BPMs will allow achievement of extremely high resolution beam position measurements ideal for low emittance, small spot size beams. This chapter will address the theory behind cavity BPMs and outline the method used to interpret the BPM output as a beam position signal.

### 4.1 Cavities as Beam Position Monitors

A cavity beam position monitor is essentially a form of waveguide and may be described as such. A charged particle present at the centre of a conducting pipe produces an electromagnetic (EM) field within the pipe which becomes distorted as the particle moves away from this central point [89]. It is the result of excitation of this field which is used for beam position measurement.

Consider, for simplicity, a cavity as a conducting cylindrical waveguide sealed at either end. For an electron travelling in a longitudinal direction through the cavity its electromagnetic field propagates as a collection of waves. These may be described as follows [90] (in cylindrical coordinates), with  $H_z = 0$  since we are interested in the transverse magnetic field

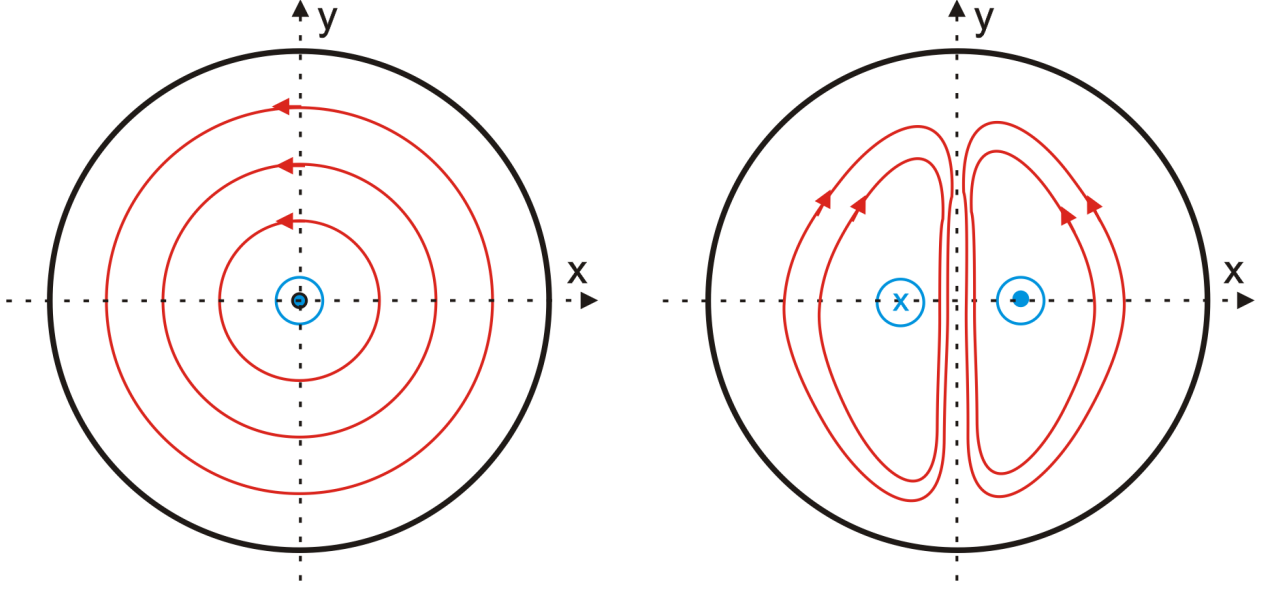


Figure 4.1: Configuration of the monopole (left) and dipole mode (right) fields in a cylindrical cavity with the electric field represented in blue and the magnetic in red. The magnitude of the dipole mode ( $TM_{110}$ ) is dependent on the position of the beam in the cavity whereas the monopole mode ( $TM_{010}$ ) is dependent on charge alone.

only for beam position measurement.

$$E_r = -C \frac{k_z}{k_c} J'_m(k_c r) \cos(m\phi) \sin\left(\frac{p\pi z}{l}\right) e^{i\omega t} \quad (4.1)$$

$$E_\phi = C \frac{k_z m}{k_c^2} \frac{J_m(k_c r)}{r} \sin(m\phi) \sin\left(\frac{p\pi z}{l}\right) e^{i\omega t} \quad (4.2)$$

$$E_z = C J_m(k_c r) \cos(m\phi) \cos\left(\frac{p\pi z}{l}\right) e^{i\omega t} \quad (4.3)$$

$$H_r = -iC \frac{\omega \epsilon_0 m}{k_c^2} \frac{J_m(k_c r)}{r} \sin(m\phi) \cos\left(\frac{p\pi z}{l}\right) e^{i\omega t} \quad (4.4)$$

$$H_\phi = -iC \frac{\omega \epsilon_0}{k_c} J'_m(k_c r) \cos(m\phi) \cos\left(\frac{p\pi z}{l}\right) e^{i\omega t} \quad (4.5)$$

Where  $C \propto A$  (the amplitude of oscillation),  $k_z = p\pi/l$  (where  $l$  is the length of the cavity),  $J_m$  is a Bessel function of the first kind (see Appendix B) [91] and  $m, p$  are integers  $m, p = 0, 1, 2, 3, \dots$  except  $m = p = 0$  which would give all fields equal to zero [92]. Equations 4.1 - 4.5 describe all possible transverse magnetic modes (determined by solving Maxwell's equations),  $TM_{mnp}$ , where the indices  $m, n$  and  $p$  represent  $\phi, r$  and  $z$  respectively. The primary or lowest frequency (monopole) transverse magnetic mode,  $TM_{010}$ , may be described

by the following equations.

$$E_z = C J_0 \left( \frac{j_{01} r}{R} \right) e^{i\omega_{010} t} \quad (4.6)$$

$$H_r = 0 \quad (4.7)$$

$$H_\phi = -iC \frac{\omega_{010} \epsilon_0 R}{j_{01}} J_0' \left( \frac{j_{01} r}{R} \right) e^{i\omega_{010} t} \quad (4.8)$$

Where the ends and sides of the cavity determine the boundary conditions where the transverse components of the EM waves must be equal to zero [93],  $E_z = 0$  at  $r = R$  and  $z = L$  (where  $R$  and  $L$  are the bore radius and length of the cavity respectively), which gives  $k_c = j_{mn}/R$  where  $j_{mn}$  is the  $n$ th root of the Bessel function.  $k_c$  is the wave number for the cut off frequency, which is the lowest frequency mode possible, dictated by these boundary conditions. Similarly the dipole mode (figure 4.1),  $TM_{110}$ , may be written as in equations 4.9 - 4.11. These so called modes are a way of referring to one specific field solution of the many which satisfy Maxwell's equations alongside any given wave equations and boundary conditions [94].

$$E_z = C J_1 \left( \frac{j_{11} r}{R} \right) e^{i\omega_{110} t} \quad (4.9)$$

$$H_r = -iC \frac{\omega_{110} \epsilon_0 R^2}{j_{11}^2 r} J_1 \left( \frac{j_{11} r}{R} \right) \sin(\phi) e^{i\omega_{110} t} \quad (4.10)$$

$$H_\phi = -iC \frac{\omega_{110} \epsilon_0 R}{j_{11}} J_1' \left( \frac{j_{11} r}{R} \right) \cos(\phi) e^{i\omega_{110} t} \quad (4.11)$$

The angular frequency may be defined using  $k^2 = k_c^2 + k_z^2$  to give the following equation.

$$\omega_{mnp} = \frac{1}{\sqrt{\mu_0 \epsilon_0}} \sqrt{\left( \frac{j_{mn}}{R} \right)^2 + \left( \frac{p\pi}{l} \right)^2} \quad (4.12)$$

### 4.1.1 Quality Factor

One of the most important parameters of the cavity is known as the quality factor. The quality factor may be seen to be a measure of the efficiency of a specific resonant mode of

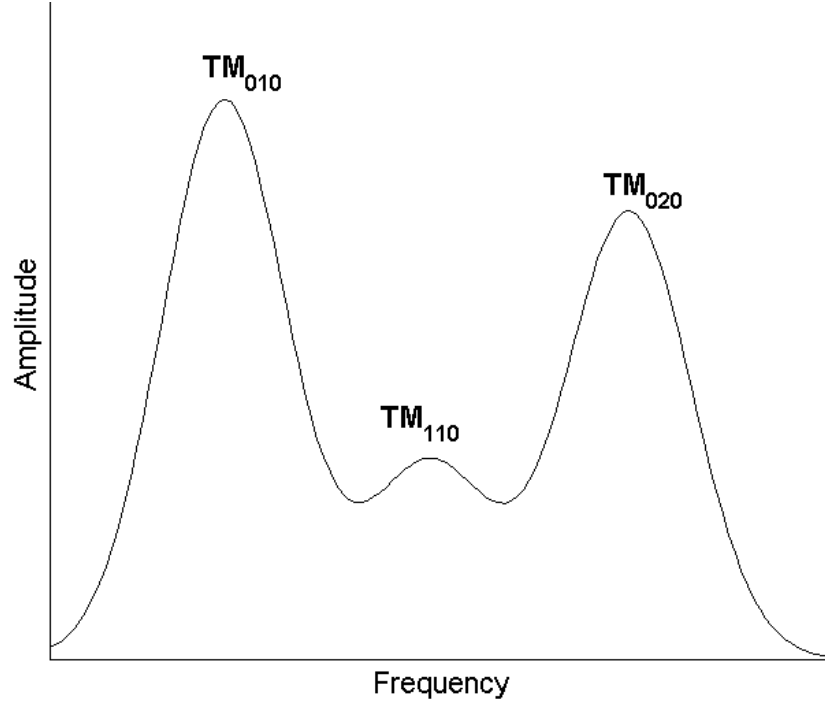


Figure 4.2: Plot to show variation of transverse magnetic field modes with frequency. It can be seen that, due to finite  $Q$  values, there is overlapping of the modes.

a cavity. It is the quality of the resonator and so a cavity with higher  $Q$  value stores more energy than it loses. It is defined as follows [95].

$$Q \equiv \omega \frac{U}{P_{loss}} \quad (4.13)$$

Where  $U$  is the energy stored in the cavity,  $\omega$  the angular frequency and  $P_{loss}$  is the power lost both inside the cavity and from external coupling to the cavity. Considering these two types of power loss separately allows for the expression of two types of quality factor.

$$Q_0 \equiv \omega \frac{U}{P_{wall}} \quad (4.14)$$

$$Q_{ext} \equiv \omega \frac{U}{P_{out}} \quad (4.15)$$

$Q_0$  is known as the unloaded quality factor and is due only to the cavity.  $P_{wall}$  is the power lost to the inside wall of the cavity, for example due to the resistivity of the cavity material, and is dependent on the cavity material and surface condition [96].  $Q_{ext}$  is the external quality factor and is a measure of the power output from external coupling to the cavity.

This is dependent only on the geometry of the cavity. These  $Q$  values may be related as follows

$$\frac{1}{Q_L} = \frac{1}{Q_0} + \frac{1}{Q_{ext}} \quad (4.16)$$

Where  $Q_L$  is known as the loaded quality factor and considers both internal and external power loss. The ratio of the loaded and external quality factors is known as the coupling constant [97].

$$\beta = \frac{Q_0}{Q_{ext}} = \frac{P_{out}}{P_{loss}} \quad (4.17)$$

This coupling constant is a measure of the coupling strength between the cavity and the outside world. For example when coupling is perfect there are no reflections and  $\beta = 1$ ,  $Q_0 = Q_{ext}$ .

### Energy Stored in a Cavity

A favourable value of  $\beta$  arises from low power loss to the cavity wall (small  $P_{wall}$ ) and high power output ( $P_{out}$ ), by definition

$$P = -\frac{dU}{dt} \quad (4.18)$$

Considering equation 4.13 we get an expression for the energy stored in the cavity.

$$U = U_0 e^{-\frac{\omega}{Q_L} t} \quad (4.19)$$

Where  $U_0$  is the initial energy stored in the cavity and the decay time constant is defined as follows.

$$\tau = \frac{Q_L}{\omega} \quad (4.20)$$

This is the time taken for the energy in the cavity to be reduced to  $1/e$  of its original value.

### Cavity-Beam Coupling

Given that the unloaded quality factor,  $Q_0$ , is dependent on the material (and surface quality) of which the cavity is made it is preferable to use instead the external quality factor or some other measure of cavity efficiency not dependent on these variables. The  $R/Q$  parameter serves this purpose and characterizes the way in which the beam interacts with the cavity. Here  $Q$  is again the quality factor and  $R$  is known as the shunt impedance.

$$R = \frac{|\int E_z \cdot dz|^2}{P_{wall}} = \frac{|V|^2}{P} \quad (4.21)$$

Where  $E_z$  is the electric field along the beam axis and  $V$  is the voltage induced in the cavity. So for  $R/Q$  we get a value to assess the accelerating field which is dependent only on the cavity geometry.

$$\frac{R}{Q} = \frac{|V|^2}{\omega U} \quad (4.22)$$

#### 4.1.2 Output Signals

Of the many available transverse magnetic modes the first monopole and dipole modes are considered, that is  $TM_{010}$  and  $TM_{110}$  (figure 4.1), where the offset and tilt of the beam are calculated as follows

$$V_{offset}(t) = \Delta y \times q e^{i\omega t} e^{-t/\tau} \quad (4.23)$$

$$V_{tilt}(t) = \Delta \alpha \times q e^{i\omega t + \pi/2} e^{-t/\tau} \quad (4.24)$$

where  $V$  is voltage,  $\Delta y$  is the beam offset,  $\Delta \alpha$  is the bunch tilt (the angle between the bunch and the longitudinal axis, according to the cavity) and  $q$  is the beam charge. The factor of  $\frac{\pi}{2}$  may be understood by considering the bunch as two different macro particles (one representing the head of the bunch and one the tail). The voltage outputs for each of

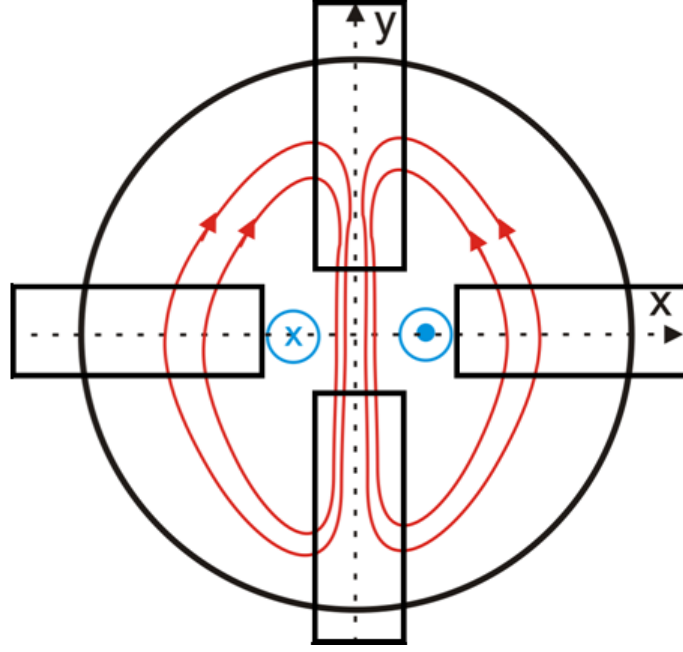


Figure 4.3: The arrangement of waveguides used to couple to cavity dipole modes. The waveguides couple to transverse magnetic modes whose field lines are parallel to the orientation of the waveguide. The red lines represent the magnetic field lines and blue the electric.

these macro particles are as follows

$$V_+(t) = -\frac{q}{2}\theta\sigma_z \frac{d^2V}{dqdy} \sin\left(\omega\left(t + \frac{\sigma_z}{c}\right)\right) \quad (4.25)$$

$$V_-(t) = -\frac{q}{2}\theta\sigma_z \frac{d^2V}{dqdy} \sin\left(\omega\left(t - \frac{\sigma_z}{c}\right)\right) \quad (4.26)$$

giving a phase difference of  $\frac{\pi}{2}$  where the macro particles are located at  $\pm\sigma_z$ ,  $q$  is the bunch charge and  $\theta$  is the tilt angle.

### Transverse Magnetic Dipole Mode

The first transverse magnetic dipole mode ( $TM_{110}$ ) is used for the measurement of position since the magnitude of this mode is directly dependent upon the transverse position of the beam in the cavity and is at a minimum when the beam is positioned at the centre of the cavity. This mode is also dependent on the charge of the beam and so a beam position measurement derived from this mode must be normalized by beam charge.

### Transverse Magnetic Monopole Mode

The monopole mode ( $TM_{110}$ ) is independent of beam position (neglecting higher order terms) and is therefore a constant for identical electron bunches passing through the cavity regardless of their trajectory. The monopole mode gives a measure of the charge and arrival phase of the electron bunch and allows for charge normalization of the dipole signal thus giving a position dependent result.

#### 4.1.3 Mode Selection

Figure 4.2 shows the frequency distribution of transverse magnetic modes in an individual cavity. It can be seen that at the peak of the dipole mode ( $TM_{110}$ ) there is also some added monopole signal (due to each mode having a finite value of  $Q$  [98]) from both the first and second transverse magnetic monopole modes, this prevents the dipole mode from being selected using electronic frequency filtering techniques. The dipole mode information is extracted using selective coupling by waveguides. The slots couple out the dipole mode where the magnetic field vector is parallel to the slot, whilst rejecting the monopole mode which is perpendicular to the slot. Figure 4.3 shows the arrangement of slots in the cavity and the mechanism by which the  $x$ -axis dipole mode is selected. The top and bottom slots are used to couple out the  $x$  dipole mode (as shown in figure 4.3) and the  $y$  dipole mode is selected using the horizontal slots.

## 4.2 Signal Processing

Since the BPM output (equation 4.23) is in the GHz range it must be down-converted to a lower, more easily manageable, frequency due to the lack of available data acquisition systems able to cope with such high frequencies. The signal is processed in two stages first through electronics and then using software.

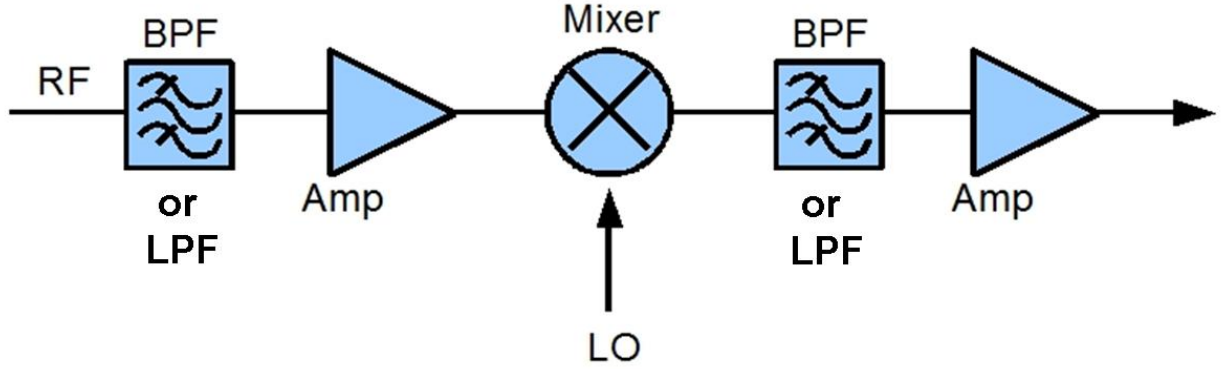


Figure 4.4: Schematic of the method by which BPM signals are processed using electronics. This is known as a homodyne receiver when the frequency of the LO is the same as that of the incoming signal ( $f_{RF} = f_{LO}$ ) and a heterodyne receiver for  $f_{RF} \neq f_{LO}$ .

### 4.2.1 Electronics

Figure 4.4 shows a diagram of the major components used in BPM processing electronics. This scheme may be implemented in 2 ways; as a heterodyne receiver under the condition where the incoming RF signal is of different frequency to that of the LO ( $f_{RF} \neq f_{LO}$ ) and a homodyne receiver where  $f_{RF} = f_{LO}$ .

The heterodyne receiver converts an incoming signal to a fixed intermediate frequency (IF) through the use of frequency filtering and mixing [99] (figure 4.4). The incoming RF signal is filtered amplified and mixed to give an intermediate frequency where the intermediate frequency is given by

$$\omega_{IF} = \omega_{RF} - \omega_{LO} \quad (4.27)$$

The advantage of this method is that the IF may be of low frequency and therefore more suited to data acquisition and situations where signals must travel along long cables. Consider incoming and LO signals which may be characterized as follows

$$V_{RF}(t) = a \cos(\omega_{RF}t) \quad (4.28)$$

$$V_{LO}(t) = b \cos(\omega_{LO}t) \quad (4.29)$$

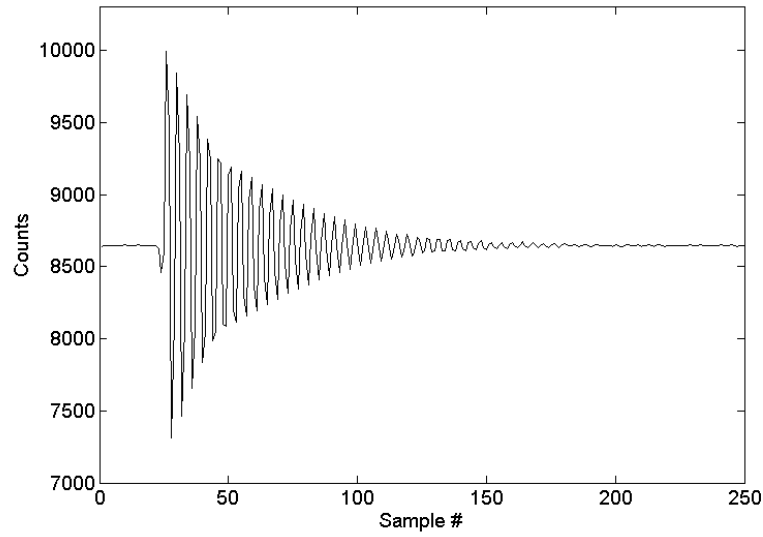


Figure 4.5: Dipole cavity BPM output waveform. The waveform is an exponentially decaying sine wave (equation 4.31), where the digitiser is clocked at 100 MHz so that each sample is 10ns.

These two signals are combined in the mixer as follows [100]

$$V_{RF}(t)V_{LO}(t) = \frac{ab}{2}[\cos(\omega_{RF} - \omega_{LO}) + \cos(\omega_{RF} + \omega_{LO})] \quad (4.30)$$

giving two signals of different frequency. The first term gives what is known as the down-converted component of the waveform and the second gives the higher frequency, up-converted component. In the BPM case the interest is in the down-converted term with  $\omega_{LO} > \omega_{IF}$ . The up-converted term is filtered out. In the case of the ATF2 cavity BPM system (discussed further in section 5.1.3) the frequency is processed using a homodyne receiver followed by a heterodyne receiver to ultimately down-convert the signal from 6.426GHz to 20MHz.

### 4.2.2 Digital Down Conversion

Figure 4.5 shows an example of the digitized output of the mixing electronics. This signal is of the form [101]

$$V(t) = Ae^{-\Gamma t} \sin(\omega t + \phi) \quad (4.31)$$

Where  $V(t)$  is the electronics output voltage,  $A$  is the amplitude,  $\phi$  the phase and  $\Gamma$  the decay constant of the waveform (where  $\Gamma = 1/\tau$ ).

The method by which the waveform is processed is known as digital down conversion (DDC) [102]. First the signal is mixed with a local oscillator of the form shown in equation 4.32 to give a complex waveform.

$$V_{LO}(t) = e^{i\omega t} \quad (4.32)$$

Where  $\omega = 2\pi f_0$  and  $f_0$  is the frequency of the waveform.

The mixed signal is then filtered, using the MATLAB filter function (see Appendix B), in order to remove the up-converted component (with a frequency double that of the original waveform) introduced by the mixing process [103]. A time domain Gaussian filter described by equation 4.33 is used.

$$F = \sqrt{2\pi}\Delta f e^{\left(\frac{-t_i^2(2\pi\Delta f)^2}{2}\right)} \quad (4.33)$$

Where  $\Delta f$  is the filter bandwidth. Application of this filter produces the envelope of the mixed waveform from which amplitude and phase may be calculated as follows and can be seen in figure 4.6.

$$A = \sqrt{a^2 + b^2} \quad (4.34)$$

$$\phi = \tan^{-1}\left(\frac{b}{a}\right) \quad (4.35)$$

where the complex waveform  $V = a + ib$ . The amplitude and phase of this filtered waveform may then be used to calculate the in-phase ( $I$ ) and quadrature-phase ( $Q$ ) components of the amplitude, which can then be related to beam position.

Table 4.1 shows  $A_d$ ,  $\phi_d$ ,  $\omega$  and  $\tau$  calculated for one electron bunch passing through a dipole cavity BPM (see figure 4.5 for BPM output waveform from this bunch crossing) in the final focus beamline of ATF2 (the ATF2 cavity BPM installation will be discussed in chapter 5). Each variable was calculated at  $t = 62$  ADC samples (discussion of data taking

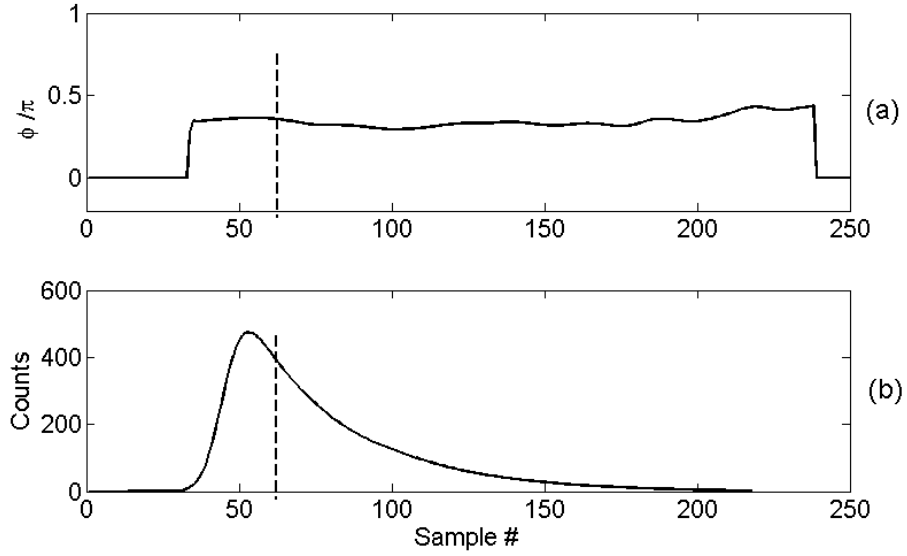


Figure 4.6: (a) phase,  $\phi$ , and (b) amplitude,  $A$  (equation 4.35) of the dipole cavity BPM waveform shown in figure 4.5. The dashed lines mark the sample number (10ns per sample) at which  $A$  and  $\phi$  were considered for the  $I$  and  $Q$  calculations (see equation 4.37).

methods, ADC counts and sample times will be discussed in chapter 5) as can be seen in figure 4.6.

### 4.2.3 Calculation of In Phase and Quadrature Phase Components

The  $I$  and  $Q$  components may be calculated using the following equations.

$$I = \frac{A_d}{A_r} \cos(\phi_d - \phi_r) \quad (4.36)$$

$$Q = \frac{A_d}{A_r} \sin(\phi_d - \phi_r) \quad (4.37)$$

where  $d$  and  $r$  represent the dipole and reference (or monopole) cavities. Both  $I$  and  $Q$  are dependent on beam position and so a rotation is applied as follows

$$\begin{pmatrix} I' \\ Q' \end{pmatrix} = \begin{pmatrix} \cos \theta_{iq} & \sin \theta_{iq} \\ -\sin \theta_{iq} & \cos \theta_{iq} \end{pmatrix} \begin{pmatrix} I \\ Q \end{pmatrix} \quad (4.38)$$

BPM	$A_d(counts)$	$\phi_d(rad)$	$\omega(rad)$	$\tau(samples)$	Sample #	$I$	$Q$
QF9AFF	392	$0.42\pi$	1.577	23	62	0.267	-0.129

Table 4.1: Cavity BPM output waveform parameters.

where  $\theta_{iq} = \tan^{-1}(m_{iq})$  and  $m_{iq}$  is the gradient of the  $I$  vs  $Q$  linear fit (see figure 5.19 in the next chapter), giving

$$I' = I \cos \theta_{iq} + Q \sin \theta_{iq} \quad (4.39)$$

$$Q' = -I \sin \theta_{iq} + Q \cos \theta_{iq} \quad (4.40)$$

This rotation makes  $Q'$  independent of beam position leaving  $I'$  with a linear dependence so now only  $I'$  need be considered for determining beam position.  $Q'$  is now dependent on the beam tilt ( $\theta$ ) alone.

## 4.3 Summary

Particular transverse magnetic modes present in a cavity with an electric charge passing through it are dependent on the proximity of the charge to the cavity wall. This phenomenon makes cavities suitable to act as beam position monitors.

The first transverse magnetic dipole mode ( $TM_{110}$ ) is coupled out using slots inserted into the cavity and is the mode selected for beam position measurements. This mode varies not only with beam position but also with beam charge and so a monopole or reference cavity is used to normalize the dipole output with respect to beam charge by coupling to the first monopole mode ( $TM_{010}$ ) which varies only with charge and not position. After charge normalization the resulting signal is dependent on beam position only. This signal has two components, in phase ( $I$ ) and quadrature phase ( $Q$ ), both of which vary with position. Application of a simple rotation gives the variables  $Q'$ , which is constant, and  $I'$  which is linearly dependent on the proximity of the beam to the cavity wall (transverse beam position), with a signal output of zero for the case where the beam is centred in the BPM.

# Chapter 5

## Cavity BPM Commissioning at ATF2

A system of cavity beam position monitors has been developed for use at ATF2 in the development of final focus systems with a view to their implementation in future linear colliders [41]. There follows an account of the commissioning of this system for normal ATF2 operation.

### 5.1 Cavity BPM Hardware Setup at ATF2

The cavity beam position monitor system at ATF2 consists of 32 C-band (where C-band refers to the operating frequency of the BPMs, the C-band region of RF frequencies is commonly described, using the IEEE standard, to be between 4 and 8 GHz where the BPMs in this system operate at 6.426 GHz) dipole cavities and 4 reference (monopole) cavities distributed throughout the extraction and final focus beamlines (figure 5.1). The system is made up of several major components; cavities, mixing electronics, digitization and timing system, data acquisition and analysis software and mover systems. Figure 5.2 shows a photograph of three cavity BPMs installed on the final focus beamline at ATF2.

#### 5.1.1 Cavities

There are two types of cavity BPM used, known as dipole and monopole cavities. The dipole cavities are coupled to the dipole transverse magnetic mode and the monopole, or reference cavities, are coupled to the monopole mode (see chapter 4 for an explanation of

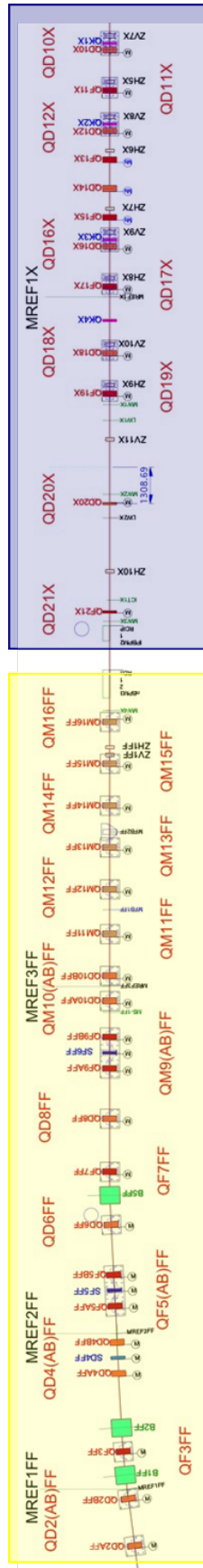


Figure 5.1: Layout of the C-band cavity BPM installation, with the beam travelling from top to bottom. Each BPM is labelled according to its neighbouring magnet [36] and the non-mover cavities are highlighted in blue whilst those mounted on movers are highlighted in yellow.

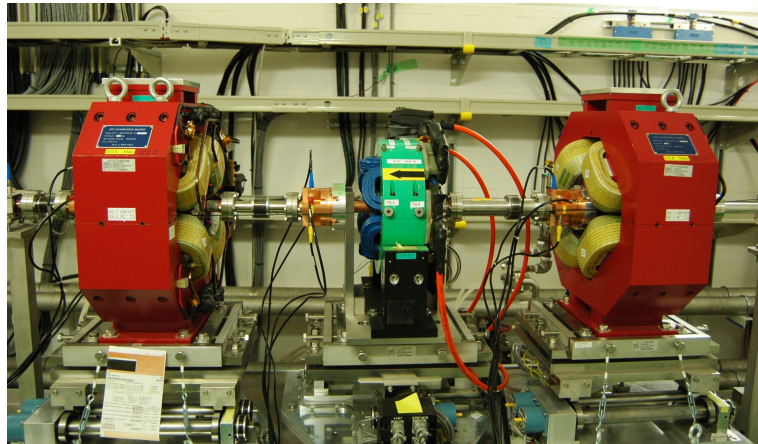


Figure 5.2: Photo of three cavity BPMs installed at the ATF2 final focus beamline. Each beam position monitor is mounted on a mover system shared by its neighbouring magnet.

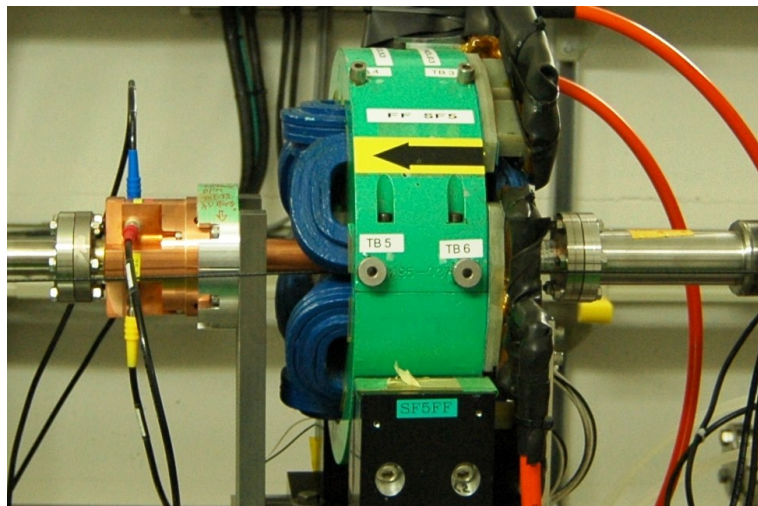


Figure 5.3: Photo of dipole cavity BPM in situ on the ATF2 final focus beamline.



Figure 5.4: Photo of one of the C-band cavity BPMs before installation.

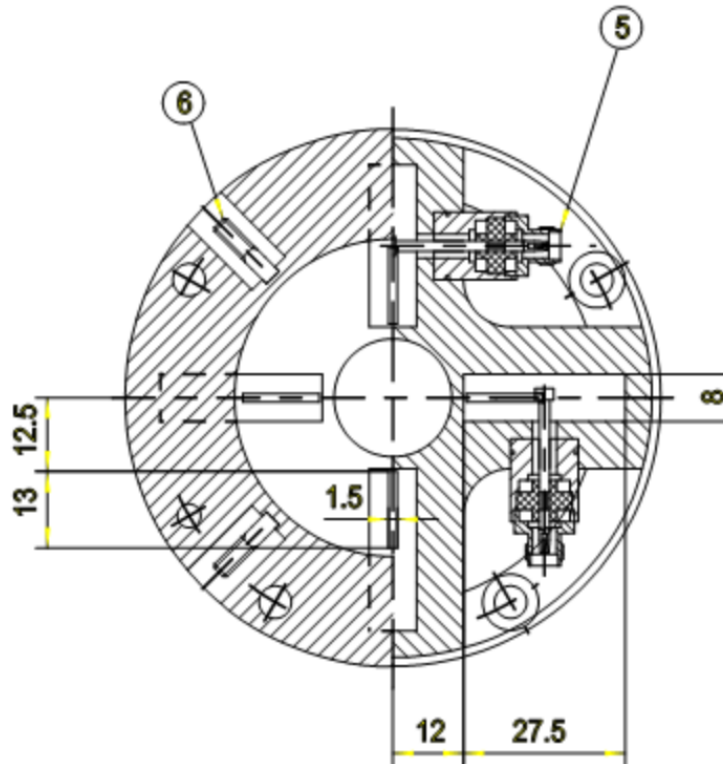


Figure 5.5: Engineering schematic of a C-band dipole cavity.

transverse magnetic modes). Figure 5.3 shows a photograph of a dipole cavity installed next to a sextupole at ATF2, figure 5.4 shows a photograph of one of the C-band<sup>1</sup> dipole cavities pre-installation at ATF2 (see figure 5.5 [104] for an engineering drawing of one of these cavities) and figure 5.6 shows a reference cavity. It can be seen that the reference cavity has only one signal pickoff point whereas the dipole cavity has four. This is due to the fact that the monopole mode is dependent entirely on the beam charge whereas the dipole mode also has a position dependence. For the dipole cavity two opposing pickoffs are for position measurement along the  $x$ -axis and two along the  $y$ -axis (see chapter 4).

### 5.1.2 Movers

Of the 32 C-band cavities 23 are mounted on movers (see for example figure 5.7) which allow movement of the cavity relative to the remainder of the beamline. These movers are shared

<sup>1</sup>C-band refers to the operating frequency of the BPMs, the C-band region of RF frequencies is commonly described, using the IEEE standard, to be between 4 and 8 GHz. In this case the operating frequency is 6.426 GHz

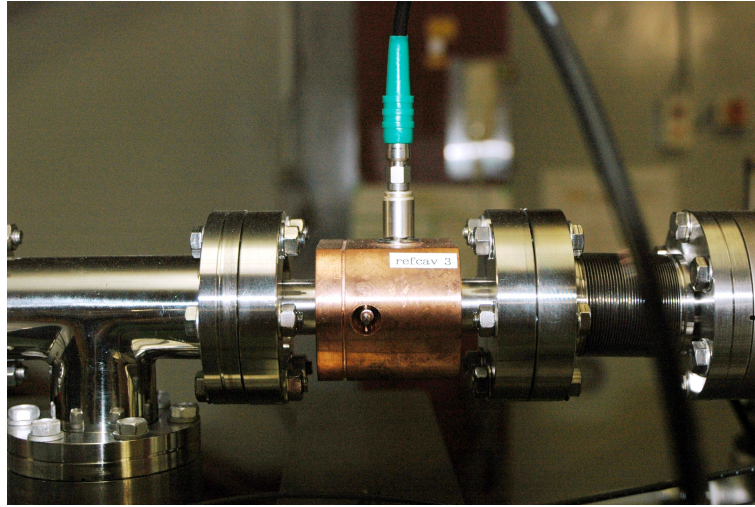


Figure 5.6: Photo of a reference cavity installed in the final focus beamline at ATF2.

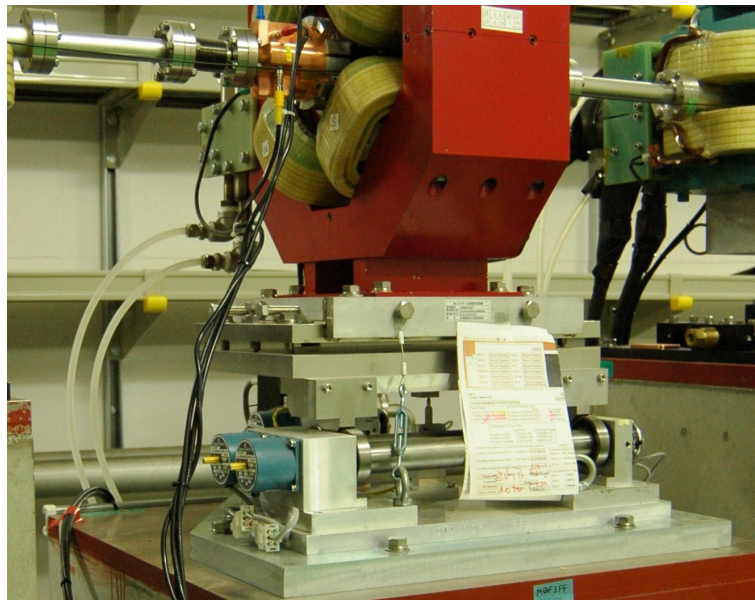


Figure 5.7: Photo of cavity BPM with quadrupole mounted on a mechanical mover. The mover is made up of a steel plate which sits on three cylindrical camming devices.

with quadrupoles and sextupoles with the cavities placed just downstream of each magnet; each mover moves a cavity and its neighbouring magnet simultaneously. The movers consist of a plate, upon which the magnet is mounted, supported by three cylindrical cams driven by stepper motors with potentiometer readbacks [105]. The cams are set off centre allowing movement in the  $x$  and  $y$  directions whilst also allowing the plate to be tilted (variation of azimuthal angle).

This mover system is ideal for use in the calibration of the cavity BPMs. Its sub micron movement capability combined with high resolution LVDTs (linear voltage displacement transducers) for mover position measurement [106] make it possible to have highly accurate calibration procedures. Calibration of the beam position monitors using the mover system will be discussed later in this chapter.

### 5.1.3 Mixing Electronics

For this BPM system the signal processing was done in two parts, the initial processing using electronics, then completed using software analysis techniques. First each pair of signals (two for  $x$ -measurement and two for  $y$ -measurement) is summed through use of a hybrid, increasing the available signal to allow a more accurate position measurement. The signals are then input to the mixing electronics giving a signal which has been down mixed from 6.426 GHz to 20 MHz [107]. A diagram of the electronic processing scheme may be seen in figure 5.8 with the major heterodyne components highlighted (see section 4.2.1) in pink.

### 5.1.4 Digitization and Timing System

Since the BPM output signal has now been down mixed electronically to give a signal of severely reduced frequency, the data from the BPM are easier to handle. The 20 MHz signals are then processed by SIS digitizers. For data acquisition SIS3301 eight channel digitizer ADC VME boards with 14 bit resolution were used [108]. The digitization clock was at

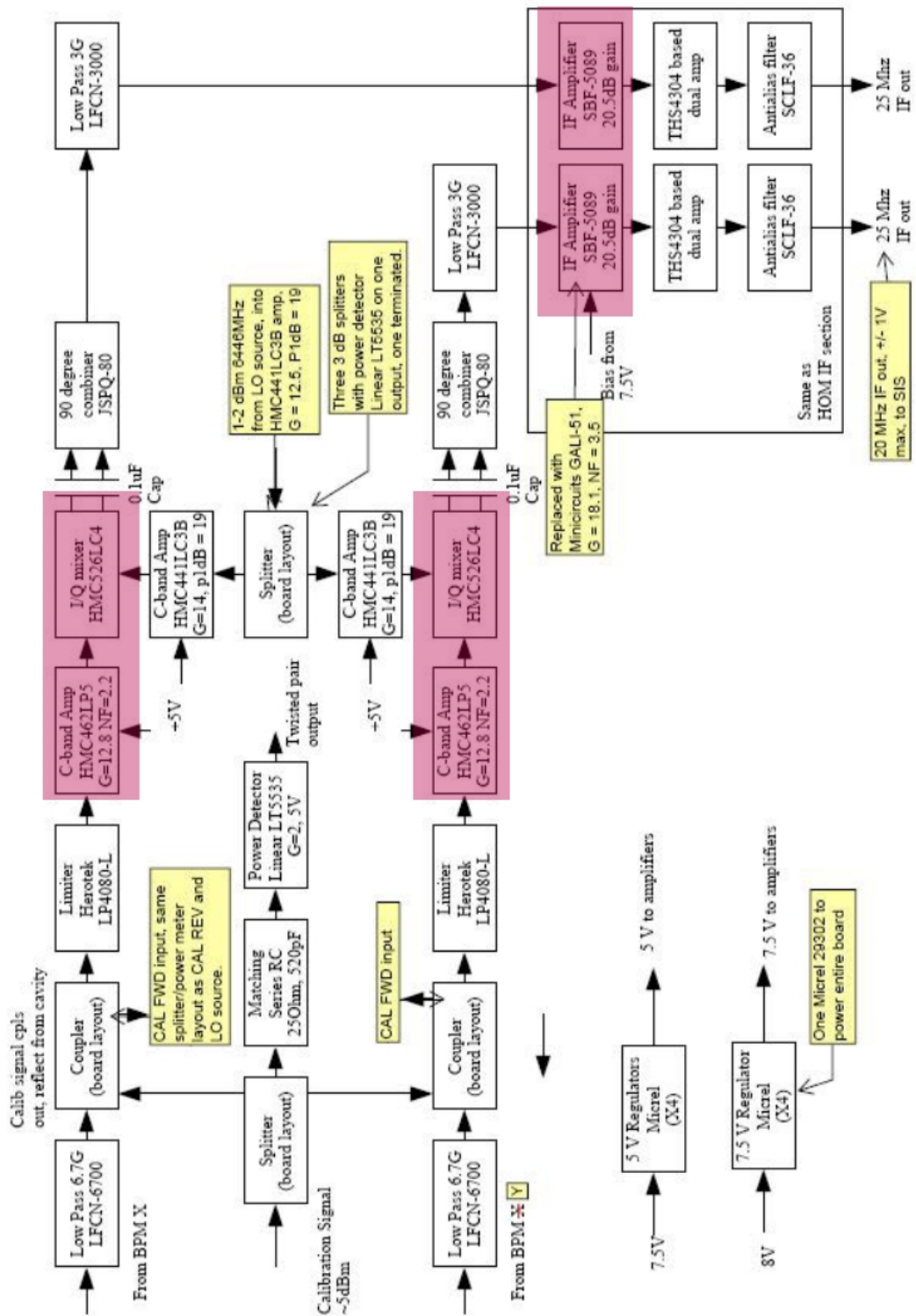


Figure 5.8: Block diagram of mixing electronics scheme for processing of cavity BPM output signals [107].

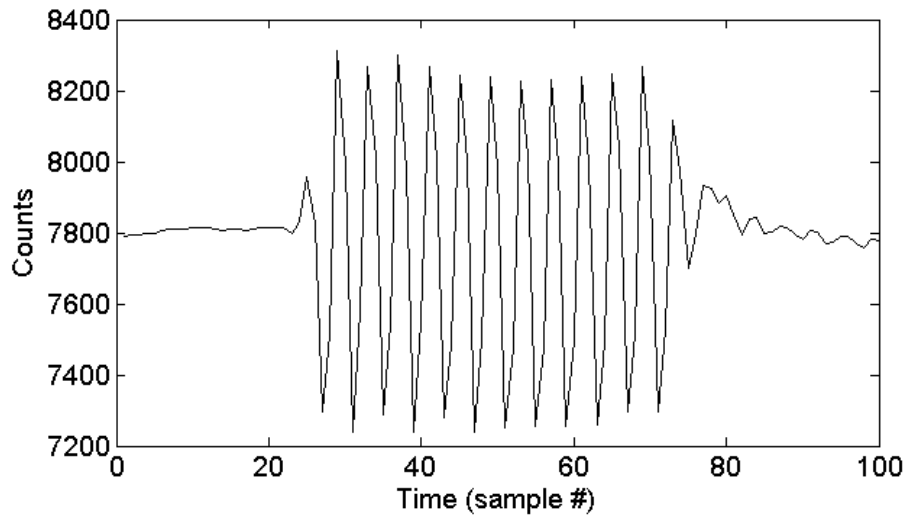


Figure 5.9: Plot of calibration tone Signal, with a sampling rate of 100 MHz giving 10 ns per sample.

a frequency of 103 MHz using the timing system shown in figure A.2, appendix A. The figure shows the method of generation of all RF signals required by the cavity BPM system, including clocks and triggers for digitizers along with the local oscillator and calibration tone signals (discussed in the next section).

### 5.1.5 Local Oscillator and Calibration Tone Systems

Figure A.3 (appendix A) shows the method of distribution of the local oscillator (LO) and calibration tone signals. The 6.446 GHz LO is generated using a signal derived from the ATF master oscillator and distributed to the mixing electronics for each BPM (figure 5.8).

#### Calibration Tone

Figure 5.9 shows an example of the digitized output of the electronics of one of the C-band dipole cavities when a calibration tone (or caltone) is input. The calibration tone will allow continuous measurement of the gain provided by the BPM electronics [109].

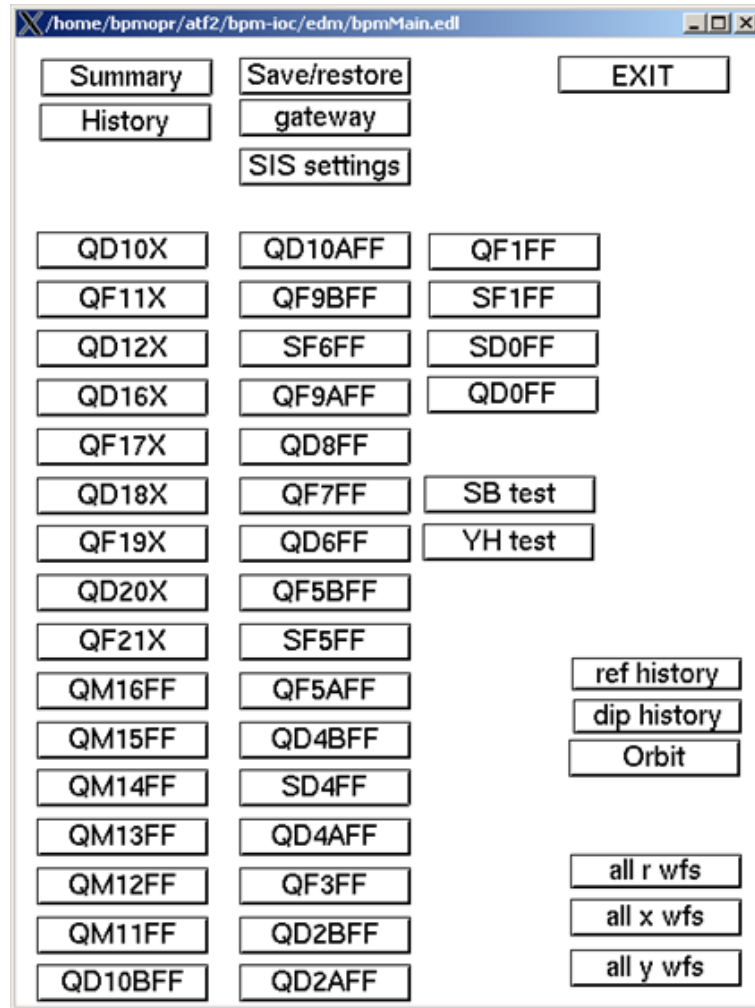


Figure 5.10: A screen shot showing the main panel of the cavity BPM data acquisition software.

## 5.2 Software

The digitized output of the beam position monitors is then handled using an EPICS (Experimental Physics and Industrial Control System [110]) IOC (Input-Output Controller). Figures 5.10, 5.11 and 5.12 show screen shots [111] of various EPICS control panels, built using the EPICS EDM (Extensible Display Manager), allowing the user to observe the output of each BPM and any other information available to EPICS. The digitized output of the beam position monitors undergoes further processing using software, with the results also input to EPICS. This waveform processing is detailed in the next section.

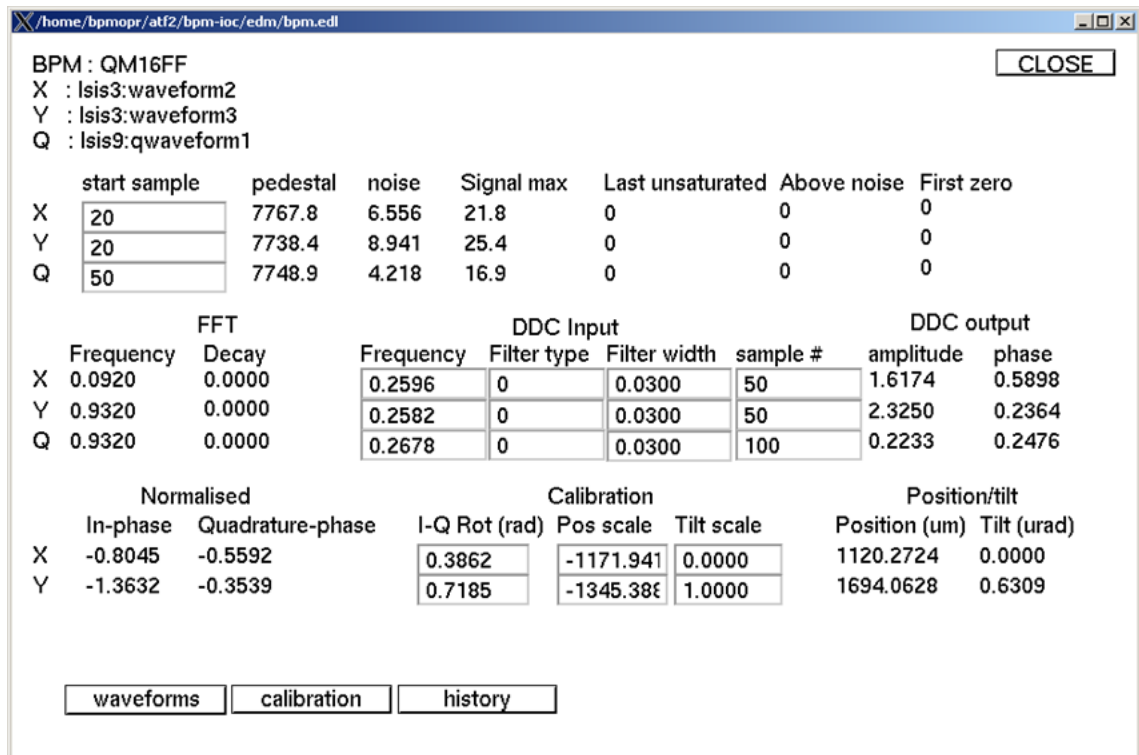


Figure 5.11: A screen shot showing an example of the parameters used in the waveform analysis for the BPM designated as QM16FF.

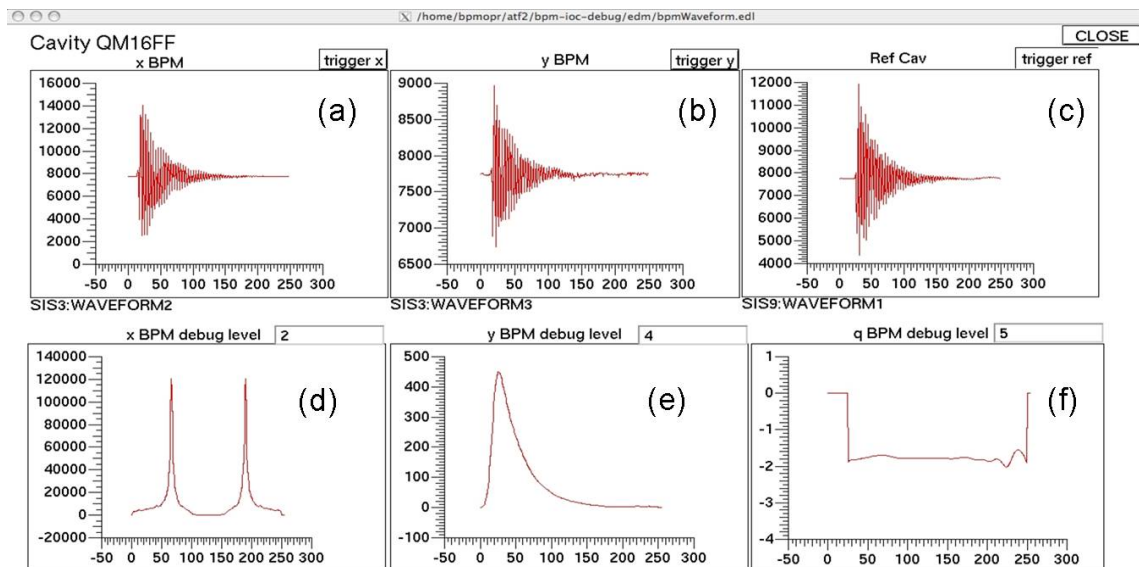


Figure 5.12: Screen shot of the waveform display, (a), (b) and (c) respectively show the digitized waveforms for the  $x$  and  $y$  axis of QM16FF alongside the monopole signal from the reference cavity. Also shown are the various stages of the BPM waveform software analysis, described in section 4.2.2. (d) is the fourier transform of the waveform, (e) is the envelope of the waveform and (f) is the phase.

## 5.3 Waveform Analysis

Figure 5.13 shows an example of the raw waveform of the cavity as output by the SIS digitizers. This waveform is the output for a single bunch passing through a cavity with mover positioned at  $x, y = -200 \mu\text{m}$ . Recalling that the signal is of the form

$$V(t) = Ae^{-\Gamma t} \sin(\omega t + \phi) \quad (5.1)$$

Where  $V(t)$  is the electronics output voltage,  $A$  is the amplitude,  $\phi$  the phase and  $\Gamma$  the decay constant of the waveform (with  $\Gamma = 1/\tau$ ), the first step in the waveform analysis is to determine  $A$ ,  $\omega$ ,  $\phi$  and  $\tau$  (see section 4.2.2) in order that  $I$  and  $Q$  may be calculated as in section 4.2.3.

### 5.3.1 Tuning

For the waveform to be made suitable for beam position measurements it must first be mixed with a local oscillator (as described in section 4.2.2) with frequency the same as that of the waveform. This frequency is most easily determined by observing the variation of phase  $\phi$  with frequency. When the LO is of the correct frequency a plot of the phase will become flattened as opposed to saw toothed, as shown in figure 5.14. The reason for this shape is that the maximum possible variation of phase is  $2\pi$ , here the range is  $\pm\pi$  due to an artifact of the data acquisition.

Table 5.1 shows the calculated frequencies (using BPM data collected during beam operation, to be referred to as online measurements) for each of the C-band cavity BPMs along with the  $Q$  values, as determined using

$$Q_L = \omega\tau \quad (5.2)$$

and  $\Gamma = 1/\tau$ . Also shown are the data taken during measurements performed on the cavities before installation (to be referred to as offline measurements) in the beamline (see appendix A

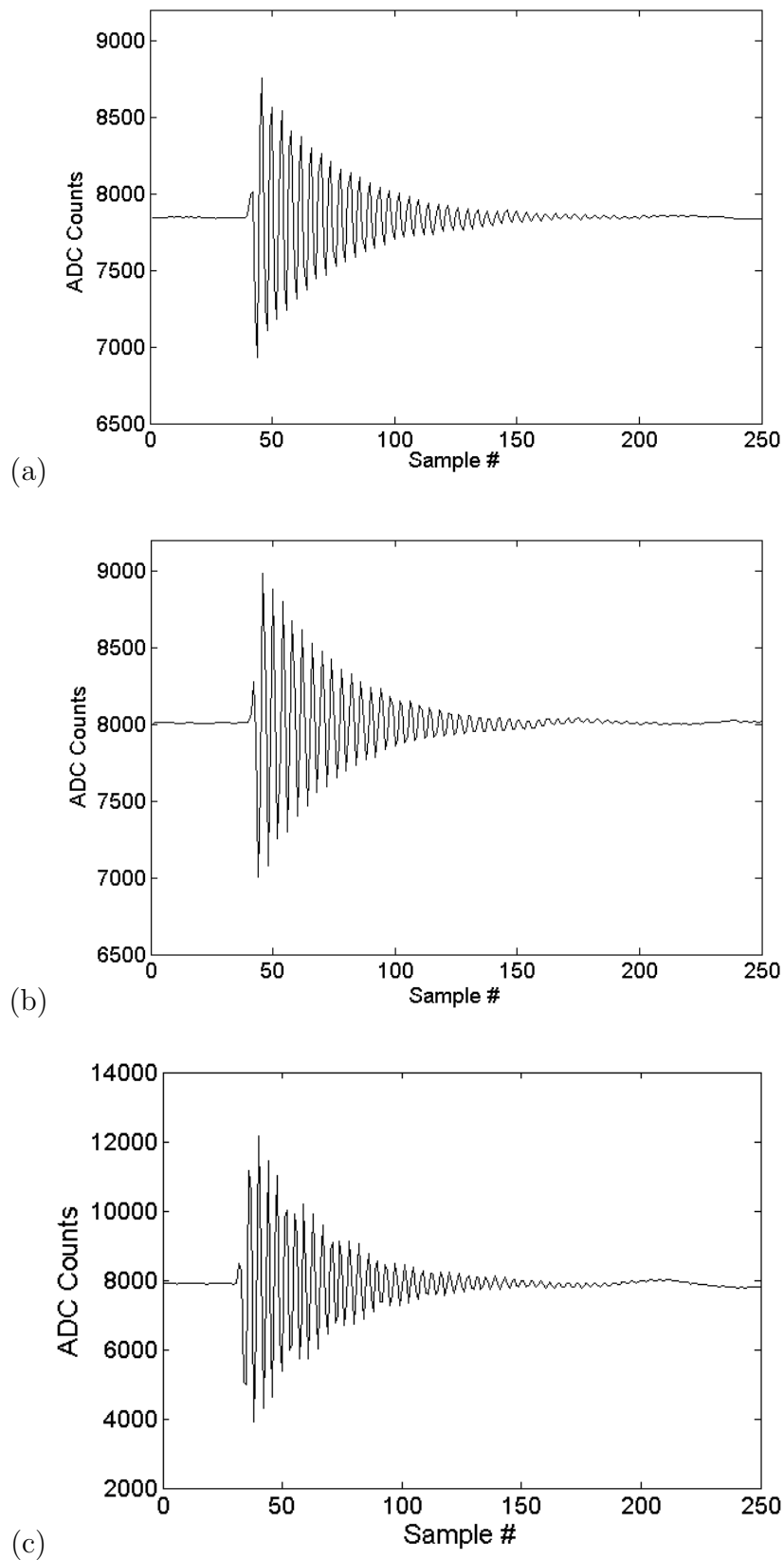


Figure 5.13: Example of a waveform output from the cavity beam position monitor QD10AFF. (a) shows the output for the  $x$ -axis, (b) for the  $y$ -axis and (c) for the reference cavity created by the first bunch passing through the cavity during a calibration procedure. As with all data acquired using the SIS digitisation system we have a sampling rate of 100 MHz giving 10 ns per sample.

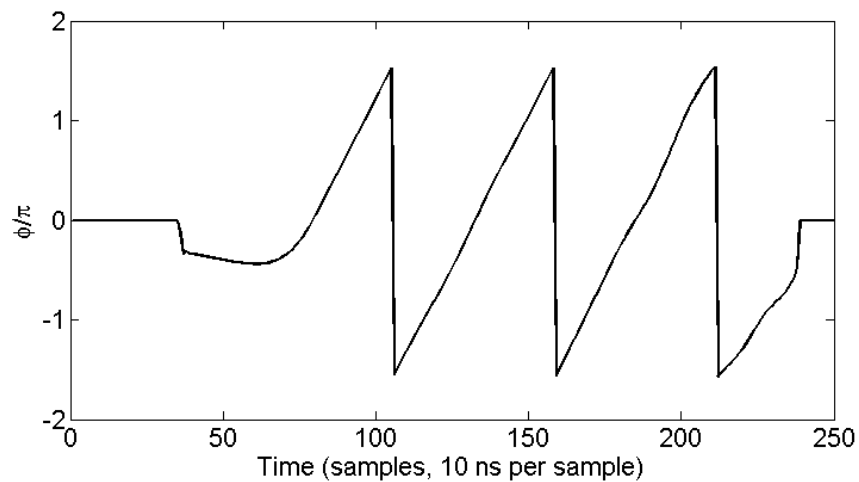


Figure 5.14: Phase vs time for a single waveform output from an untuned cavity BPM.

for hardware measurement procedure) for comparison. It can be seen that there is significant deviation of the online values for  $Q$  and frequency from those measured offline with the  $Q$  values looking more favourable when measured on the beamline. This is due to offline measurements being more difficult to perform accurately and the available equipment used having poorer resolution than that available during beam operation (online measurements).

This waveform analysis is performed using online analysis software. Values of  $I$  and  $Q$  calculated online differ from those calculated offline (using MATLAB). The reason for this difference is undetermined but of no major significance since there is an exceptionally high correlation between  $I/Q$  calculated online and  $I/Q$  calculated offline; this is illustrated in figure 5.15 where the correlation coefficient,  $\rho = 0.9979$ .

## 5.4 Calibration

This section will consider two calibration methods; the first concerning the magnet mover system and the second the variation of beam position using a bump in the beam created with dipole corrector magnets (see section 5.4.2).

BPM	$f_x^{off}$ (GHz)	$f_x^{on}$ (GHz)	$Q_x^{off}$	$Q_x^{on}$	$f_y^{off}$ (GHz)	$f_y^{on}$ (GHz)	$Q_y^{off}$	$Q_y^{on}$
QM15FF	6.423825	6.219 ± 0.034	6050.6	4966.4	6.424171	6.335 ± 0.029	6005.7	5290.4
QM14FF	6.423772	6.432 ± 0.018	6137.4	4446.1	6.423851	6.402 ± 0.035	6033.7	3833.3
QM13FF	6.423612	6.449 ± 0.020	6050.4	4843.5	6.423586	6.463 ± 0.023	6090.5	4880.9
QM12FF	6.423612	6.365 ± 0.013	6244.5	4640.4	6.423586	6.366 ± 0.022	6330.6	4450.4
QM11FF	6.423798	6.401 ± 0.003	6149.0	5024.3	6.423719	6.426 ± 0.014	6102.2	4718.9
QD10BFF	6.423878	6.388 ± 0.017	6166.8	4475.2	6.423878	6.391 ± 0.021	6190.6	4344.1
QD10AFF	6.423745	6.430 ± 0.013	6287.3	4802.4	6.423798	6.423 ± 0.021	6178.6	5191.0
QF9BFF	6.423612	6.457 ± 0.016	6244.5	4894.9	6.423586	6.465 ± 0.008	6330.6	5445.4
SF6FF	6.423878	6.377 ± 0.017	6114.1	4685.4	6.423904	6.372 ± 0.019	5949.9	4459.2
QF9AFF	6.423612	6.448 ± 0.015	6108.0	5332.5	6.423559	6.462 ± 0.021	6208.3	5639.6
QD8FF	6.423559	6.473 ± 0.021	6067.6	5575.8	6.423559	6.469 ± 0.015	6119.6	5128.5
QF7FF	6.423719	6.430 ± 0.033	6039.2	5054.1	6.423639	6.455 ± 0.039	6142.1	5008.2
QD6FF	6.423798	6.407 ± 0.027	6090.8	5467.3	6.423904	6.386 ± 0.020	6202.7	4637.2
QF5BFF	6.423559	6.464 ± 0.015	6274.9	5329.9	6.423559	6.473 ± 0.015	6284.9	5227.0
SF5FF	6.423921	6.373 ± 0.017	6085.2	4967.6	6.423904	6.378 ± 0.026	6050.8	5604.8
QF5AFF	6.423798	6.406 ± 0.019	6016.7	4859.4	6.423612	6.453 ± 0.019	5999.7	4952.3
QD4BFF	6.423692	6.442 ± 0.023	6067.7	5770.2	6.423745	6.432 ± 0.023	5949.7	4493.5
SD4FF	6.423665	6.423 ± 0.022	5983.0	4413.5	6.423665	6.428 ± 0.300	6022.3	5528.0
QD4AFF	6.423745	6.427 ± 0.025	6160.8	5598.7	6.423745	6.423 ± 0.020	6184.6	5536.0
QF3FF	6.423612	6.463 ± 0.370	6143.0	4700.5	6.423506	6.491 ± 0.022	6154.7	4937.3
QD2BFF	6.424037	6.355 ± 0.018	5966.4	4543.2	6.424037	6.365 ± 0.010	6039.0	4410.5
QD2AFF	6.424037	6.347 ± 0.361	5933.6	4326.9	6.424037	6.350 ± 0.017	5868.6	4323.1

Table 5.1: Table to compare frequency and quality factors of cavity BPMs as measured online and offline (offline measurements by Y. Honda [112], see appendix A).  $f_x^{off}$  (GHz) and  $f_x^{on}$  (GHz) are the  $x$  - channel resonant dipole cavity frequencies measured offline (using a network analyzer) and online (using the beam) respectively,  $Q_x^{off}$   $Q_x^{on}$  are the  $x$  - channel quality factors measured offline and online respectively,  $f_y^{off}$  (GHz)  $f_y^{on}$  (GHz) are the  $y$  - channel resonant dipole cavity frequencies measured offline and online respectively and  $Q_y^{off}$   $Q_y^{on}$  are the  $y$  - channel resonant dipole cavity frequencies measured offline and online respectively.

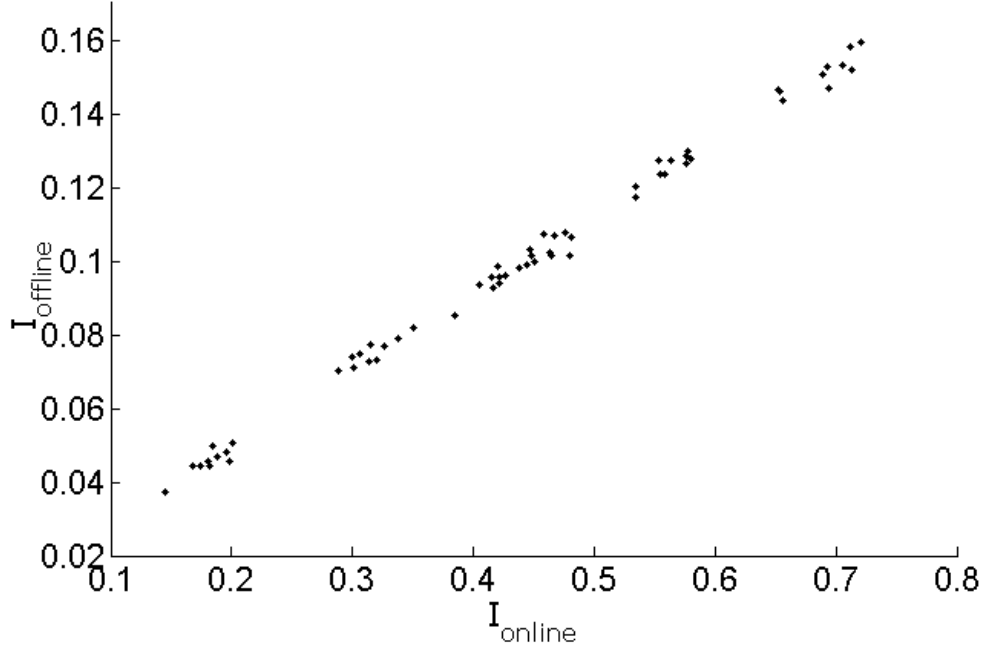


Figure 5.15:  $I$  calculated offline (using MATLAB) vs  $I$  calculated by the online data acquisition system.

#### 5.4.1 Mover Calibration

The beam position monitor with designation QD10AFF, which sits approximately half way down the final focus beam line (figure 5.1), shall be used as an example of calibration by magnet mover. The BPM was moved transverse to the beampipe and data recorded at regular intervals during the movement. For each of the  $x$  and  $y$  directions the BPM was moved by  $\pm 200 \mu\text{m}$  in steps of  $100 \mu\text{m}$  and 10 bunches were measured at each position (figure 5.16).

As the BPM moves such that the beam is away from the centre of the cavity the amplitude of the output signal increases (figure 5.17). As the beam approaches the centre of the cavity it reduces to a minimum and again begins to rise as the movement continues through the zero point and into the other half of the cavity. As the beam crosses the centre of the cavity its phase output is also changed. Figure 5.18 shows a phase jump of  $\pi$  rad as the beam passes through zero. This is seen to occur at bunch number 30 which is consistent with the minimal amplitude and mover displacement at this point. Using the plotted values for amplitude and phase the in-phase and quadrature-phase components of the waveform may

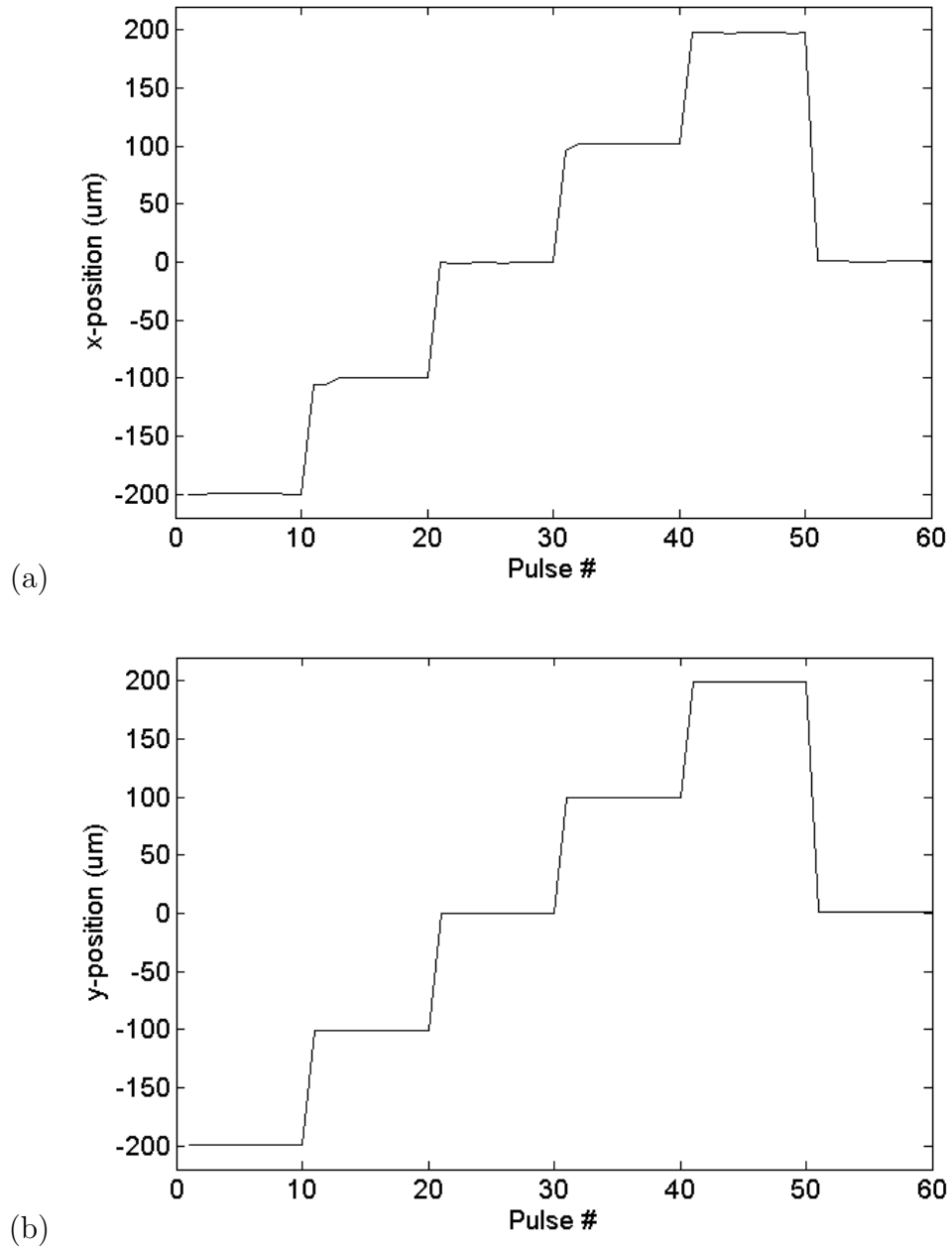


Figure 5.16: BPM position vs pulse number for  $x$  (a) and  $y$  (b) directions for a typical calibration procedure.

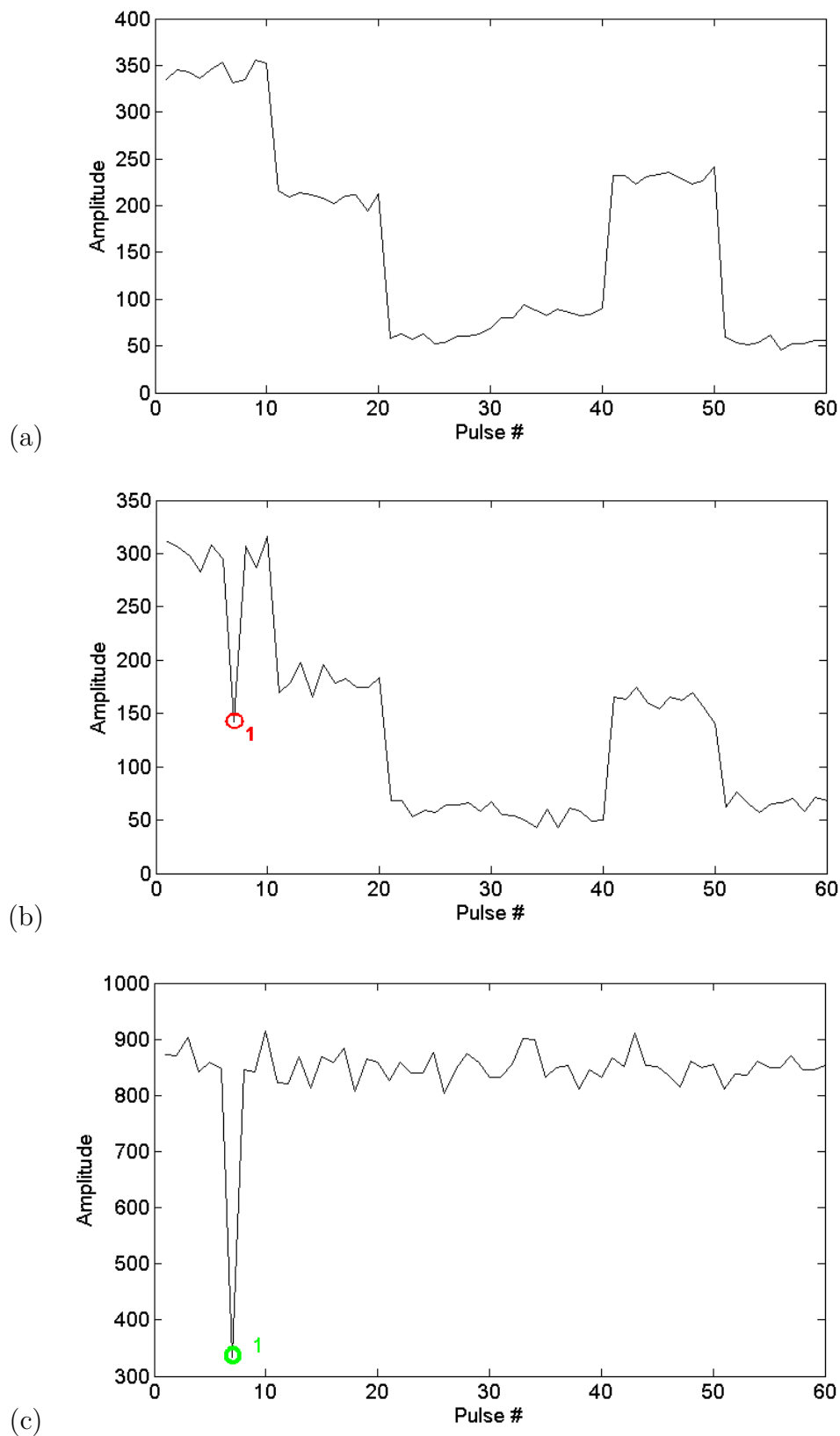


Figure 5.17: BPM signal amplitude vs pulse number for BPM QD10AFF during a mover calibration procedure; (a) shows the output for the  $x$ -axis, (b) for the  $y$ -axis and (c) for the reference cavity. The change in amplitude at pulses 30 and 50 is due not only to the movement of the BPM but also to the change in phase (figure 5.18). See the section titled Bunch Charge Effect later in this section for an explanation of the flyers labelled 1.

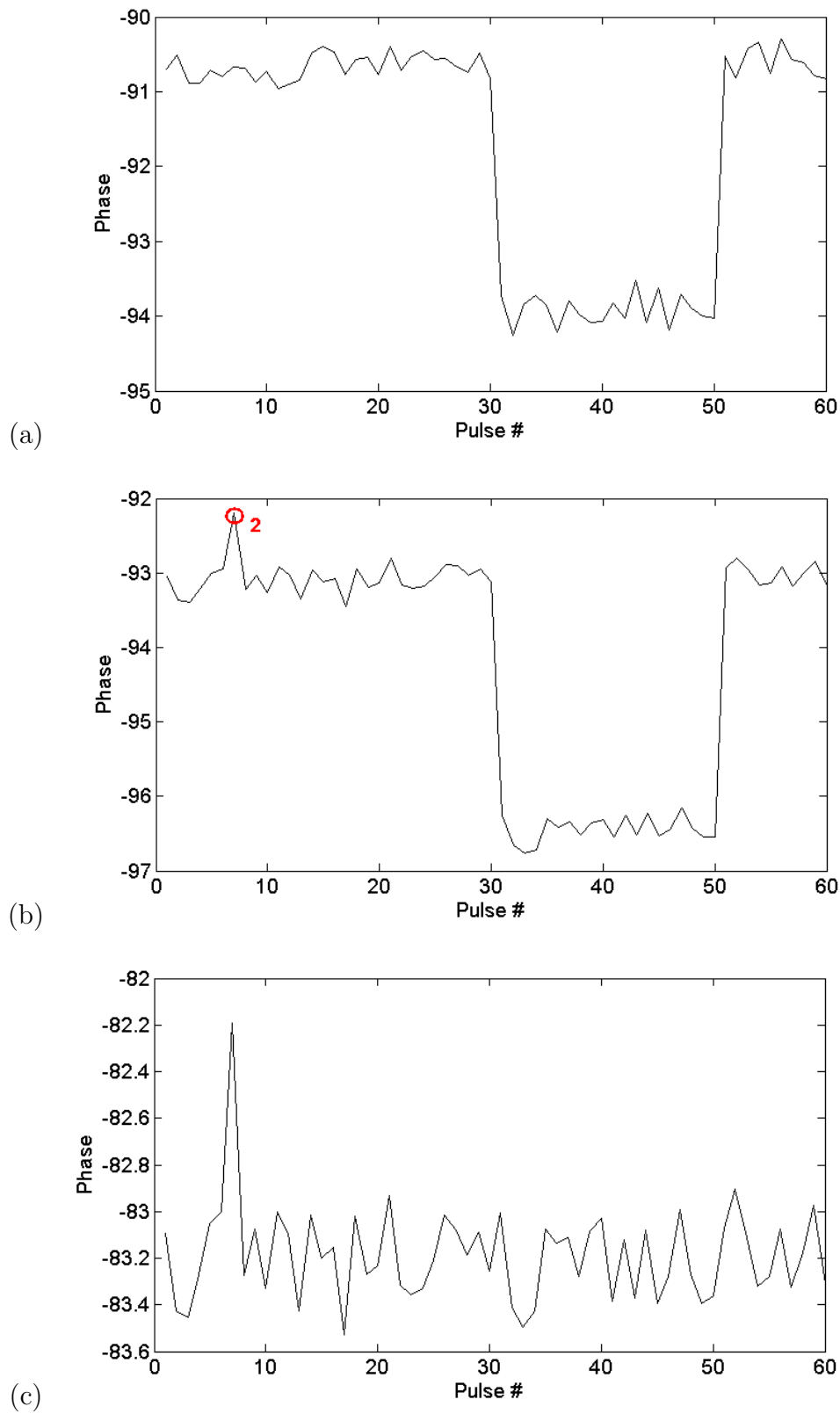


Figure 5.18: Phase vs pulse number for BPM QD10AFF during a mover calibration procedure; (a) shows the output for the  $x$ -axis, (b) for the  $y$ -axis and (c) for the reference cavity. The  $\pi$  phase jump seen at pulses number 30 and 50 is due to the beam passing through the electrical centre of the cavity.

be calculated.

When values for  $I$  and  $Q$  have been determined using the method outlined in chapter 4 a rotation is applied as follows.

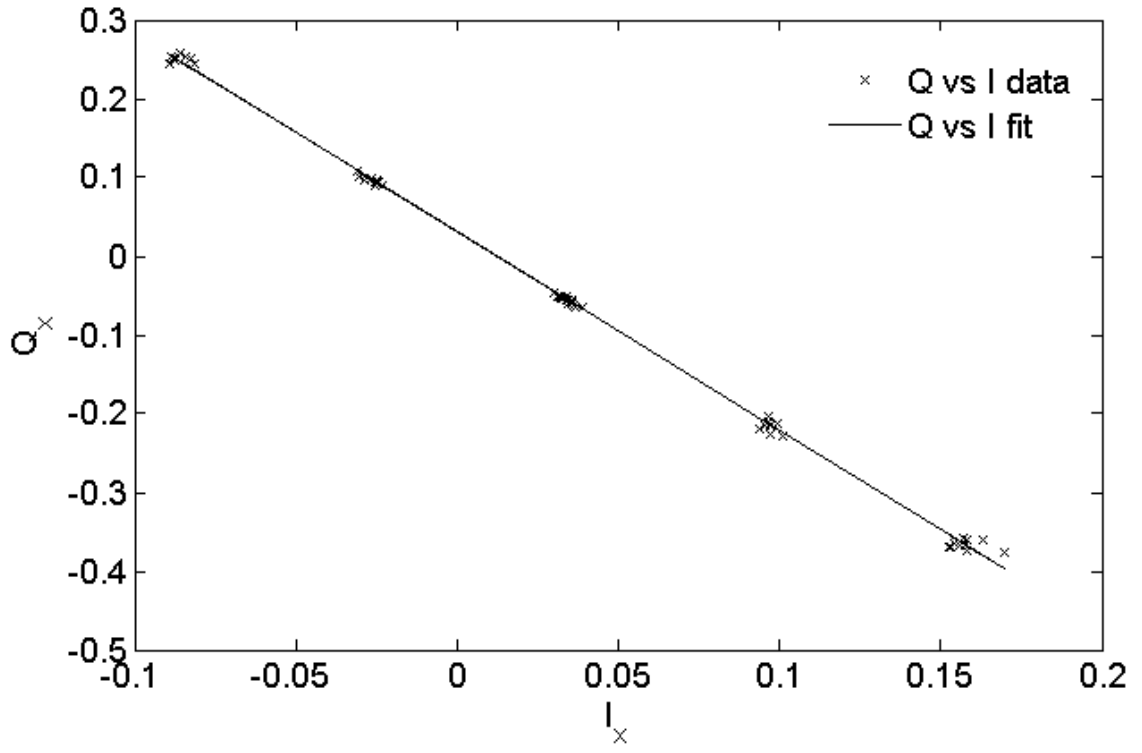
$$\begin{pmatrix} I' \\ Q' \end{pmatrix} = \begin{pmatrix} \cos(\theta_{iq}) & \sin(\theta_{iq}) \\ -\sin(\theta_{iq}) & \cos(\theta_{iq}) \end{pmatrix} \begin{pmatrix} I \\ Q \end{pmatrix} \quad (5.3)$$

Where  $\theta_{iq} = \tan^{-1}(m_{iq})$  and  $m_{iq}$  is the gradient of the  $Q$  vs  $I$  linear fit (see figure 5.19).

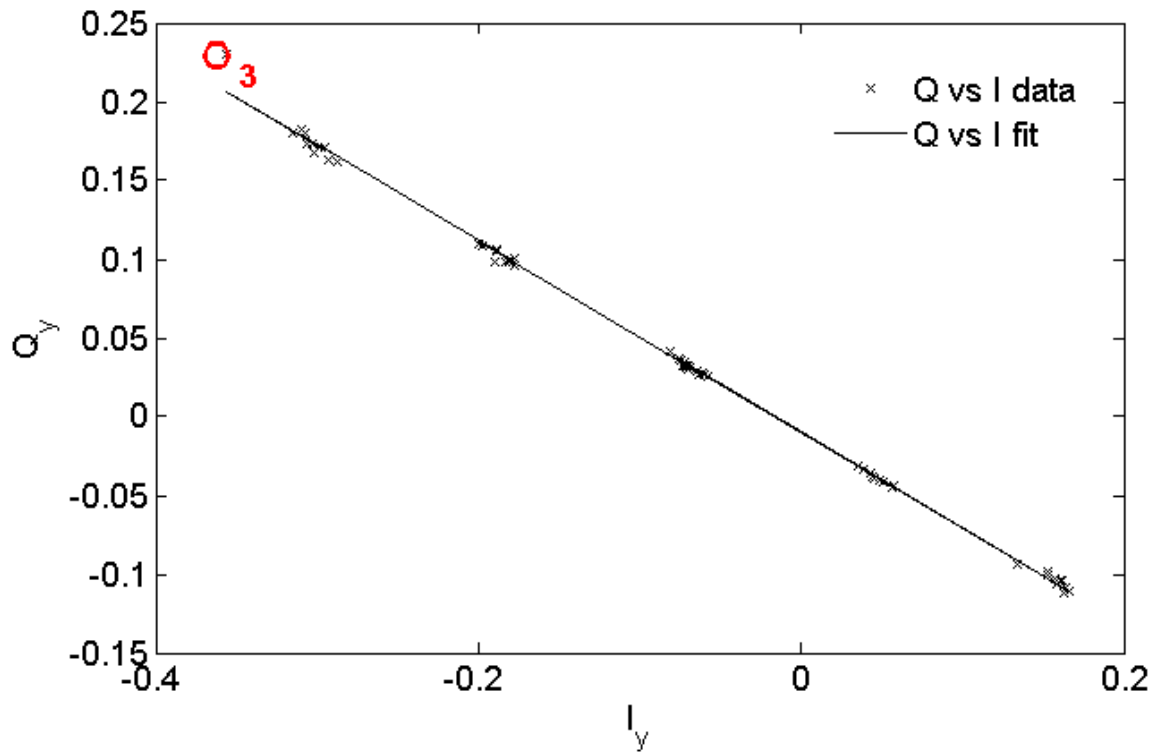
After the rotation is applied the resulting  $I'$  should be mostly dependent (there may be some slight charge dependence due to mixing of modes, as shown in figure 4.2. This effect is not considered to be significant in this case) on position and  $Q'$  mostly independent (there may also be some slight position dependence) of beam position (figure 5.20). Table 5.2 shows the rotation angles,  $\theta_{iq}$ , and scaling factors calculated for all 23 C-band mover-mounted BPMs. The scaling factor is taken as the gradient of the graph of  $I'$  vs BPM position. QM15FF and QM14FF have less attenuation so the scale factors are different and calibration of QM16FF was unsuccessful due to there being no correlation between  $I$  and  $Q$  (it is thought that the RF cables used to carry the signal from the BPM to the mixing electronics were incorrectly connected).

### Errors Due to Machine Behaviour

Figures 5.17 - 5.20 each show a point (red circles 1 - 3), at the 7th bunch in the calibration procedure, far outside the expected value. This is due to the exceptionally low charge of the electron bunch. This low charge produces a monopole mode in the reference cavity which is very small in amplitude. Such a small signal may prevent the phase from being accurately determined, causing the charge normalization to be incorrect and causing subsequently calculated variables to be uncharacteristic of the norm. All pulses with very low charge were excluded from fits to the data and further analysis.



(a)



(b)

Figure 5.19:  $Q$  vs  $I$  plot for (a)  $x$ -plane and (b)  $y$ -plane of cavity BPM QD10AFF giving a rotation angle of  $-1.1932$  and  $-0.5464$  rad

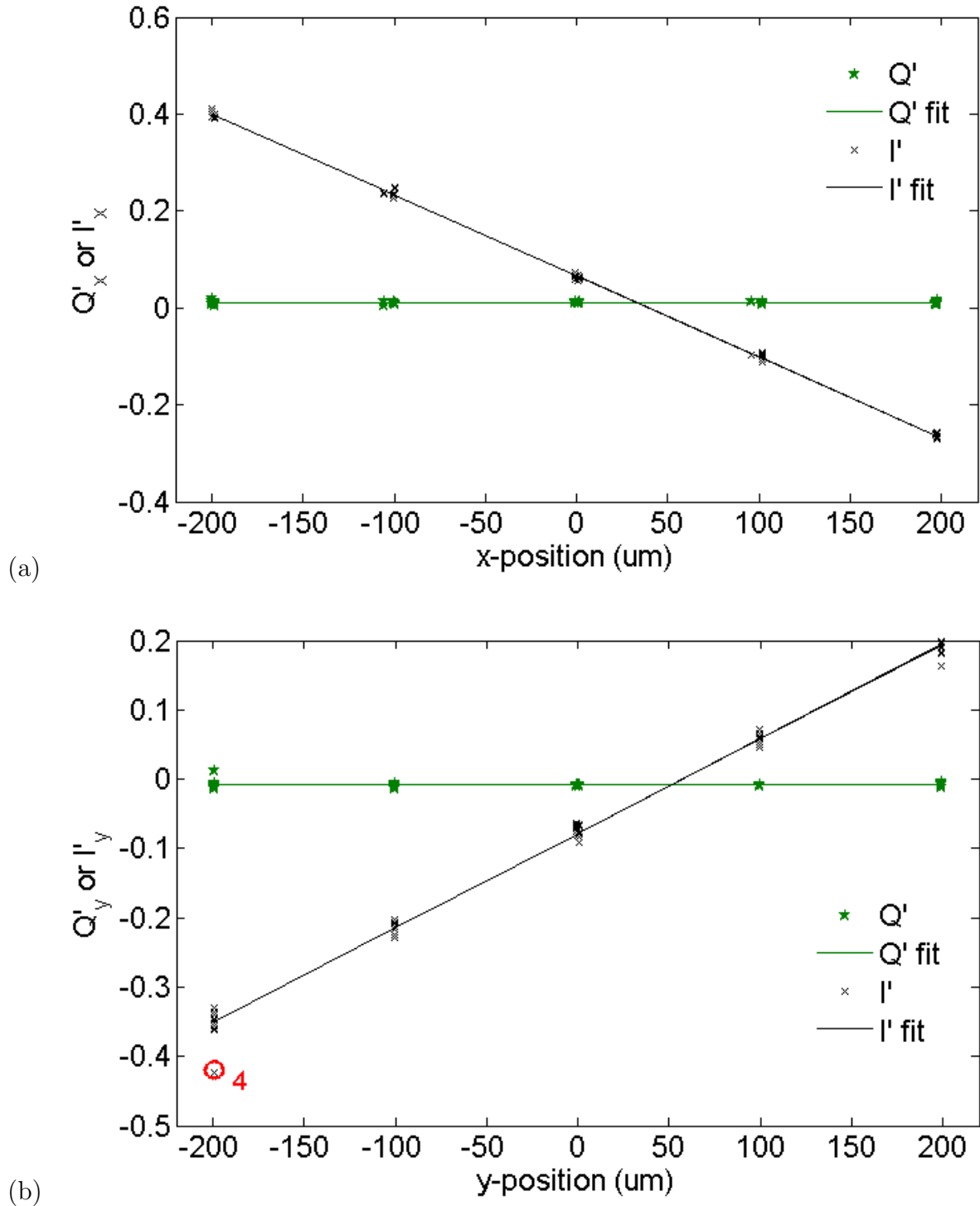


Figure 5.20:  $I'$  and  $Q'$  vs beam position plot for cavity BPM QD10AFF (a)  $x$ -plane and (b)  $y$ -plane of cavity BPM QD10AFF.

BPM	$\theta_{x_{i,q}}$ (rad)	$x$ -scale ( $\mu\text{m}$ )	$\theta_{y_{i,q}}$ (rad)	$y$ -scale ( $\mu\text{m}$ )
QM16FF	$0.006 \pm 0.110$	$-1.451 \times 10^7 \pm 12 \times 10^6$	$1.289 \pm 0.0091$	$-805.9 \pm 3.8$
QM15FF	$-0.712 \pm 0.002$	$-54.0 \pm 0.8$	$0.251 \pm 0.0047$	$-65.4 \pm 0.4$
QM14FF	$-1.324 \pm 0.006$	$-46.1 \pm 1.3$	$-1.449 \pm 0.0007$	$-48.1 \pm 0.3$
QM13FF	$-0.439 \pm 0.005$	$-730.4 \pm 50.3$	$-0.556 \pm 0.0050$	$-572.9 \pm 3.5$
QM12FF	$-0.730 \pm 0.004$	$-596.0 \pm 18.1$	$0.063 \pm 0.0020$	$-487.3 \pm 2.3$
QM11FF	$-1.059 \pm 0.002$	$-723.4 \pm 15.9$	$-1.013 \pm 0.0012$	$-590.6 \pm 3.8$
QD10BFF	$-0.799 \pm 0.002$	$-620.6 \pm 6.1$	$-0.165 \pm 0.0098$	$-584.6 \pm 12.2$
QD10AFF	$-1.193 \pm 0.002$	$599.2 \pm 2.1$	$-0.546 \pm 0.0024$	$-732.6 \pm 7.3$
QF9BFF	$1.380 \pm 0.002$	$-543.6 \pm 6.9$	$-1.250 \pm 0.0043$	$-660.6 \pm 6.3$
SF6FF	$-0.102 \pm 0.018$	$569.8 \pm 16.6$	$-0.679 \pm 0.0058$	$-837.2 \pm 9.9$
QF9AFF	$0.265 \pm 0.004$	$766.6 \pm 14.0$	$-0.764 \pm 0.0046$	$-577.2 \pm 4.5$
QD8FF	$-0.350 \pm 0.003$	$586.2 \pm 8.7$	$0.002 \pm 0.0018$	$-759.0 \pm 8.2$
QF7FF	$-1.172 \pm 0.003$	$649.8 \pm 22.5$	$0.127 \pm 0.0023$	$-637.4 \pm 3.2$
QD6FF	$-0.674 \pm 0.002$	$535.4 \pm 17.6$	$0.331 \pm 0.0022$	$853.9 \pm 3.1$
QF5BFF	$-1.356 \pm 0.006$	$733.6 \pm 48.7$	$0.115 \pm 0.0046$	$541.0 \pm 4.0$
SF5FF	$-0.485 \pm 0.019$	$736.7 \pm 57.5$	$0.290 \pm 0.0069$	$616.2 \pm 5.8$
QF5AFF	$0.565 \pm 0.002$	$-649.2 \pm 50.9$	$0.131 \pm 0.0042$	$544.1 \pm 5.5$
QD4BFF	$-0.335 \pm 0.002$	$501.9 \pm 13.8$	$-0.965 \pm 0.0057$	$639.4 \pm 9.6$
SD4FF	$0.248 \pm 0.002$	$-634.8 \pm 12.2$	$-0.397 \pm 0.0058$	$669.7 \pm 12.9$
QD4AFF	$-0.754 \pm 0.002$	$550.7 \pm 3.5$	$-0.638 \pm 0.0041$	$645.5 \pm 13.3$
QF3FF	$1.389 \pm 0.003$	$-816.6 \pm 43.8$	$-0.412 \pm 0.0026$	$800.6 \pm 5.2$
QD2BFF	$0.655 \pm 0.002$	$515.4 \pm 18.1$	$0.561 \pm 0.0075$	$615.8 \pm 10.4$
QD2AFF	$0.634 \pm 0.004$	$1231.5 \pm 45.9$	$0.537 \pm 0.0067$	$-715.0 \pm 11.2$

Table 5.2: Calibration results for all 23 mover mounted ATF cavity BPMs.

### Quadrupole Effect

Each cavity is mounted on a mover together with a quadrupole. The cavity is placed just inside the quadrupole at the downstream end (see figure 5.7), the effect of this quadrupole can be characterized as follows

$$\frac{d^2x}{ds^2} = -k(s)x_i \quad (5.4)$$

where  $x_i$  is the initial position of the beam as it enters the quadrupole,  $s$  is the longitudinal position along the beampipe and  $k(s)$  is the magnet focussing coefficient which is dictated by the field in the magnet as follows

$$k = \frac{B_0}{B_\rho a_0} \quad (5.5)$$

where  $B_0$  is the tip field,  $a_0$  the tip radius and  $B_\rho$  the magnetic rigidity. Here the thin lens approximation may be used to give

$$\Delta x' = -Kx \quad (5.6)$$

where  $K = kl_q$  and  $l_q$  is the length of the quad. For example QD10AFF with a current of  $I = 17.34\text{A}$  (as was the case at the time of calibration) gives  $K = 0.38\text{m}^{-1}$  and so  $\Delta x$  at the centre of the cavity BPM is  $\approx 340\text{nm}$  for an initial beam position of  $x_i = 10\mu\text{m}$ . This represents a 3.4% error in position which is typical for all of the ATF2 BPMs which are positioned immediately downstream of a quadrupole.

#### 5.4.2 Non-Mover Calibration

The beam position monitors in the extraction line (QD10X - QF21X, see figure 5.1) are fixed in transverse position (i.e. not mounted on movers) and so in order to calibrate these BPMs the beam was swept across the beampipe with the use of dipole corrector magnets. This was done by creating a bump in the beam as illustrated in figure 5.21. This local bump is created using four dipole corrector magnets to manipulate the beam into a flat trajectory (for

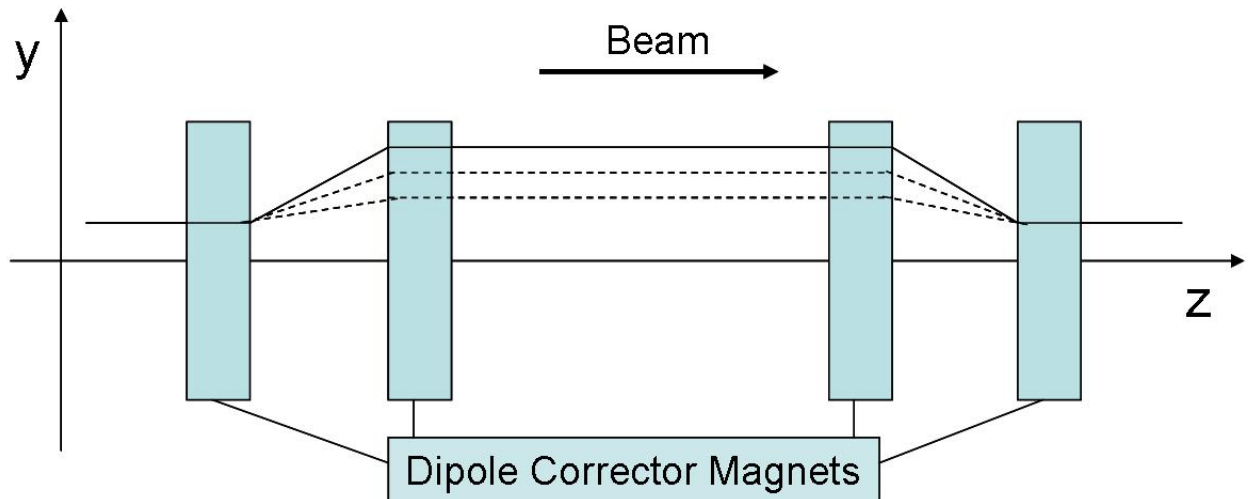


Figure 5.21: Diagram illustrating the method for creating a local bump.

a fixed distance) and their currents varied such that the beam moves transversely whilst still maintaining a flat trajectory. The bump was calculated using flight simulator software [113], an ATF2 optics and beam control tool.

Figure 5.22 shows the variation in beam position, as calculated from the bump optics, during the calibration procedure. The beam was moved in steps of  $250 \mu\text{m}$  over the range  $\pm 500 \mu\text{m}$ , recording data for ten electron bunches at each step. After determining the beam position from the bump the calibration is performed as it was in the mover calibration case (section 5.4.1). Figure 5.23 shows plots of  $I$  vs  $Q$  for both the  $x$  and  $y$  calibrations. Figure 5.24 shows variation of calculated beam position with  $I'$  and  $Q'$ . The calibration results for all nine (non-mover) cavity BPMs in the ATF2 extraction line are shown in table 5.3.

### 5.4.3 Scaling Factors

One of the desirable properties of the BPM system is to have identical BPMs. In this case the scaling factors should be identical in magnitude and since this is not the case the BPMs and their electronics must be different. This is due to slight differences in the cavities (seen in frequency variation reported in table 5.1) and the mixing electronics.

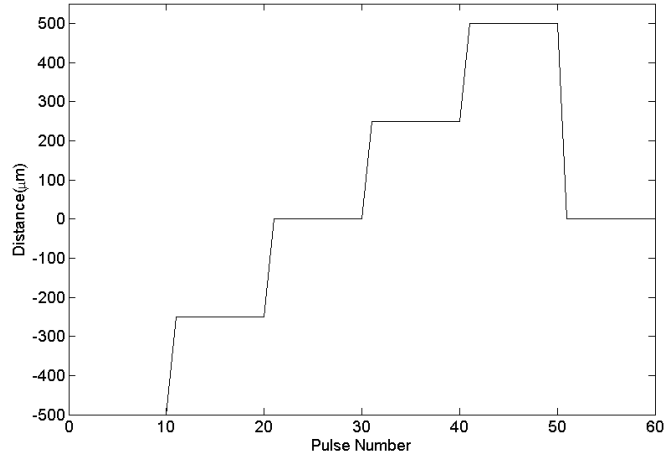


Figure 5.22: Beam position vs pulse number for a non-mover calibration.

BPM	$\theta_{x_{iq}}$ (rad)	$x$ -scale ( $\mu\text{m}$ )	$\theta_{y_{iq}}$ (rad)	$y$ -scale ( $\mu\text{m}$ )
QD10X	$0.492 \pm 0.002$	$547.6 \pm 3.8$	$1.209 \pm 0.004$	$-1130.0 \pm 46.8$
QF11X	$-1.416 \pm 0.001$	$-958.45 \pm 9.2$	$1.056 \pm 0.002$	$805.8 \pm 3.8$
QD12X	$-1.487 \pm 0.001$	$-694.4 \pm 3.9$	$-1.448 \pm 0.005$	$-941.2 \pm 9.4$
QD16X	$1.361 \pm 0.001$	$-695.2 \pm 2.1$	$0.749 \pm 0.002$	$-774.4 \pm 6.0$
QF17X	$-1.460 \pm 0.001$	$656.8 \pm 2.5$	$-1.539 \pm 0.004$	$501.7 \pm 5.1$
QD18X	$1.510 \pm 0.002$	$-674.2 \pm 3.1$	$-1.414 \pm 0.002$	$761.6 \pm 4.6$
QF19X	$0.696 \pm 0.004$	$-723.1 \pm 11.3$	$0.639 \pm 0.001$	$667.4 \pm 2.8$
QD20X	$0.715 \pm 0.001$	$666.1 \pm 4.7$	$0.398 \pm 0.002$	$-515.0 \pm 4.1$
QF21X	$-1.471 \pm 0.001$	$517.4 \pm 21.9$	$-1.403 \pm 0.001$	$431.7 \pm 2.3$

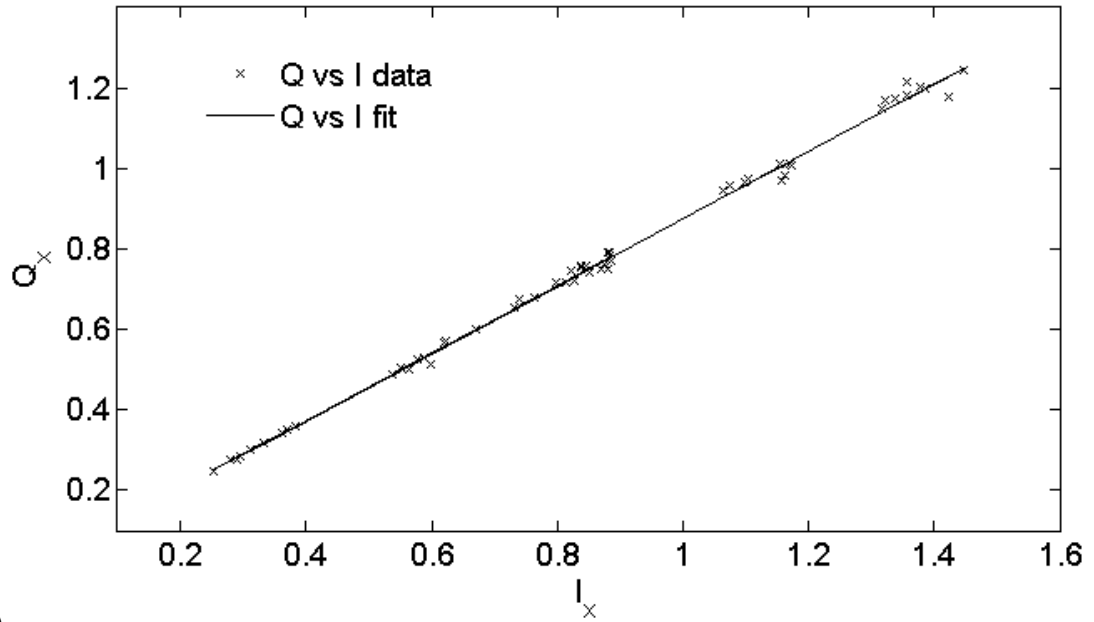
Table 5.3: Table of non-mover calibration results.

## 5.5 Problems and Solutions

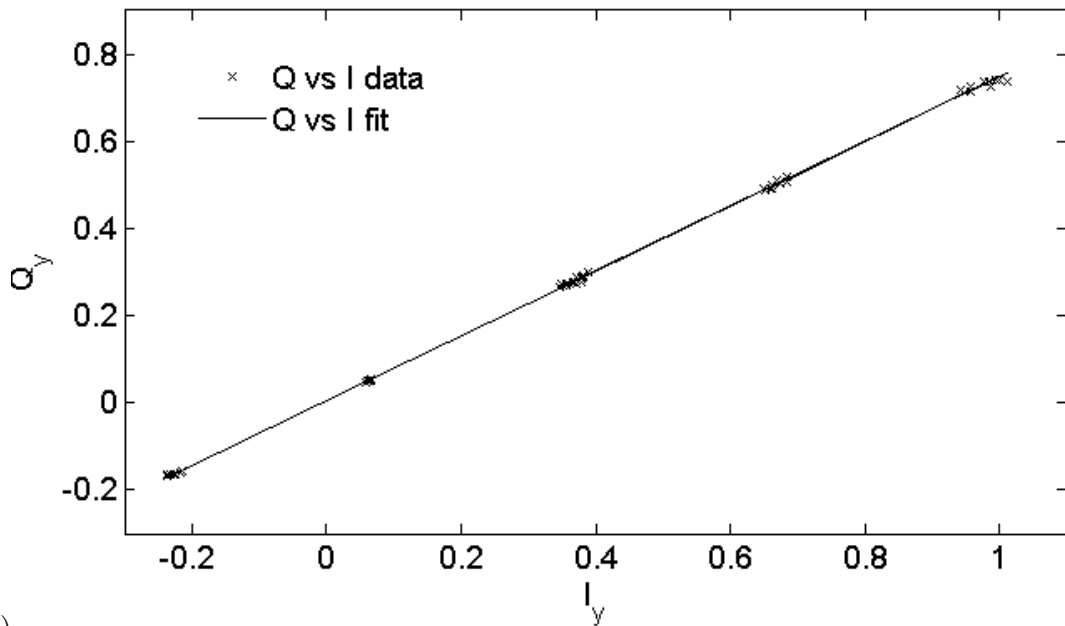
During commissioning of any new hardware system it is expected that various problems may arise. There follows an explanation of the two most significant problems and their solutions.

### Timing System and Signal Processing

Special attention must be paid to the synchronization of the data acquisition system (digitizers) with the beam in order to ensure data are recorded as the beam passes through the cavity and that the monopole signal used for charge normalization is used with the correct dipole signal. The layout of the timing system is shown in figure A.2 (Appendix A). Several problems arose during the commissioning of the timing system mostly due to clocks and



(a)



(b)

Figure 5.23:  $Q$  vs  $I$  plot for (a)  $x$ -plane and (b)  $y$ -plane of cavity BPM QF19X.

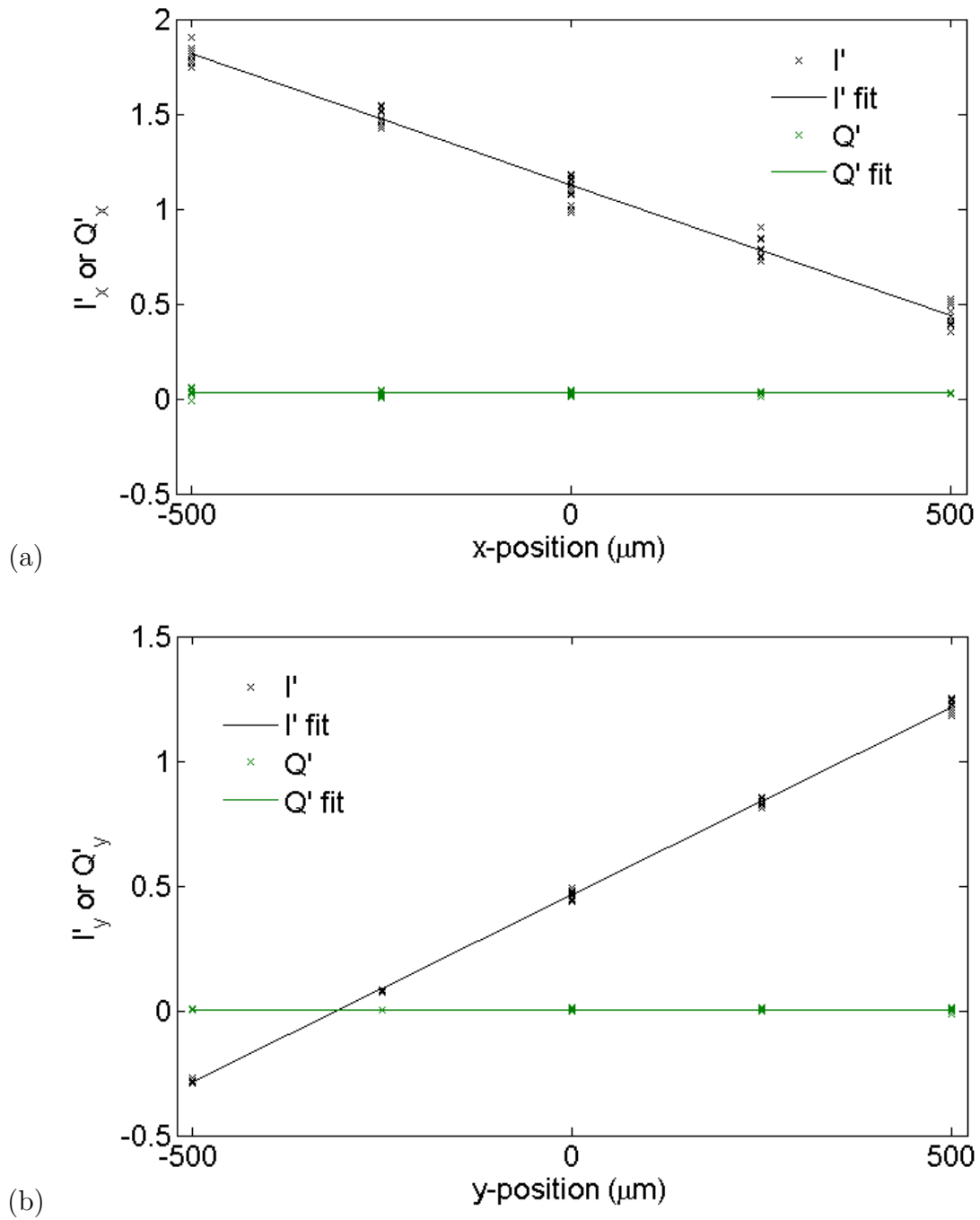


Figure 5.24:  $I'$  and  $Q'$  vs beam position plot for (a)  $x$ -plane and (b)  $y$ -plane cavity BPM QF19X.

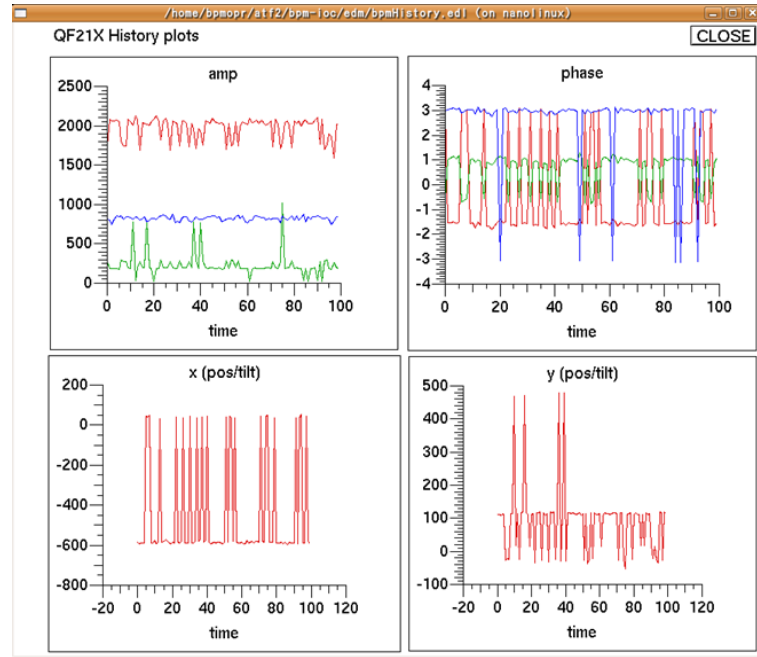


Figure 5.25: Screenshot illustrating cavity BPM phase problems. For the top two plots the red trace is the calculated  $x$  position, green the  $y$  and blue is the reference cavity monopole signal.

triggers jittering with respect to each other [114]. These were rectified by deriving these signals from the same source. Figure 5.25 shows the erratic behaviour of the BPM system that comes with such issues.

Figure 5.25 is a screenshot of the online cavity BPM analysis software. It shows the variation in amplitude, phase and calculated  $x$  and  $y$  beam position. Instability between the trigger and timing clock signals input to the SIS digitisers causes an apparent jump in phase (seen in the top right plot in figure 5.25). Since this phase is then used in the calculation of the beam position (see section 4.2.2) the position of the beam also seems to vary. This variation can be seen to be false since the amplitude of the cavity signal (seen in the top left plot in figure 5.25) has little variation.

One other significant problem came with the beam arrival time. Initially the DDC sample point (see section 4.2.2) was fixed in time at some point just after the peak of the digitized waveform. This method works perfectly well assuming the timing signals are unchanged, however since these signals are derived from the ATF2 master oscillator (in order to be locked to the beam) its condition may change (to account for problems seen in other ATF2

systems, many of which rely on these signals). This was rectified by the installation of a diode directly to a cavity output signal to measure the beam arrival time which then defined  $t_0$  (the beginning of the waveform produced by the bunch) and the DDC sample point was taken to be some number of time samples from this variable  $t_0$  as opposed to some fixed point.

### Reference Cavity Locations

The output from a dipole cavity BPM undergoes charge normalization (see chapter 4) using the output of a reference cavity and at ATF2 each dipole cavity uses the nearest downstream reference cavity (figure 5.1). It was seen that most often during calibration procedures the beam was sometimes kicked out of the beampipe when the mechanical mover (upon which one cavity and one focusing magnet were mounted), of the cavity undergoing the procedure, was moved to an extreme position (say 1mm from the central position). This meant that the beam did not reach the downstream reference cavity and so no monopole signal was produced and charge normalization was not performed, giving an incorrect position measurement or scaling factor (for occurrence during a calibration procedure). This issue was addressed through use of only the first two reference cavities, MREF1X and MREF3FF (see figure 5.1).

## 5.6 Stability and Dynamic Range

### Stability

In order to have working BPMs suitable for normal running of an accelerator there must be a high level of stability within the system. Table 5.4 shows five mover calibrations performed on QM13FF over a thirty six hour period and table 5.5 shows scale factors for BPM QM14FF for three different calibration procedures over several days. Both results show the scaling factors to be stable to within 10%.

Date	Time	$\theta_{y_{iq}}$ (rad)	$y$ -scale ( $\mu\text{m}$ )
08-12-2009	11:21:17	$-0.556 \pm 0.012$	$-572.9 \pm 3.49$
09-12-2009	06:18:18	$-0.552 \pm 0.007$	$-538.2 \pm 10.60$
09-12-2009	07:37:45	$0.335 \pm 0.009$	$-552.9 \pm 2.52$
09-12-2009	08:03:48	$-0.553 \pm 0.010$	$-550.1 \pm 2.26$
09-12-2009	22:43:03	$-0.586 \pm 0.004$	$-568.7 \pm 3.40$

Table 5.4: Results of calibration stability test of QM13FF recorded for the  $y$ -direction over a thirty six hour period. The variation from negative to positive value in  $\theta_{y_{iq}}$  is due to a  $\pi$  jump in phase.

Date	$x$ -scale ( $\mu\text{m}$ )	$y$ -scale ( $\mu\text{m}$ )
02-12-2009	$-41.6 \pm 1.30$	$-43.4 \pm 1.03$
04-12-2009	$-38.5 \pm 0.92$	$-42.9 \pm 0.47$
08-12-2009	$-46.1 \pm 1.34$	$-48.1 \pm 0.34$

Table 5.5: Calibration stability of QM14FF

## Dynamic Range

Figure 5.26 shows a calibration procedure performed over a range of  $\pm 1\text{mm}$  for QM13FF and it can be seen that the BPM output remains linear over the whole range. This range was in some cases seen to be the maximum range of the mover when it was at its extreme position in the direction perpendicular to that being measured, so in the case of the mover BPMs the BPM is not necessarily the limiting factor in dynamic range.

## 5.7 Summary

The first steps in setting up these BPMs for normal operation are waveform processing (DDC) and calibration. Two different methods of calibration were used; mover calibration (for those BPMs mounted on mechanical movers) and bump calibration (for those whose transverse position is fixed). During the DDC process the cavity frequency is determined which in turn leads to the determination of the quality factor.

Digital down conversion determines the in-phase ( $I$ ) and quadrature-phase ( $Q$ ) components of the BPM signal, which are both dependent on beam position. A simple rotation

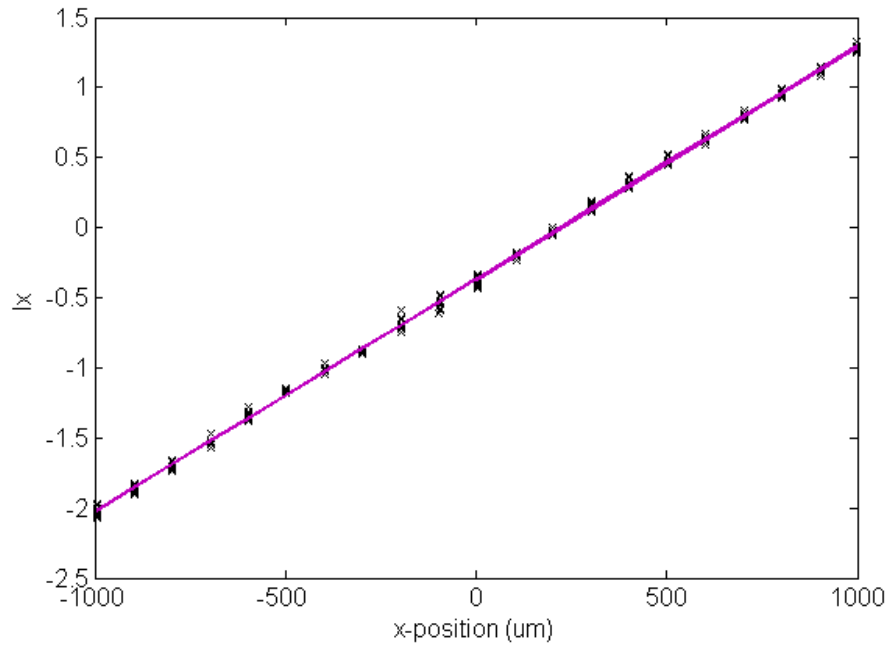


Figure 5.26:  $I'_x$  vs  $x$ -position for QM13FF over a range of  $\pm 1$ mm.

puts the entirety of the position dependence on one variable ( $I'$ ) and calibration determines the scaling factor of this linear dependence. Calibrations were performed for all 32 C-band cavity BPMs and the stability and dynamic range investigated. Two BPMs were used to investigate the reproducibility of the scaling factor and found to be stable to within 10%. The commissioning processes outlined in this chapter brought the cavity BPM system to a state suitable for normal accelerator running. Figure 5.27 shows a plot of the measured beam orbit throughout the BPM system, the red lines represent the  $x$ -position and the blue lines represent  $y$ . Such an orbit plot is used online during accelerator operation.

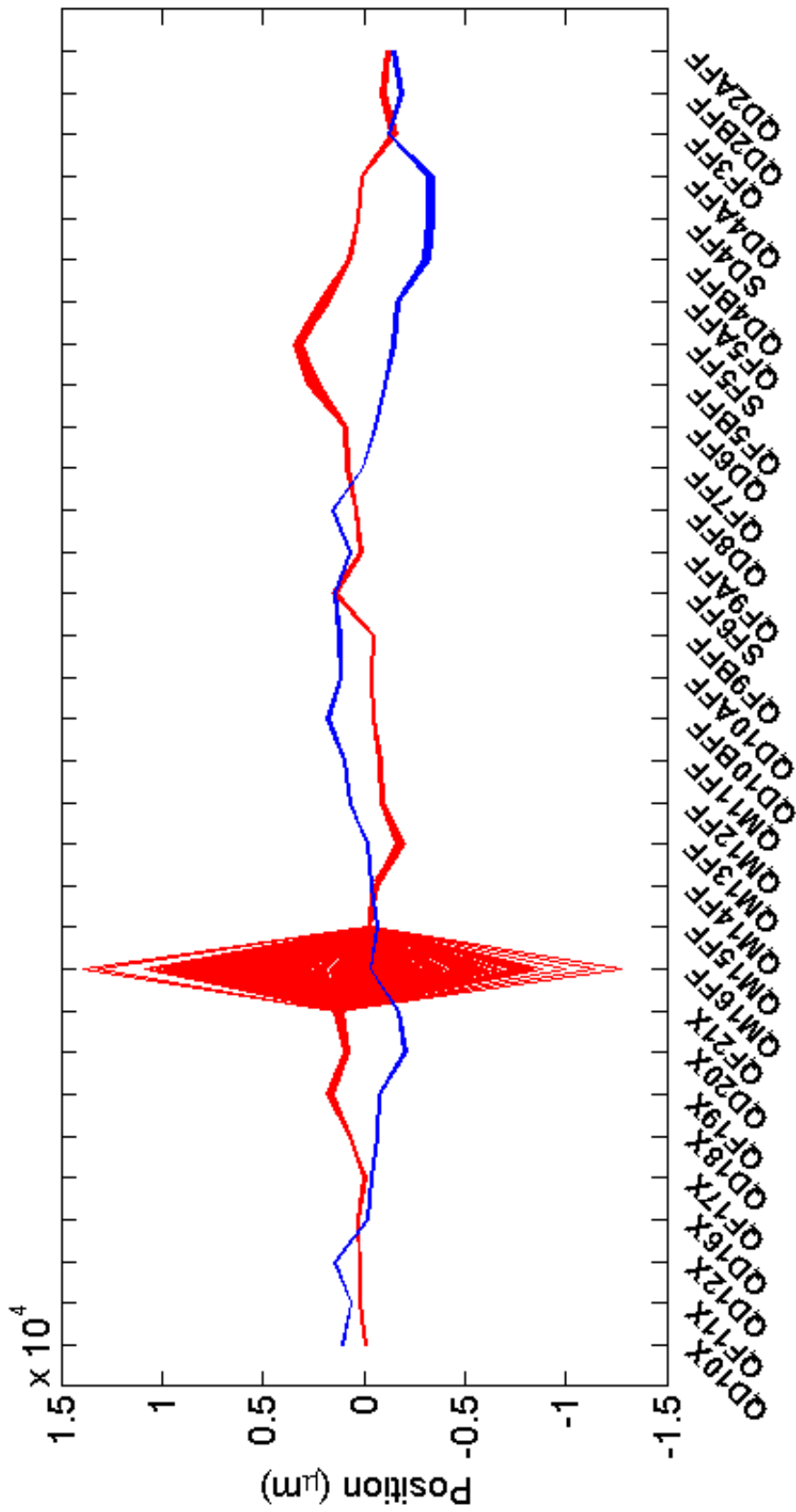


Figure 5.27: Beam orbit in the extraction line and final focus system of ATF2 plotted for 500 pulses. The red lines indicate the  $x$ -position whereas the blue lines show the  $y$ -position. The  $x$ -position at QM16FF is undefined since the calibration was unsuccessful (see section 5.4.1)

# Chapter 6

## Cavity BPM System Performance

In order to understand beam dynamics in an accelerator it is usual to develop a machine, or optics, model. Beam position measurements may then be fitted to this model and used to calculate other beam properties. Model Independent Analysis (MIA) describes methods by which beam properties may be determined without the use of an optics model. This chapter will outline a method by which the resolution of BPMs may be determined without consideration of transfer matrices (see chapter 3). There will then follow an investigation into the digital down conversion method of signal processing and a demonstration of the application of cavity BPMs in accelerators.

### 6.1 BPM Resolution Determination Using Model Independent Analysis

The most common way of determining BPM resolution is to use an accelerator optics model. Given initial beam parameters a model may be used to predict the position of the beam in a BPM and the resolution of the BPM is determined by the difference between this predicted position and the position as measured by the BPM (see section 3.4). There are two major issues with this method of determining resolution. One is the accuracy of the model (especially for large complex accelerators such as the ILC) and the second is the limiting effect of a given BPM's resolution (it was shown in section 3.4 that the resolution calculated by using the three BPM method is severely limited by BPM of poorest resolution). Given these

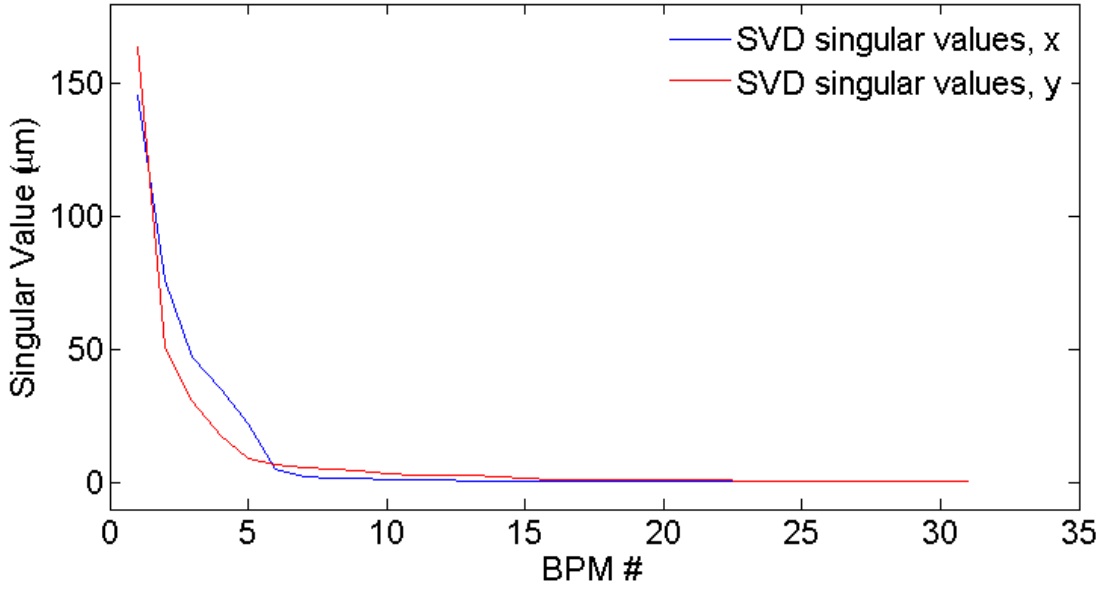


Figure 6.1: Singular values for SVD.

issues it is desirable to develop a method of determining resolution without the necessity of optics models. The high degree of correlation seen in BPM measurements [115] makes it possible to use Model Independent Analysis (MIA) to determine the resolution of a BPM system without knowledge of the accelerator optics model. Model independent analysis uses singular value decomposition (SVD) to remove the correlation between the BPMs to leave only noise, which is a measurement of the BPM resolution [116].

Position data were taken, immediately after the calibration procedure and simultaneously for all BPMs, for 500 beam pulses with a stationary beam and a matrix of measured beam positions constructed. The matrix,  $B$  of size  $P \times M$  (where  $M$  is the number of BPMs and  $P$  the number of pulses) contains the measured trajectory of each electron bunch.  $B$  may undergo Taylor expansion over all variables that the beam position depends on [117], as follows

$$\begin{aligned}
 b = & b(\bar{x}_1, \bar{x}'_1, \bar{\delta}, \bar{\sigma} \dots) + \sum_{\nu \in \{\bar{x}_1, \bar{x}'_1 \dots\}} \left. \frac{\partial b}{\partial \nu} \right|_{\nu = \bar{\nu}} \Delta \nu \\
 & + \frac{1}{2} \sum_{\nu_1, \nu_2 \in \{\bar{x}_1, \bar{x}'_1 \dots\}} \left. \frac{\partial^2 b}{\partial \nu_1 \partial \nu_2} \right|_{\nu_1 = \bar{\nu}_1, \nu_2 = \bar{\nu}_2} \Delta \nu_1 \Delta \nu_2 + \dots
 \end{aligned} \tag{6.1}$$

where  $\Delta\nu = \nu - \bar{\nu}$  and  $b$  is a row vector of  $B$ . Simplifying to give

$$b = b_0 + \sum_{s=1}^S \Delta\hat{q}_i^s \left[ \sigma_s \frac{\partial b}{\partial q^s} \right] + noise \quad (6.2)$$

where  $\hat{q}^s$  is normalized (to one over time, becoming dimensionless) and represents the  $s$ th physical variable. For example  $\hat{q}^s = \frac{\Delta\nu - \langle \Delta\nu \rangle}{\sigma_s}$ , where  $\sigma_s$  is the rms variation. In matrix form, this gives [117]

$$B_{P \times M} \equiv Q_{P \times d} F_{M \times d}^T + N \quad (6.3)$$

where  $N$  is a matrix containing the random noise present in each BPM,  $Q$  represents the temporal patterns of the pulses and  $F$  represents the spatial patterns ( $f = \sigma_s \frac{\partial b}{\partial q^s}$ ). The contributions of the physical variables  $q_s$  to the beam orbit may be obtained using singular value decomposition.

### 6.1.1 Singular Value Decomposition

Singular value decomposition gives [118]

$$B = USV^T \quad (6.4)$$

where  $U$  and  $V$  are orthogonal matrices representing the temporal and spatial components (eigenvectors), respectively, of the measured beam position and  $S$  is a diagonal matrix of non-zero singular values (eigenvalues). The eigenvalues indicate the significance of a given variable's contribution to beam motion. The smaller values arise from BPM noise and the largest from physical beam variations. Figure 6.1 shows a plot of the singular values and figure 6.2 shows the spatial and temporal components for the largest three singular values. The spatial eigenvectors for the second and third eigenvalues identify noisy BPMs (numbers 11 and 26, QM14FF and QD4BFF). The largest singular value is zeroed and the matrix  $B$  reconstructed into a matrix containing largely random noise. The resolution of each BPM is taken to be the rms variation of the beam position as given by the reconstructed matrix,  $B$ .

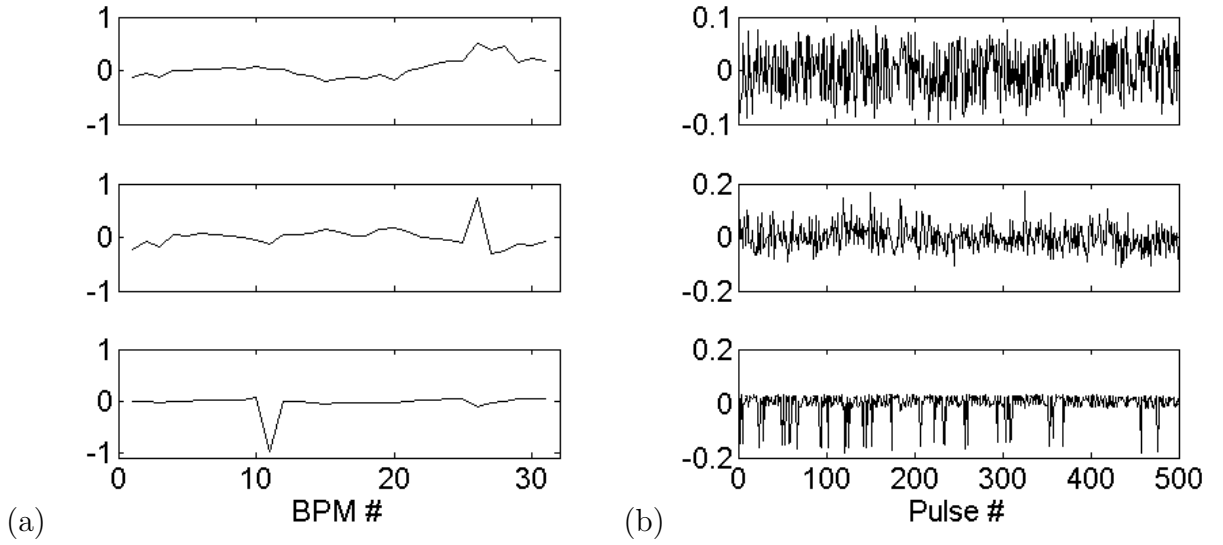


Figure 6.2: Normalized spatial (a) and temporal (b) eigenvectors of beam motion for the most significant three eigenvalues, determined via SVD. Results for BPM QD10AFF.

### 6.1.2 Results

Table 6.1 shows the calculated resolutions for each BPM.  $\sigma_{pos}$  is the rms variation of the measured position distribution and  $\sigma_{MIA}$  is the rms variation of the SVD output. Figure 6.3 shows an example of the determination of BPM resolution using the SVD method of model independent analysis; (a) shows the  $x$  and  $y$  plotted position for each pulse, (b) shows the same plot after the data have been processed, (c) shows the distribution of the measured beam position and (d) shows the distribution of  $x$  and  $y$  after MIA. Comparison of the resolution results calculated with and without the use of MIA shows that with MIA the resolution is significantly improved, taking the resolution from micron to nanometre level. The resolution results for all BPMs are plotted in figure 6.4

## 6.2 DDC Signal Processing

The digital down conversion process is dependent on two variables; the filter width,  $\Delta f$ , and the local oscillator frequency,  $\omega$  (see section 4.2.2 for DDC explanation). The LO frequency is calculated by flattening the phase plot and the filter width preallocated in the online processing software. What happens if these variables are incorrectly assigned?

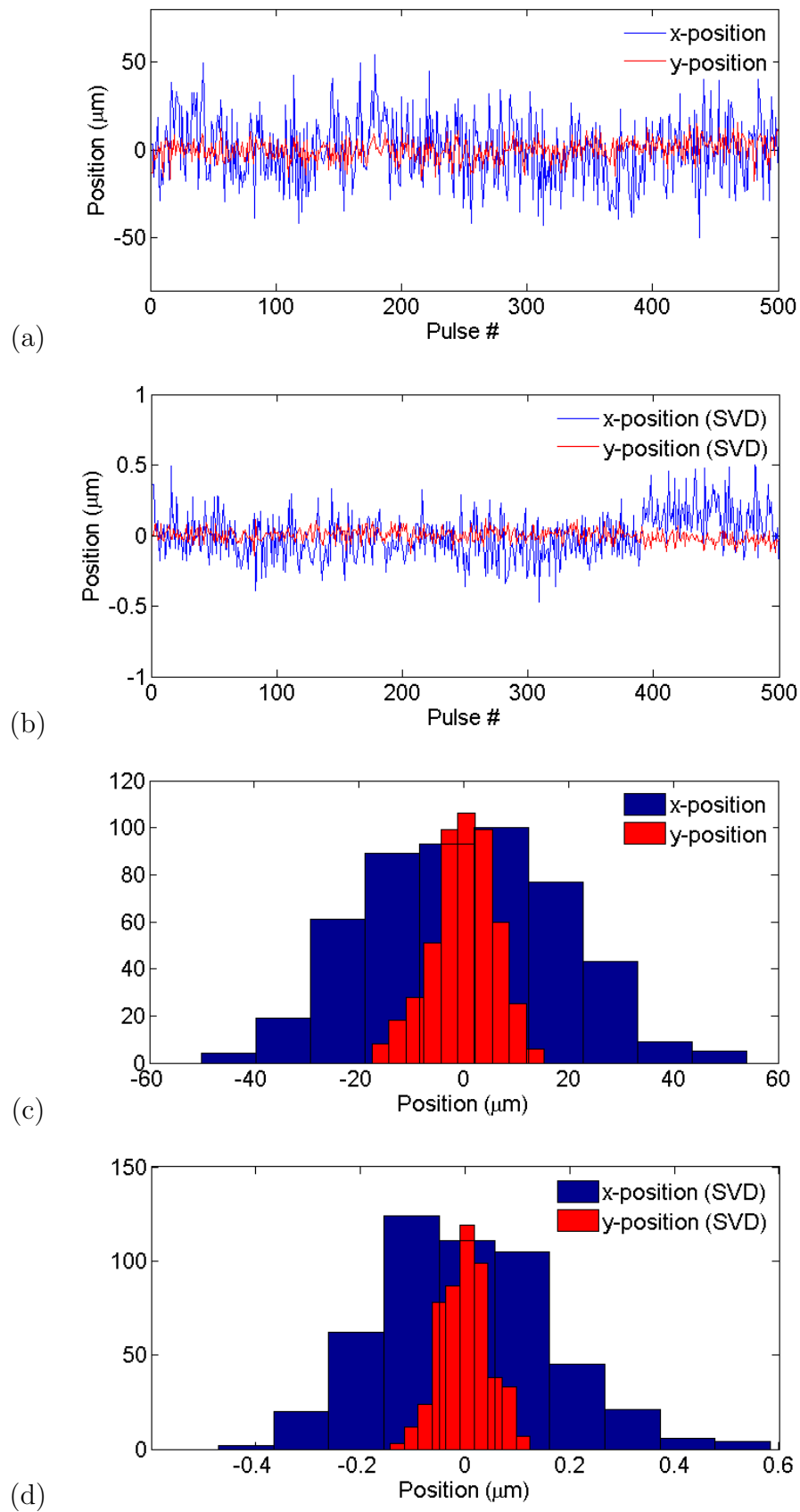


Figure 6.3: Beam position variation over 500 pulses, as measured by BPM QM15FF. (a), (c) show the measured beam position and (b), (d) show the beam position after MIA.

	BPM	$\sigma_{xpos}(\mu\text{m})$	$\sigma_{MIA}(\mu\text{m})$	$\sigma_{ypos}(\mu\text{m})$	$\sigma_{MIA}(\mu\text{m})$
1	QD10X	5.22	0.106	31.95	0.465
2	QF11X	23.92	0.273	9.83	0.143
3	QD12X	9.44	0.097	30.30	0.398
4	QD16X	9.77	0.247	3.50	0.116
5	QF17X	15.47	0.266	2.51	0.073
6	QD18X	15.06	0.066	9.72	0.195
7	QF19X	44.53	0.275	8.37	0.128
8	QD20X	18.19	0.238	14.00	0.118
9	QF21X	29.61	0.572	8.13	0.162
10	QM15FF	20.23	0.165	19.63	0.046
11	QM14FF	57.14	1.594	24.50	0.944
12	QM13FF	49.25	0.205	4.30	0.111
13	QM12FF	43.05	0.188	17.45	0.107
14	QM11FF	34.95	0.206	25.72	0.120
15	QD10BFF	15.94	0.240	44.74	0.307
16	QD10AFF	14.16	0.330	32.54	0.198
17	QF9BFF	23.76	0.591	30.84	0.085
18	SF6FF	39.44	0.760	36.00	0.101
19	QF9AFF	22.71	0.303	20.48	0.246
20	QD8FF	20.72	0.106	42.11	0.289
21	QF7FF	40.87	0.168	4.64	0.164
22	QD6FF	49.48	0.174	14.53	0.040
23	QF5BFF	127.39	0.484	27.34	0.075
24	SF5FF	115.9	0.568	39.03	0.120
25	QF5AFF	119.66	0.648	42.83	0.174
26	QD4BFF	39.74	0.318	115.32	1.220
27	SD4FF	27.16	0.394	89.32	0.542
28	QD4AFF	13.38	0.323	104.03	0.469
29	QF3FF	73.91	0.682	34.17	0.212
30	QD2BFF	41.41	0.588	50.22	0.306
31	QD2AFF	39.12	1.121	38.76	0.158

Table 6.1: Table of cavity BPM resolution results showing the rms variation of measured beam position ( $\sigma_x/\sigma_y$ ) and SVD results ( $\sigma_{MIA}$ ).



### 6.2.1 Optimization of Filter Width

The filtering process is performed in order to remove the upconverted component of the BPM signal, after LO mixing. If the filter is too wide this component of the waveform will not be removed and if it's too narrow too much signal will be removed, so reducing the resolution.

Figures 6.5 and 6.6 show the variation of amplitude, phase,  $I$ , scaling factor and  $I - Q$  rotation angle with filter width. It can be seen that all of these parameters vary significantly over a range of  $0.3 \text{ samples}^{-1}$ , in steps of 0.003, where the filter width for the data analysis in this thesis was chosen to be  $0.03^3$  in line with the online DDC signal processing. For this value the amplitude peak is large in magnitude whilst still being smooth (figure 6.5a). When the filter width is significantly narrower the amplitude of this signal is low and when it is wider the signal becomes noisy. The phase is also affected by filter width showing a nice flat signal for  $\Delta f = 0.03$ , but as the filter gets wider it becomes impossible to determine the phase (i.e the phase plot is no longer flat). This variation in amplitude and phase causes variation in  $I$  and therefore variation in scale (figure 6.6). If, as the filter width changes  $I$  and scaling factor change in the same manner then the resolution would remain unchanged. Figure 6.7 shows that this is not the case and so resolution is dependent on filter width.

### 6.2.2 Optimization of LO Frequency

The correct LO frequency is determined as that frequency which causes the phase plot to be flattened. This process may be done online (by eye). The effect of variation of frequency with DDC output will give an indication of the validity of this method of DDC frequency selection.

Figures 6.8 and 6.9 show the variation of amplitude, phase,  $I$ , scaling factor and  $I - Q$  rotation angle with DDC LO frequency. It can be seen that all of these parameters vary significantly over a range of  $0.2 \text{ samples}^{-1}$ , in steps of 0.002, where the DDC LO frequency for the data analysis in this thesis was chosen to be 0.2504 by flattening the phase plot.

---

<sup>3</sup>The frequency throughout has been given in units of  $\text{samples}^{-1}$ . The SIS digitizer cards were clocked at 100MHz giving a filter width of 3MHz and a sample time of 10 ns.

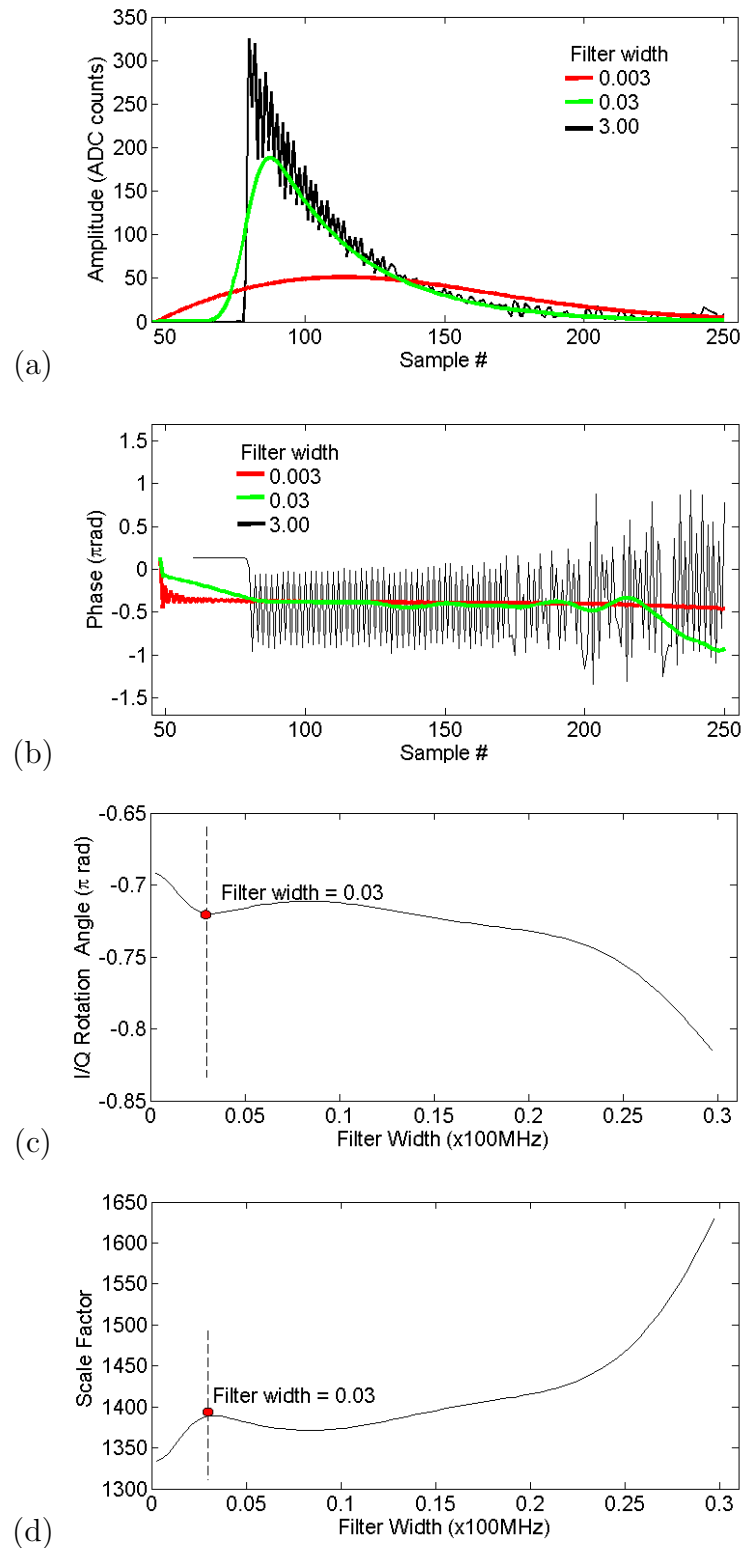


Figure 6.5: Variation of (a) amplitude, (b) phase, (c) I-Q rotation angle and (d) scale factor with filter width.

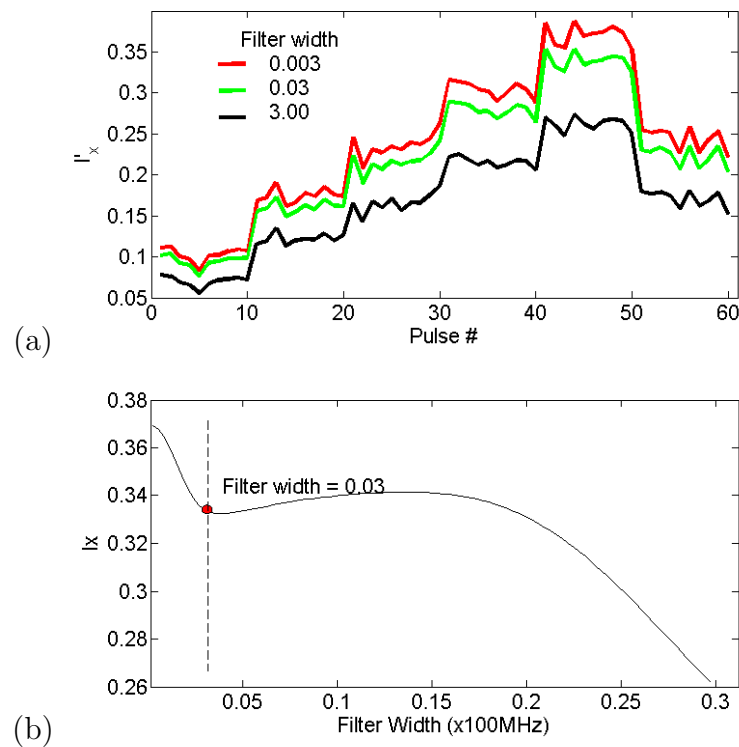


Figure 6.6: Variation of in-phase component of BPM signal with filter width.

For this value the amplitude peak is the largest value (figure 6.5a). When the DDC LO frequency is varied the peak of the amplitude plot has a much smaller value. The phase is also affected by DDC LO frequency showing a nice flat signal for  $\Delta f = 0.2504$ , but as the DDC LO frequency varies it becomes impossible to determine the phase (i.e the phase plot is no longer flat). This variation in amplitude and phase causes variation in  $I$  and therefore variation in scale (figure 6.9). If as the DDC LO frequency changes  $I$  and scaling factor in the same manner then the resolution would remain unchanged, figure 6.10 shows that this is not the case and so resolution is dependent on LO frequency.

### 6.3 Applications of Cavity BPMs

Knowledge of beam position is very important in accelerators not only to maintain a required beam orbit but it can also be used to determine other beam and accelerator properties by observing how the beam position varies under different conditions. One such measurement is that of dispersion.

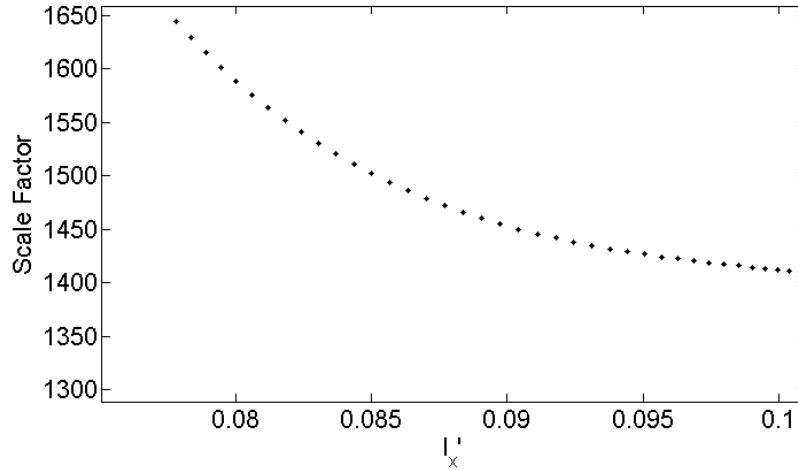


Figure 6.7:  $I$  vs scale factor for variable filter width.

### 6.3.1 Dispersion Measurement

Section 2.3 described the method by which beam dispersion may be determined. To recap

$$\Delta x(s) = D_x(s)\delta \quad (6.5)$$

$$\delta = -\frac{1}{\alpha - \gamma^{-2}} \frac{\Delta f}{f} \quad (6.6)$$

where  $\Delta x$  is the horizontal displacement of the beam,  $s$  is the position along the beamline,  $D_x(s)$  is the dispersion function,  $\delta$  is the relative momentum deviation of the beam,  $f$  is the RF frequency,  $\gamma$  is the Lorentz factor and  $\alpha$  is the momentum compaction factor (a difference in path length for a given relative momentum deviation [119] which is 0.002 in the case of ATF [120]). The constant  $\alpha$  is a property of circular accelerators. At ATF it is calculated for the damping ring, which precedes the extraction and final focus beamlines, and used to calculate the dispersion in these linear sections of the accelerator.

Since there are no RF cavities present in the extraction line or final focus system of ATF2 the RF frequency,  $f$ , was varied in the damping ring. Figure 6.11 shows the measured horizontal and vertical dispersion in each C-band<sup>4</sup> cavity BPM for  $\Delta f = 3$  KHz.

<sup>4</sup>C-band refers to the operating frequency of the BPMs, the C-band region of RF frequencies is commonly described, using the IEEE standard, to be between 4 and 8 GHz. In this case the operating frequency is 6.426 GHz

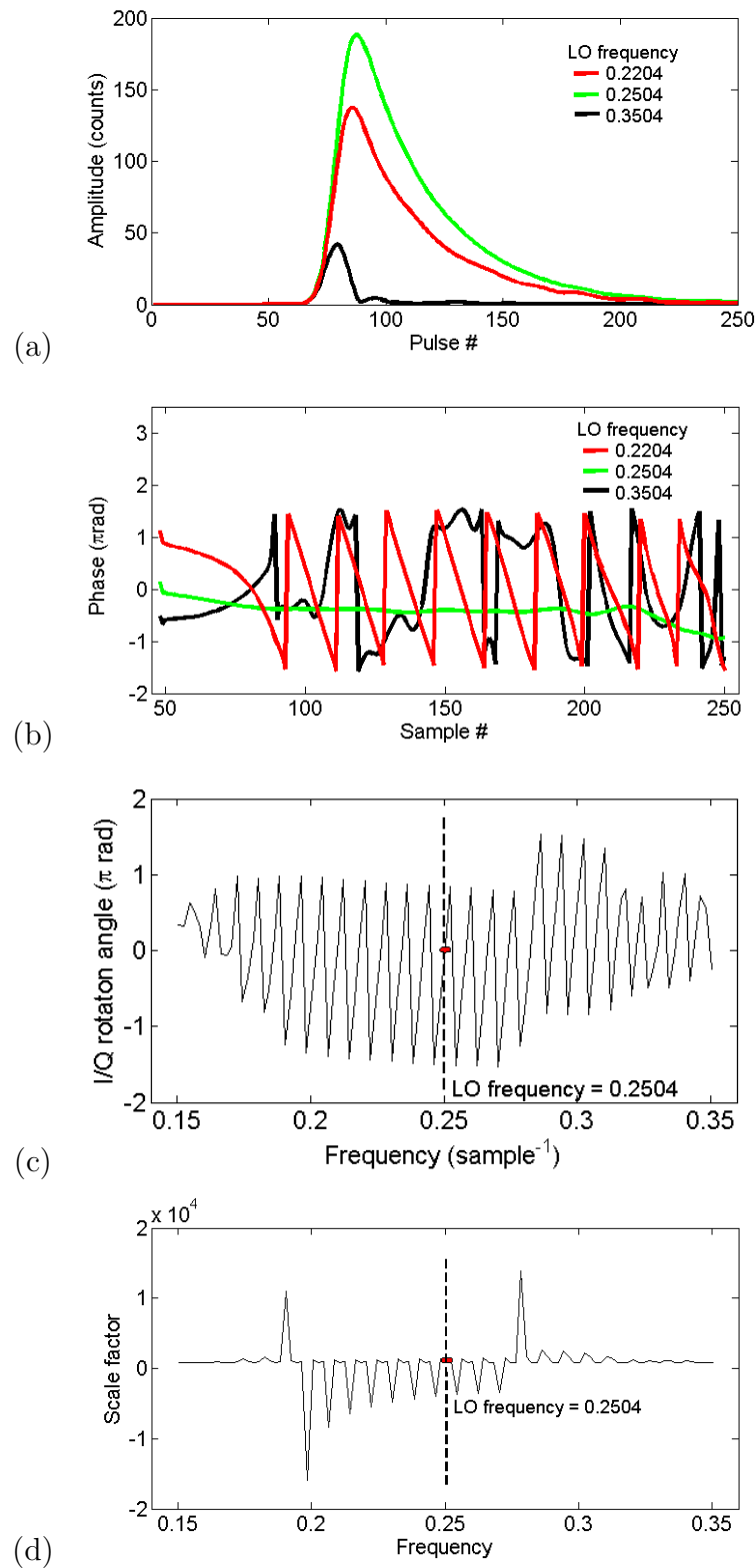


Figure 6.8: Variation of (a) amplitude, (b) phase, (c) I-Q rotation angle and (d) scale factor with DDC LO frequency. The sampling time of the digitizer is 10 ns per sample giving a frequency of  $1 \text{ sample}^{-1} = 100 \text{ MHz}$ .

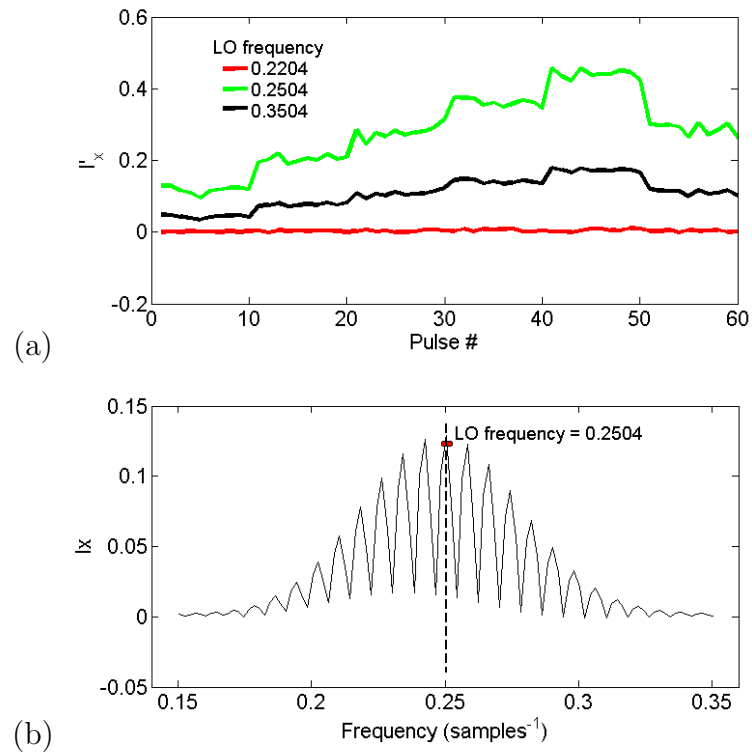


Figure 6.9: Variation of in-phase component of BPM signal with DDC LO frequency (for all pulses (a) and for a single pulse (b)). The sampling time of the digitizer is 10 ns per sample giving a frequency of  $1 \text{ sample}^{-1} = 100 \text{ MHz}$ .

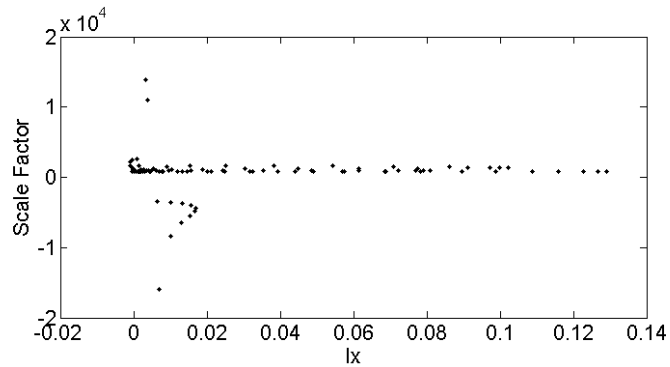


Figure 6.10: Scale factor vs  $I_x$  for variable DDC LO frequency.

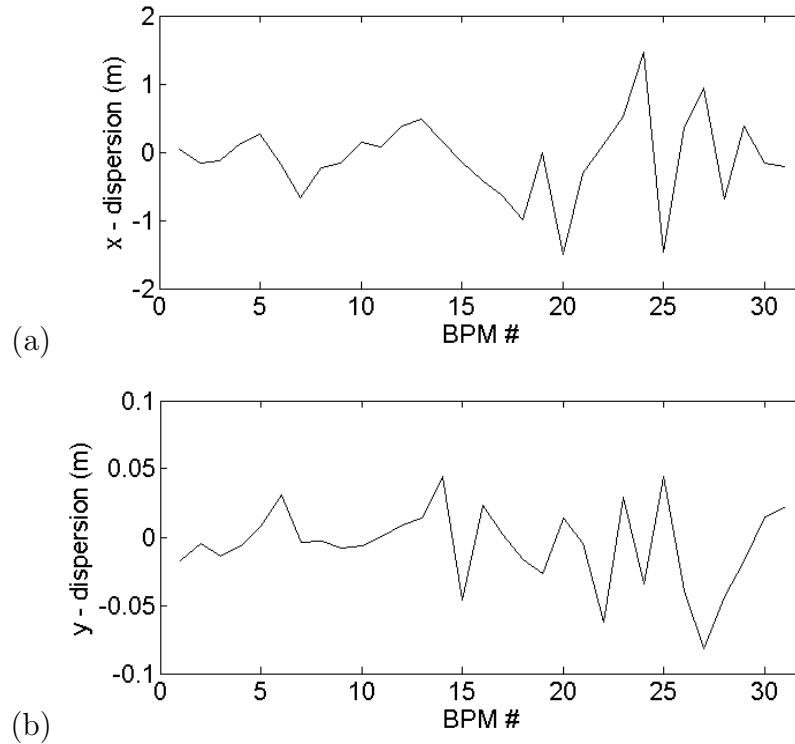


Figure 6.11: Horizontal (a) and vertical (b) dispersion measurements at each C-band BPM located in the ATF2 extraction line and final focus system.

## 6.4 Summary

The performance of the BPM system was assessed through measurement of the resolution of all 36 BPMs by use of model independent analysis. A simulation using real BPM data was performed to test the validity of the digital down conversion process. The DDC filter width and LO frequency were varied and found to have a significant effect on the scaling factor. Care must be taken to optimise these variables and they should be monitored regularly.

The cavity BPM system has achieved resolutions of  $<100$  nm with all achieving resolutions better than  $1 \mu\text{m}$ . BPM QM15FF has achieved a  $y$  - resolution of 46 nm, which is much better than the others due to lower attenuation of the cavity signals entering the electronics. The signals input to the mixing electronics for all BPMs, with the exception of QM14FF and QM15FF, were attenuated by 20 dBm increasing the noise level and reducing the resolution. It is expected that removal of the attenuation will increase the signal to noise ratio of the system to consistently reach the design resolution of 50 nm [116]. A final test of the system was to determine the dispersion at each of the BPMs with use of the momentum compaction

factor ( $\alpha$ ) as calculated in the damping ring (immediately preceding the extraction and final focus beamlines).

# Chapter 7

## Summary and Conclusions

Development and testing of a fast position feedback system has been demonstrated a success at ATF. Commissioning and testing of the beam position monitor section of the feedback system was performed, including calibration of the BPM and measurement of the position resolution. A second project, also for use in final focus systems, saw installation of a large array of high resolution cavity BPMs at ATF2. These BPMs were successfully calibrated and their properties investigated, including measurement of their resolution. The design resolution of 50 nm was achieved and the system is now being used during normal accelerator operation.

### 7.1 Feedback on Nanosecond Timescales

The future of particle physics is dependent on the development of accelerator technology where, alongside energy, collision luminosity is one of the most important considerations. Some of the major tools used in producing and maintaining high luminosity are beam feedback systems. A fast feedback system for correction of vertical beam position at the IP of a future linear collider has been demonstrated at both ATF and NLCTA. An investigation into the stripline BPMs used for vertical beam position measurement was performed showing 10 ns latency and better than  $5\mu m$  resolution.

### 7.1.1 Beam Position Monitor Studies

The FONT4 BPM processors use the difference-over-sum method for determining beam position. The difference and sum signals were output from the processors and the charge normalization done using the digital feedback board for the feedback BPM and offline in MATLAB for the two witness BPMs. All three BPMs were calibrated using corrector magnets and their calibration constants found to be close to the expected value ( $2.9 \text{ mm}^{-1}$ ) although not identical to each other. The resolution of the BPMs was determined to be  $4.5 \mu\text{m}$  using a geometric method which takes the difference between the beam position predicted by two of the BPMs and the position as measured by the third. This resolution was worse than the expected  $1\text{-}2 \mu\text{m}$  and further investigation showed that this may in part be due to differences in behaviour of each of the processors (the method of determining resolution makes the assumption that all BPMs and their electronics are identical, figure 3.17). The final results of the BPM analysis indicates that it is possible to achieve  $1 \mu\text{m}$  level resolution with the striplines and electronics (described in chapter 3) installed at ATF though special attention must be paid to data analysis methods and variation between processors. The BPMs used in the feedback system must be capable of consistently measuring beam position at the  $1 \mu\text{m}$  resolution level in order that the feedback system be viable for use at the ILC.

### 7.1.2 Past Achievements

The FONT project has passed through several stages beginning with FONT1 and FONT2 at NLCTA, both of which succeeded in demonstrated beam position feedback. FONT1 was a completely analogue system with  $66 \text{ ns}$  latency (plus  $5 \text{ ns}$  for the BPM processor) which achieved a  $10\text{:}1$  position correction [49]. The second generation feedback system achieved a  $14\text{:}1$  position correction, a latency of  $55 \text{ ns}$  (plus  $18 \text{ ns}$  for the BPM processor) and included several major changes; two additional BPMs were introduced (FONT1 had only a single BPM) and used to determine the resolution of the feedback BPM ( $15 \mu\text{m}$  achieved), the distance between kicker and BPM was reduced in order to reduce the latency, the BPM processor was redesigned to allow online charge normalization and a beam flattener was

added. For the third generation of FONT the move was made to ATF where the bunch spacing is 2.8 ns as opposed to the 88 ps at NLCTA. FONT3 achieved a 23:1 correction ratio with 23 ns latency and a BPM resolution of 15  $\mu\text{m}$  (without charge normalization to reduce latency). FONT4 saw the introduction of digital feedback electronics for increased accuracy but with the cost of increased latency. This decision was taken along side the decision to shift the concentration of the project from "warm" to "cold" (with larger bunch spacing) machines such as the ILC. FONT4 operated on a three bunch beam with a spacing of 154ns.

### 7.1.3 Future Goals

Development of the FONT feedback system is ongoing at ATF2 with the recent installation of a second kicker for angle correction,  $y'$ . The short term goal of the FONT project (FONT5) is to fully commission the newly developed feedback electronics and BPM processors. A single board has been developed to acquire data from the BPM processors with higher resolution ADCs and using this information to perform bunch by bunch feedback in both  $y$  and  $y'$ . It is hoped that the feedback system will be of use in normal accelerator running at ATF2 to stabilize the beam by reducing bunch to bunch jitter. A longer term goal of the FONT project is to develop a feedback system suitable for use at CLIC (Compact Linear Collider), which is a proposed future linear collider [121]. Development of a feedback system for a machine such as CLIC will present new challenges to the FONT group due to a shorter bunch spacing (0.5ns for CLIC as opposed to 337ns for ILC) than would be found in a super conducting accelerator.

## 7.2 Cavity BPM

Beam position monitors are an important and necessary part of any particle accelerator. They are invaluable in determining beam and accelerator properties, for example; beam size, dispersion and emittance from which Twiss parameters and therefore accelerator parameters and beam orbit may be determined. The achievement of nano-metre beam sizes demands

very high resolution BPMs which is important since higher resolution allows more accurate position measurement therefore reducing the uncertainty of any calculated property which varies with beam position.

32 C - band cavity BPMs were installed throughout the extraction line and final focus systems of ATF2, 23 of which (those in the final focus system) were mounted on mechanical movers. The outputs (decaying sine wave, see section 4.2.2) of the BPMs were input to signal processing electronics and the output recorded using digitizer based data acquisition (see section 5.1). These data were then processed in software by digital down conversion to give a single value for the position of each bunch (in ADC counts). The entire system was then calibrated to allow conversion of position in counts to position in microns. The extraction line BPMs (without movers) were calibrated by creation of a beam orbit bump which was varied to move the beam in a transverse direction across the beampipe. The final focus BPMs were calibrated by moving the BPMs, using mechanical movers, instead of moving the beam. The BPM system is now completely commissioned for normal accelerator operation.

After the installation and calibration at ATF2 the cavity BPMs were investigated to determine their properties, the most important being the resolution. Data were recorded for all BPMs simultaneously, with a static beam and movers in fixed positions, to measure the position of each bunch in each BPM. This data was then processed using model independent analysis to determine the resolution without requiring knowledge of the  $R$  - matrices (accelerator model). This method of resolution determination is ideal in the case of this BPM system (it was not suited to the FONT BPMs) due to the availability of a large array of BPMs. MIA works by removal of high correlation in the BPM data (see section 6.1) leaving only the noise, where the rms variation of this is taken to be the resolution. Resolutions of  $<100$  nm have been achieved in some cases and are better than  $1 \mu\text{m}$  in most cases. The BPM output signals were attenuated by 20 dBm, thereby increasing the noise level and reducing the resolution. It is expected that much improved resolution will be seen when this attenuation is removed and the design resolution ( $50\mu\text{m}$ ) consistently achieved.

### 7.2.1 Future Work for Cavity BPM

Four S-band (where S-band refers to the operating frequency of the BPMs. The S-band region of RF frequencies is commonly described, using the IEEE standard, to be between 2 and 4 GHz where the BPMs in this system operate at 2.9 GHz) cavity BPMs have also been installed in the final focus beamline at ATF2. They have been positioned towards the down stream end of the beamline in the area of the final doublet. The requirement for use of S-band over C-band BPMs arises from the condition that the aperture of the BPMs is designed to be twice as large as that required further upstream in the beamline. This is due to the large size of the beam as it enters the final doublet to be squeezed down to its ideal nanometre size (see section 1.1.3 for this method of producing nanometre sized particle beams). These BPMs have recently been commissioned and are currently undergoing tests.

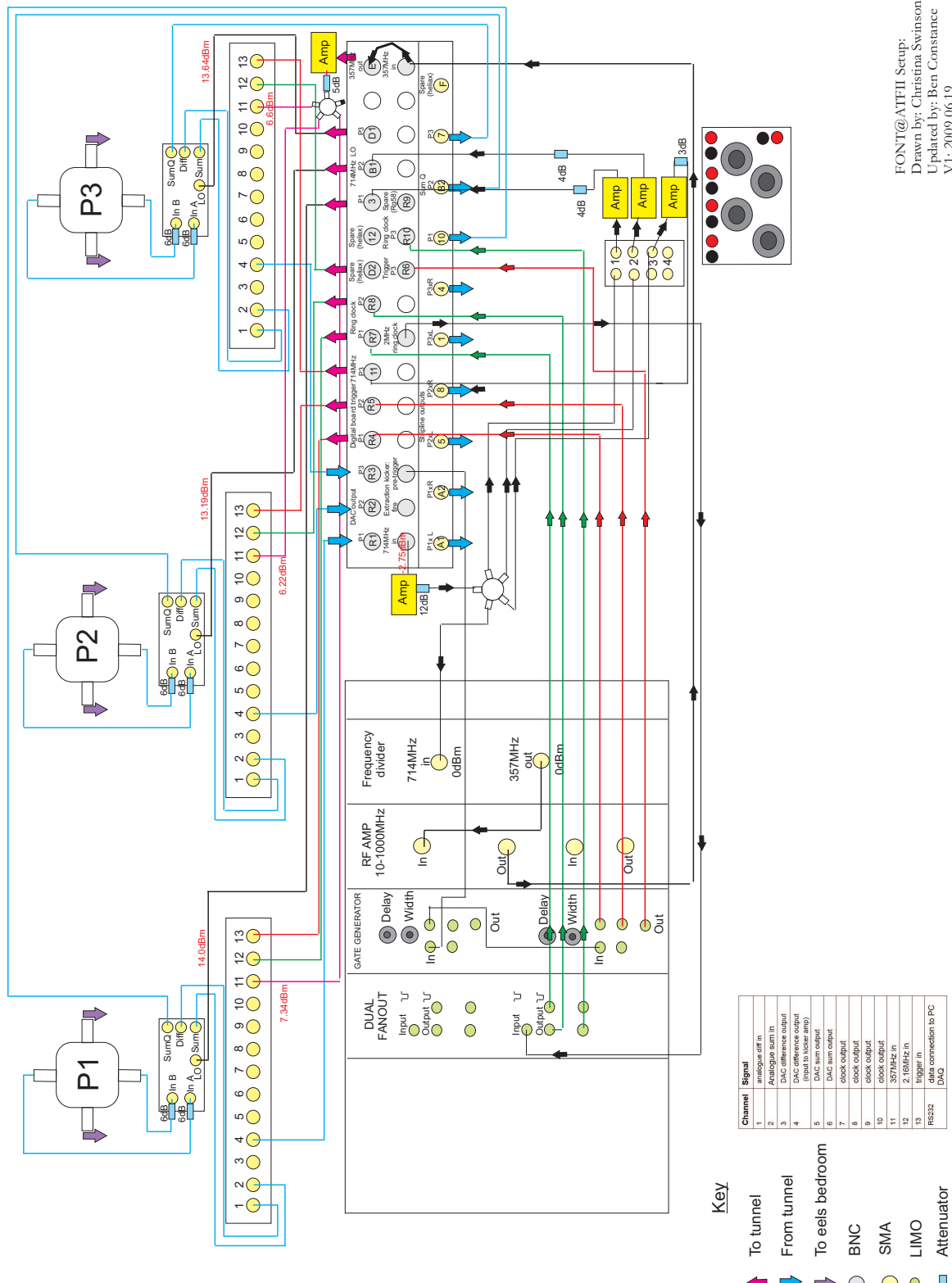
# Appendix A

## Hardware Methods and Schematics

A.1 Layout of the FONT Cable Plant at ATF2

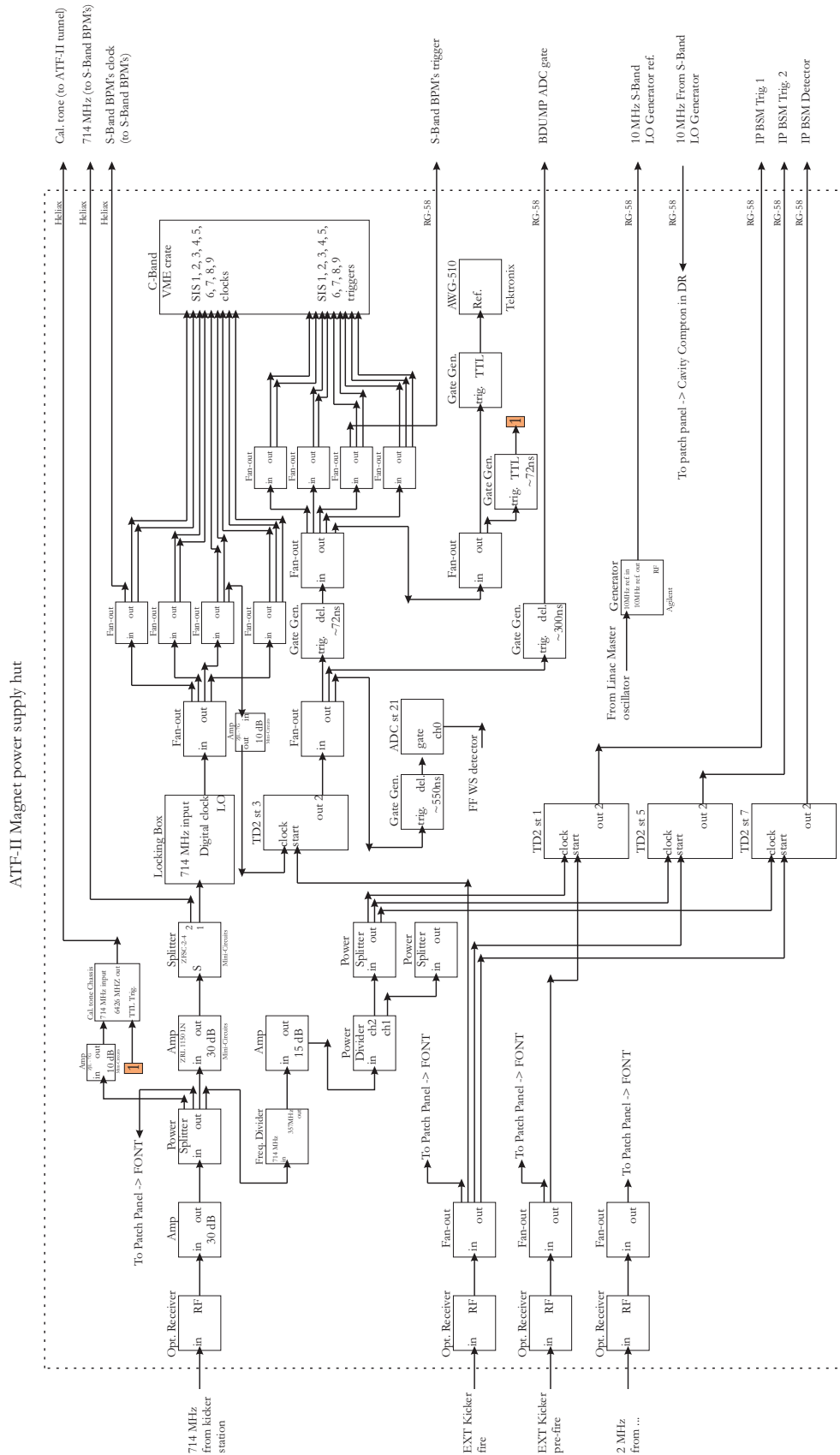
A.2 Layout of Cavity BPM Timing System

A.3 Layout of Cavity BPM LO and Caltone Distribution Systems



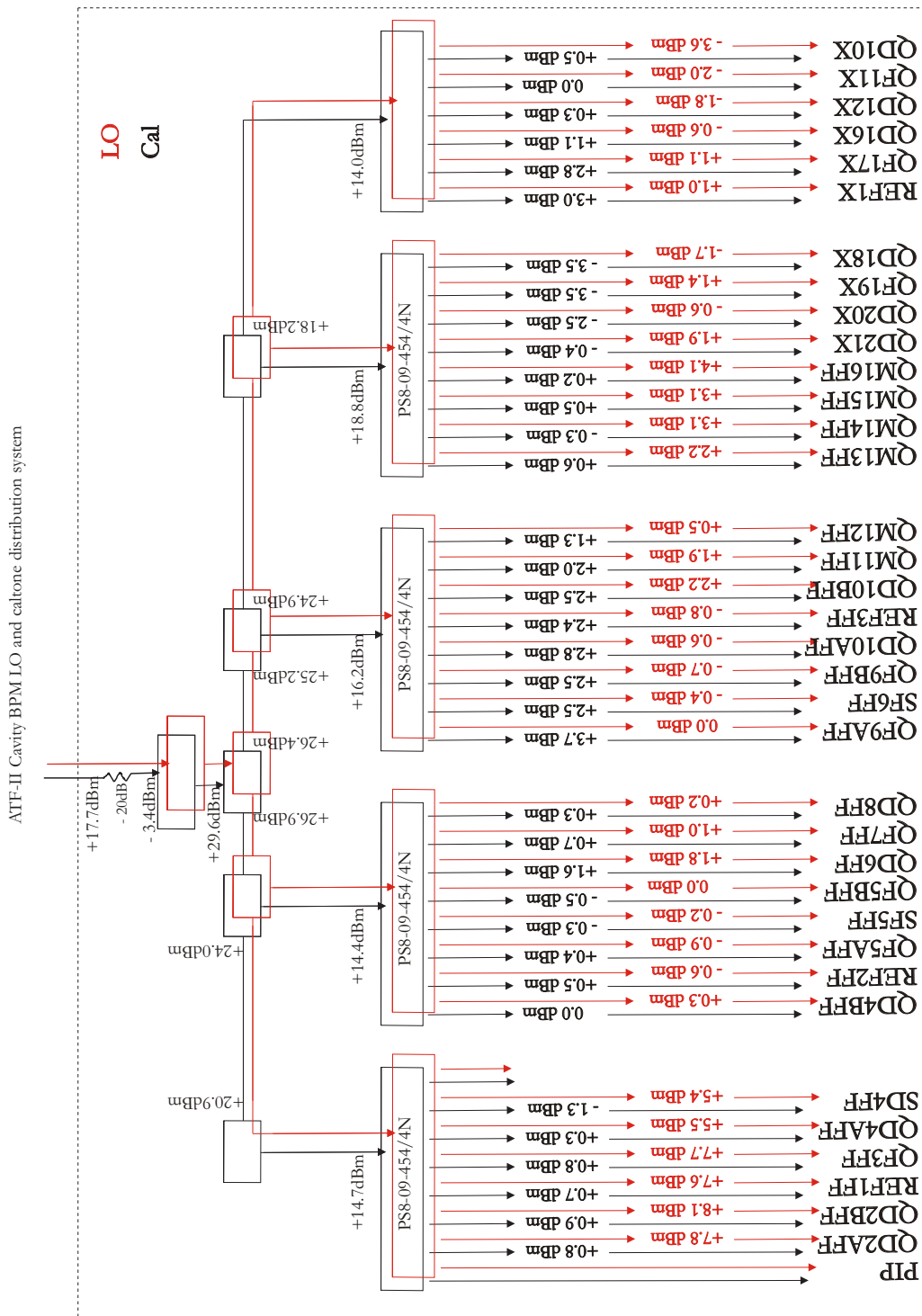
FONT@ATFII Setup:  
 Drawn by: Christina Swinson  
 Updated by: Ben Constance  
 V1: 2009.06.19

Figure A.1: Layout of the FONT cable plant at ATF2 [122].



ATF-II timing diagram: "ATF-II Magnet power supply hut"  
 Drawn by: Aryshev Alexander  
 28.05.2009

Figure A.2: Diagram of the cavity BPM timing system located in the power supply room at ATF2 [123].



ATF-II Cavity BPM LO and Cal distribution system V1  
 Drawn by: C. Swinson  
 30.04.2009

Figure A.3: Diagram of the cavity BPM LO and caltone distribution systems. The 6.446GHz local oscillator is distributed to each set of mixing electronics along with the calibration tone signal.

## A.4 Cavity Frequency - Offline Measurements

Section 5.3.1 describes a method by which the cavity frequency may be determined using information from the beam. It is also possible to determine this frequency offline using a network analyzer. Figures A.4 and A.5 show an example of a network analyzer measurement performed on a dipole cavity. Two of the four couplers are used in these measurements; a signal is input to one channel and the output from another channel measured. Figure A.4 shows the reflection measurement where the frequency of the input signal is varied, and the output measured from the same channel. The peak at 6.424 GHz is the frequency of the dipole mode. No peak is seen at the monopole mode frequency indicating that the cavity has been successfully designed such that this mode is suppressed. The width of the dipole peak gives a measurement of the  $Q$  value. Figure A.5 shows, for the same input, the output from the channel adjacent cavity channel (i.e input to  $x$  and output from  $y$ ). The lack of peak at the dipole frequency confirms that there is no cross coupling present so a movement in one direction will not affect the output in the other direction. All hardware measurements in table 5.1 were performed by Y. Honda [112], of KEK, prior to the installation of the cavities in the beamline.

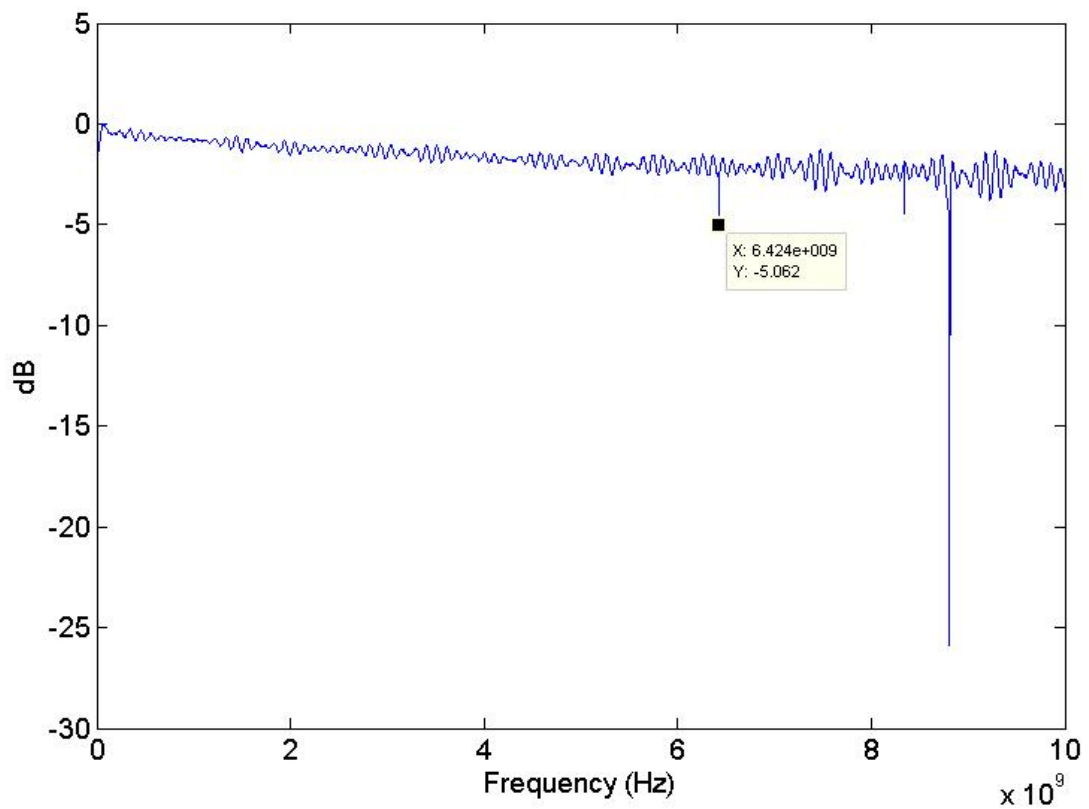


Figure A.4: Plot of cavity BPM network analyzer measurements showing the reflection measurement,  $s_{11}$  (measurement of variation of the BPM output for the same channel as the input)

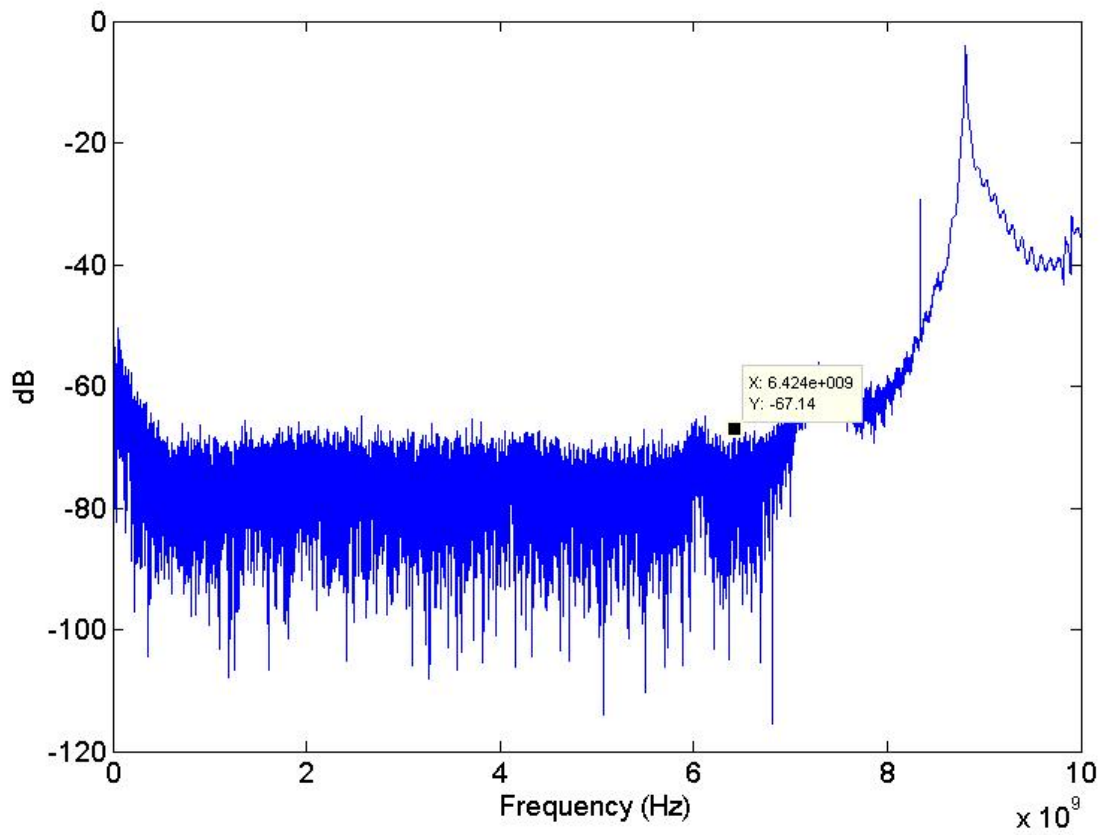


Figure A.5: Plot of cavity BPM network analyzer measurements, s12 (signal input to one channel and output measured from the adjacent channel, i.e input for  $x$  channel and output for  $y$  channel)

# Appendix B

## Mathematical and Computing Functions

### B.1 Bessel Functions of the First Kind

The functions  $J_m$  are known as Bessel functions of the first kind and are a set of solutions to the Bessel differential equation, defined as follows [124]

$$z^2 \frac{d^2 u}{dz^2} + z \frac{du}{dz} + (z^2 - m^2)u = 0 \quad (\text{B.1})$$

and  $J_m$  is defined as

$$J_m(z) = \left(\frac{z}{2}\right)^m \sum_{k=0}^{\infty} \frac{\left(-\frac{z^2}{4}\right)^k}{k! \Gamma(m+k+1)} \quad (\text{B.2})$$

where  $\Gamma$  is the gamma factor ( $\Gamma(n) = (n-1)!$ ) Figure B.1 is a plot of  $J_m$ , where  $m = 0, 1, 2 \dots 5$ , created using the MATLAB function `bessel[m,z]` which performs the calculation of equation B.2 on a given data set,  $z$ .

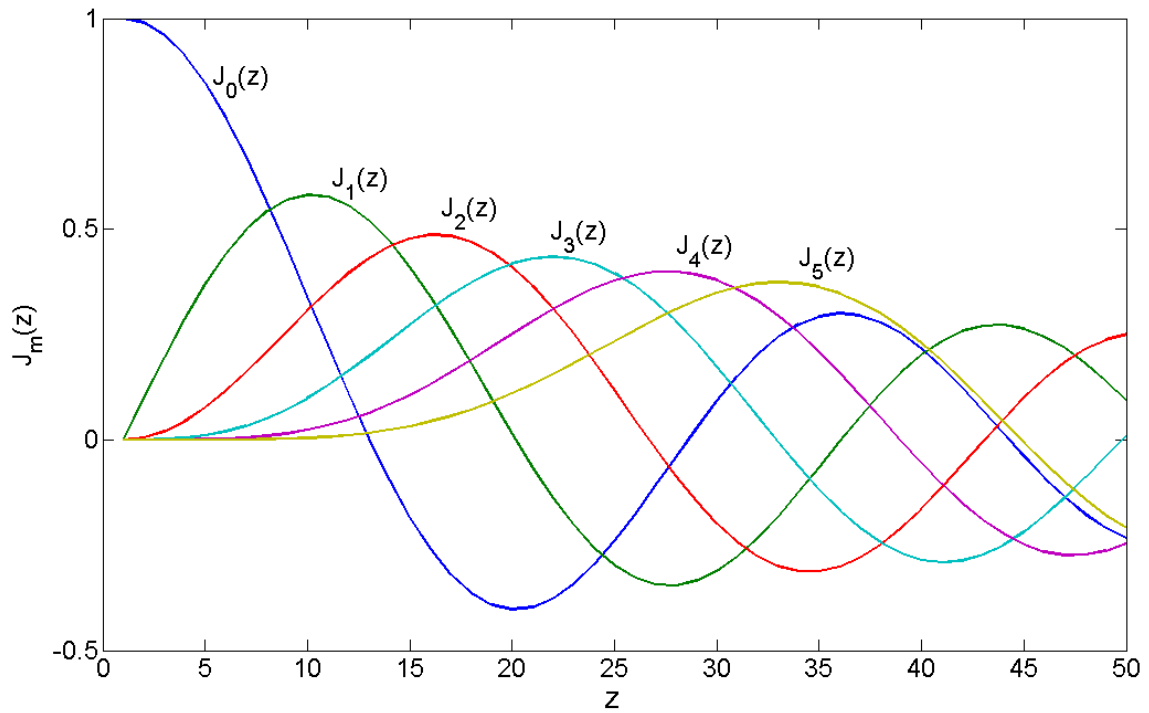


Figure B.1: Plot of Bessel functions of the first kind,  $J_m$ , where  $m = 0, 1, 2 \dots 5$

## B.2 filter[b,a]

The MATLAB filter function

```
y = filter (B, A, x)
```

filters the data  $x$  using a digital filter defined by  $A$  and  $B$  [125]. The function is defined as follows [126]

$$y(n) = \sum_{i=0}^{M_n} b_i x(n-i) - \sum_{j=1}^{N_n} a_j y(n-j), \quad i = 0, 1, \dots, M \quad j = 1, 2, \dots, N$$

(B.4)

where  $A$  and  $B$  are vectors containing the elements  $a_j$  and  $b_i$  of feedback and feedforward coefficients respectively [127].

# Bibliography

- [1] <http://www.slac.stanford.edu>. “The Linac and the SLAC Linear Collider”.
- [2] <http://www.linearcollider.org/cms/>.
- [3] P. N. Burrows & the Gateway to the Quantum Universe committee. “The international Linear Collider - Gateway to the Quantum Universe” (2007).
- [4] Nobukazu Toge Nan Phinney & Nicholas Walker (Editors). “International Linear Collider Reference Design Report. Volume 3: Accelerator”. ILC Global Design Effort (2007).
- [5] H. Weidemann. “Synchrotron Radiation”. Springer (2003).
- [6] C. R. Prior. “The Physics of Accelerators”. CERN Accelerator School (October 2000).
- [7] Roberto Aloisio & Pasquale Blasi. *Astropart. Phys.*, **18** (2002) 195–203.
- [8] Peter W. Higgs. *Int. J. Mod. Phys.*, **A17S1** (2002) 86–88.
- [9] D. Miller. “Lectures in Particle Physics: Politics, Solid State and the Higgs”. Department of Physics and Astronomy, University College, London, UK (2006). <http://www.phy.uct.ac.za/courses/phy400w/particle/higgs3.htm>
- [10] G. Moortgat-Pick. “The role of polarized positrons and electrons in revealing fundamental interactions at the Linear Collider”. CERN-PH-TH/2005-036 (2005).
- [11] D. Binosi & L. Theu. “JaxoDraw: A graphical user interface for drawing Feynman diagrams”. Computer Physics Communications, Volume 161, Issues 1-2, Pages 76-86 (2004).
- [12] A. Djouadi. “SUSY@ILC (talk)”. Galileo Galilei Institute for Theoretical Physics, Arcteri, Florence (2007). <http://www.ggi.fi.infn.it/talks/talk472.pdf>
- [13] “The Official String Theory Website: Supersymmetry to the rescue?” <http://pdg.web.cern.ch/pdg/cpep/supersymmetry.html>
- [14] Particle Data Group. “The Particle Adventure” (1999). <http://superstringtheory.com/experm/exper4.html>

- [15] Chris Miller. “Cosmic Hide and Seek: the Search for the Missing Mass” (1995). <http://www.eclipse.net/~cmmiller/DM>
- [16] Manuel Drees et al. *Phys. Rev.*, **D63** (2001) 035008.
- [17] G. Ganis J. Ellis & K. Olive. “Supersymmetric Dark Matter and the Energy of a Linear Electron-Positron Collider”. CERN-TH/99-386 (1999).
- [18] C. Amsler *et al.* “The Review of Particle Physics”. Particle Data Group (2008).
- [19] S. Heinemeyer. “Why Do We Need a Top Mass Measurement with ILC Precision?” LCWS05. [http://www.slac.stanford.edu/econf/C050318/talks/0401\\\_TALK.PDF](http://www.slac.stanford.edu/econf/C050318/talks/0401\_TALK.PDF)
- [20] Zack Sullivan. “Top Quark Physics at the ILC: Methods and Meanings”. arXiv:0903.1143v1 [hep-ph] (2008).
- [21] Barry Barish. “ILC: Technologies and Concept (lecture)”. Fourth International Accelerator School for Linear Colliders (September 2009). <http://ilcagenda.linearcollider.org/conferenceTimeTable.py?confId=3475>
- [22] Wanming Liu & Wei Gai. “Systematic Study of Undulator Based ILC Positron Source: Production and Capture”. PAC07 Conf. Proc. pp2921.
- [23] A. Wolski. “An Introduction to the ILC Damping Rings (part of the John Adams Institute Lecture Series)” (2006). [www.adams-institute.ac.uk/lecture\\\_series\\\_2007.php](http://www.adams-institute.ac.uk/lecture\_series\_2007.php)
- [24] E. J. N. Wilson. “An introduction to particle accelerators”. Oxford University Press (2001).
- [25] “ILC wiki”. <http://www.linearcollider.org/wiki/doku.php>
- [26] K. Ranjan. “ILC Main Linac Simulation”. ILC Meeting, Fermilab (March 2006). [http://ilc-dms.fnal.gov/Members/kirti/Mar\\_2906\\_talk/folder\\_contents](http://ilc-dms.fnal.gov/Members/kirti/Mar_2906_talk/folder_contents)
- [27] A. Seryi. “The ILC Beam Delivery System Conceptual Design and R&D Plans”. Proceedings of 2005 Particle Accelerator Conference, Knoxville, Tennessee (2005).
- [28] T. O. Raubenheimer & F. Zimmermann. *Rev. Mod. Phys.*, **72**, 1 (2000) 95.
- [29] A. Seryi. “Beam Delivery”. International Accelerator School for Linear Colliders, Sokendai, Japan (May 2006). <http://www.linearcollider.org/GDE/school/2006---Sokendai/Program-Calendar>
- [30] Y. Iwashita. *LCWS/ILC07 Conf. Proc.*, **1** (2007) 785–788.
- [31] I. A. Melzer-Pellmann. “Study of beam-beam effects with offset and angle scans”. EUROTEV-REPORT-2007-021 (2007).
- [32] P. N. Burrows & G. Myatt. “A Fast Feedback System for Luminosity Optimisation at a High-Energy Lepton Collider”. University of Oxford (February 2000).

- [33] J. Resta-Lopez. “Beam Dynamics Simulations for Linear Colliders: CLIC and ILC”. John Adams Institute PP seminar, University of Oxford (November 2007).
- [34] G. R. White. *PAC03 Conf. Proc.*, **4** (2003) 2778–2780.
- [35] Y. H. Chin. *APAC01 Conf. Proc.*, **1** (2001) 198–200.
- [36] S. Araki. “ATFII beamline layout”. Private communication (2008).
- [37] KEK ATF. Promotional Material. <http://www-atf.kek.jp/atf/files/ATF-E1227.pdf>
- [38] <http://www.atf.kek.jp/>. “Introduction to ATF Accelerator”.
- [39] J. Urakawa *et al.* “Accelerator Test Facility, Design and Study Report”. KEK Internal Report 95-4 (June 1995).
- [40] Y. Honda & K. Kubo *et al.* “Achievement of Ultra-Low Emittance Beam in the ATF Damping Ring”. SLAC-PUB-10113 (2003).
- [41] ATF2 Group. “ATF2 Proposal”. SLAC-R-771, KEK Report 2005-2 (August 2005).
- [42] T. Tauchi. *EPAC08 Conf. Proc.*, **1** (2008) 2907–2911.
- [43] P. N. Burrows *et al.* *PAC07 Conf. Proc.*, **1** (2007) 416–418.
- [44] P. Prieto. “High Resolution Upgrade of the ATF Damping Ring BPM System”. Beam Instrument Workshop Proceedings (2008). <http://www.als.lbl.gov/biw08/papers-final/TUPTPF040.pdf>
- [45] Y. Chung. *PAC1991 Conf. Proc.*, **3** (1991) 1121–1123.
- [46] S. Jolly. “An Intra-pulse Fast Feedback System for a Future Linear Collider”. Ph.D. thesis, University of Oxford (2003).
- [47] R. E. Shafer. “Beam Position Monitoring”. AIP (1990).
- [48] V. Sargsyan. “Comparison of Stripline and Cavity Beam Position Monitors”. TESLA Report 2004-03 (2004).
- [49] S. Molloy. “A Fast Feedback System Designed to Maintain Luminosity at a Linear Collider”. Ph.D. thesis, Queen Mary College, University of London (2006).
- [50] G. Vismara. *DIPAC99 Conf. Proc.*, **1** (1999) 12–18.
- [51] M. Wendt. *DIPAC01 Conf. Proc.*, **1** (2001) 63–65.
- [52] A. Kalinin. *AIP Conf. Proc.*, **648** (2003) 384–392.
- [53] K. H. Hu, J. Chen, C. H. Kuo, K. T. Hsu & T. S. Ueng. *PAC '99 Conf. Proc.*, **3** (1999) 2069–2071.

- [54] R. E. Shafer. “Log-ratio signal processing technique for beam position monitors”. Accelerator Instrumentation Workshop, Berkeley, CA, 27-30 Oct 1992.
- [55] P. N. Burrows. *LCWS04 Conf. Proc.*, **1** (2004) 369–371.
- [56] M. G. Minty & F. Zimmermann. “Measurement and Control of Charged Particle Beams”. Springer (2003).
- [57] K. Kubo & T. Okugi. “Dispersion Measurement in ATF DR”. ATF internal report (1997).
- [58] P. N. Burrows *et al.* *EPAC06 Conf. Proc.*, **1** (2006) 852–854.
- [59] P. N. Burrows. Private communication.
- [60] The NLC Collaboration N. Phinney (Ed.). “2001 report on the Next Linear Collider”. Prepared for APS / DPF / DPB Summer Study on the Future of Particle Physics, Snowmass, Colorado (2001).
- [61] Ronald D. Ruth. *EPAC1996 Conf. Proc.*, **1** (1996) 47–51.
- [62] P. N. Burrows. *PAC03 Conf. Proc.*, **1** (2003) 687–689.
- [63] C. I. Clarke. “The Interaction Point Collision Feedback System at the International Linear Collider and its Sensitivity to Electromagnetic Backgrounds”. D.Phil. Thesis, Wolfson College, University of Oxford (2008).
- [64] P. N. Burrows *et al.* *EPAC04 Conf. Proc.*, **1** (2004) 785–787.
- [65] P. N. Burrows. “Feedback on Nanosecond Timescales (FONT)(SLAC/NLCTA)”. Talk given at ELAN workshop, Frascati (2004).
- [66] P. N. Burrows. “Feedback on Nanosecond Timescales (FONT): FONT2 run results Dec 03/Jan 04”. LCUK presentation (2004).
- [67] P. N. Burrows *et al.* *PAC05 Conf. Proc.*, **1** (2005) 1359–1361.
- [68] P. N. Burrows *et al.* “Latest Beam Test Results of the FONT4 ILC Intra-train Feedback System Prototype”. LCWS/ILC08 Conf. Proc. (2008).
- [69] “Zeroth Order Design Report for the Next Linear Collider” (1996). <http://www-project.slac.stanford.edu/lc/ZDR/Zeroth.html>
- [70] B. Constance. “Status of FONT5 feedback system beam tests”. Talk at 8th ATF2 project meeting (2009).
- [71] G. Christian. “Feedback on Nanosecond Timescales (FONT) - Review of Feedback Prototype Tests at ATF(KEK)”. LC-ABD presentation (2007).
- [72] P. N. Burrows *et al.* *EPAC06 Conf. Proc.*, **1** (2006) 849–851.
- [73] C. Moler (creator). “MATLAB (Matrix Laboratory) ver:R2006b”. Mathworks (2006).

- [74] G. White. “FONT DAQ - A SEPUI Compliant Interface”. Private communication.
- [75] N. Terunuma. Private communication.
- [76] C. Perry. Private communication.
- [77] H. Dabiri-Khah. Private communication.
- [78] Bob L. Sturm. “MATLAB and the Moving Average”. University of California, Santa Barbara (2006).
- [79] KEK ATF. “ATF control system (v system)”. Database of Machine Parameters.
- [80] E. Wilson. “Lectures in Accelerator Physics”. John Adams Institute, University of Oxford (2006).
- [81] N. Delerue & D. Urner. “Accelerator Physics Option”. University of Oxford Lecture Series.
- [82] R. Apsimon. “Investigation into the Calibration and Resolution of the BPM Processors and the Analysis Software”. John Adams Institute, University of Oxford (June 2008).
- [83] C. Perry. “BPM processor electronics gain”. Private communication.
- [84] C. I. Clarke. “EM background tests of IP feedback hardware”. LC-ABD presentation (2007).
- [85] B. Constance. Internal FONT Note (July 2009).
- [86] SAS Institute. “Pearson Product-Moment Correlation” (2003). [http://support.sas.com/onlinedoc/913/getDoc/en/procstat.hlp/corr\\\_sect12.htm](http://support.sas.com/onlinedoc/913/getDoc/en/procstat.hlp/corr\_sect12.htm)
- [87] A. Kalinin. Private communication.
- [88] C. Perry. Private communication.
- [89] R. Lorenz. “Cavity Beam Position Monitors”. AIP Conference Proceeding 451 (1998).
- [90] T. Weiland *et al.* “CERN Accelerator School of RF Engineering; Review of Theory (I, II, III)”. Darmstadt Technical University (2000).
- [91] K. T. Tang. “Mathematical Methods for Engineers and Scientists 3”. Springer (2007).
- [92] L. Sevgi. *Turk. J. Elec. Engin*, **14** (2006) 293–311.
- [93] A. Liapin. “Resonant Cavities as Beam Position Monitors. Part 1. Waveguides and cavities”. University College London lectures. <http://www.hep.ucl.ac.uk/~liapine/>
- [94] Constantine A. Balanis. “Advanced Engineering Electromagnetics”. Wiley (1989).
- [95] A. Heo. “Masters Thesis” (2007). <https://www.pp.rhul.ac.uk/twiki/pub/JAI/AtfDigitalHardware/2007219009.pdf>

- [96] T. Nakamura. “Development of Beam-position Monitors with High Position Resolution”. Ph.D. thesis, University of Tokyo (2008).
- [97] O. Khainosvski. “NanoBPM Meeting Report: Analyzing Waveforms in position BPM in order to find an optimal Qexternal”. UC Berkeley (2005).
- [98] A. Liapin. “Resonant Cavities as Beam Position Monitors. Part 2. Features”. University College London lectures. <http://www.hep.ucl.ac.uk/~liapine/>
- [99] Microwaves101.com. “Superheterodyne receiver”. P-N Designs, Inc. [http://www.microwaves101.com/encyclopedia/receivers\\\_superhet.cfm](http://www.microwaves101.com/encyclopedia/receivers\_superhet.cfm)
- [100] Queens University Learning Wiki. “Mixers”. Queen’s University. <http://bmf.ece.queensu.ca/mediawiki/index.php/Mixers>
- [101] S. T. Boogert. “Beam position monitor handbook”. Royal Holloway, University of London. <https://www.pp.rhul.ac.uk/twiki/bin/view/JAI/BeamPositionHandbook>
- [102] S. T. Boogert. “ATF2 Cavity BPM”. ATF Status Report (2009). <https://www.pp.rhul.ac.uk/twiki/pub/JAI/AtfDigitalStatusReports/atf2-bpm-09092009.pdf>
- [103] M. Slater *et al.* “Cavity BPM System Tests for the ILC Energy Spectrometer”. Nuclear Instruments and Methods in Physics Research A (2008).
- [104] Adapted from Cavity BPM Assembly engineering diagram for Phang Accelerator Laboratory - not yet in
- [105] G. White. “Magnet Mover Overview”. SLAC Confluence Wiki. <http://silicondetector.org/display/ATF>
- [106] Stanford Linear Accelerator Center. “Magnet Mover Documentation for the ATF2 Program at KEK” (2008).
- [107] T. Smith *et al.* “ATF2 Q-BPM Front-end Electronics”. SLAC (2006).
- [108] SIS GmbH. “SIS3300/SIS330165/80/100 MHz VME FADCs: User Manual” (2004).
- [109] S. T. Boogert. “Cavity BPM caltone”. Private communication.
- [110] Argonne National Laboratory. “EPICS: Experimental Physics and Industrial Control System”. <http://www.aps.anl.gov/epics/>
- [111] S. T. Boogert. “Cavity BPM User Interface”. Private communication.
- [112] Y. Inoue Y. Honda. “RF measurement of ATF2 Q-BPMs”. ATF, KEK (2007).
- [113] G. White *et al.* *EPAC08 Conf. Proc.*, **1** (2008) 1562–1564.
- [114] S. T. Boogert. “ATF2 Cavity BPMs”. ATF Status Report (2009). <https://www.pp.rhul.ac.uk/twiki/pub/JAI/AtfDigitalStatusReports/atf2-bpm-16092009.pdf>
- [115] S. T. Boogert. “LCABD WP7: Cavity BPMs”. LCUK (2010).

- [116] S. T. Boogert *et al.* “Cavity Beam Position System for ATF2”. IPAC2010 (2010 - to be published).
- [117] J. Irwin *et al.* “Model-independent analysis with BPM correlation matrices”. EPAC98 (1998).
- [118] J. Safranek. “Model Independent Analysis”. USPAS (2006). [http://controls.als.lbl.gov/als\\_physics/csteier/uspas06/](http://controls.als.lbl.gov/als_physics/csteier/uspas06/)
- [119] A. Streun. “Momentum Compaction Factor”. CERN Accelerator School (1999). <http://sfsbd.psi.ch/pub/cas>
- [120] T. Okugi *et al.* “Lifetime Measurement of ATF Damping Ring”. EPAC98 (1998).
- [121] J. Resta-Lopez *et al.* “Luminosity Performance Studies of Linear Colliders with Intra-train Feedback Systems”. LCWS/ILC08. arXiv:0902.2915v1 [physics.acc-ph] (2008).
- [122] C. Swinson & B. Constance. “Font cable plant”. Private communication (2009).
- [123] A. Aryshev. “ATFII Timing Diagram”. Private communication (2009).
- [124] B. G. Korenev. “Bessel Functions and their Applications”. Chapman and Hall/CRC (2002).
- [125] Mathworks. “Matlab Documentation (filter)”. Mathworks. <http://www.mathworks.com/access/helpdesk/help/techdoc/ref/filter.html>
- [126] Julius O. Smith. “Introduction to Digital Filters with Audio Applications”. W3K Publishing (2007).
- [127] W. H. Steeb. “Mathematical tools in signal processing with C++ & Java simulations”. World Scientific Publishing co. (2005).